UC San Diego

UC San Diego Electronic Theses and Dissertations

Title

A search for new physics with Z bosons, jets, and missing transverse energy at CMS

Permalink

https://escholarship.org/uc/item/2496j89t

Author

Andrews, Warren T.

Publication Date

2012

Peer reviewed|Thesis/dissertation

UNIVERSITY OF CALIFORNIA, SAN DIEGO

A Search for New Physics with Z Bosons, Jets, and Missing Transverse Energy at CMS

A dissertation submitted in partial satisfaction of the
requirements for the degree
Doctor of Philosophy

in

Physics

by

Warren T. Andrews

Committee in charge:

>   Professor Frank Würthwein, Chair
>   Professor Claudio Campagnari
>   Professor John Hildebrand
>   Professor Ken Intriligator
>   Professor Avi Yagil

2012

The dissertation of Warren T. Andrews is approved, and it is
acceptable in quality and form for publication on microfilm
and electronically:

_____

_____

_____

_____
                                                        Chair

University of California, San Diego

2012

To my family.

I have a limited intelligence and I've used it in a particular direction.

—Richard P. Feynman

TABLE OF CONTENTS

LIST OF FIGURES

LIST OF TABLES

ACKNOWLEDGEMENTS

| 2005 | B. A. in Physics, New York University |
| 2012 | Ph. D. in Physics, University of California, San Diego |

PUBLICATIONS

"Search for physics beyond the standard model in events with a Z boson, jets, and missing transverse energy in pp collisions at $\sqrt{s} = 7$ TeV", Physics Letters B, 2012

"Search for electroweak production of charginos and neutralinos using leptonic final states in pp collisions at $\sqrt{s} = 7$ TeV", submitted for publication

ABSTRACT OF THE DISSERTATION

A Search for New Physics with Z Bosons, Jets, and Missing Transverse Energy at CMS

by

Warren T. Andrews

Doctor of Philosophy in Physics

University of California, San Diego, 2012

Professor Frank Würthwein, Chair

I present a search for new physics in the final state of a Z boson, jets, and missing transverse energy in proton-proton collisions delivered by the Large Hadron Collider (LHC) at CERN in 2011 at a center of mass energy of 7 TeV and collected by the Compact Muon Solenoid (CMS) experiment.

Chapter 1

Introduction

Particle physics is the study of the most fundamental constituents of matter and their interactions. All of physics concerns itself with matter and energy, but particle physics seeks to understand the fundamental particles which constitute matter and to completely specify the ways those particles interact with each other. One way this is currently done is using particle accelerators. Today, the world's highest energy particle accelerator is called the Large Hadron Collider (LHC), and it is located at CERN, outside Geneva, Switzerland.

This thesis describes an analysis of proton-proton collisions–provided by the LHC and collected by the Compact Muon Solenoid (CMS) detector–which finds particles called Z bosons and looks at a particular kinematic spectrum called Missing Transverse Energy (*MET*). The remainder of the introduction will attempt to describe what this means to a non-physicist audience without technical details.

Particle physics is also called *high-energy physics* because in order to produce very massive particles, we must collide highly energetic particles. The kinetic energy of the accelerated particles (protons, in the case of the LHC) is converted into mass of new particles. This is possible because of Einstein's famous equation $E = mc^2$, which is a consequence of special relativity.

By modern standards, the field of particle physics is quite old: nearly 100 years. Though I do not have time to describe it, for an account of the history of particle physics, see [1]. For introductory textbooks on particle physics (at the advanced undergraduate level), see [2, 3].

1.1 Overview of Particle Physics

The best theory of particle physics is called *the standard model*. The main aspects of the theory were developed over roughly thirty years from the 1950s through the 1970s, though research on the standard model continues today. It is a quantum field theory, which means it is a quantum mechanical theory which is fully compatible with special relativity. I say 'best' because the standard model has withstood confrontation with thousands of experimental results and emerged mostly unscathed. It is particularly impressive, and perhaps even somewhat unexpected, that this is true even after the LHC's first year of high energy (7 TeV center of mass energy) running with large luminosity: the integrated luminosity of the 2011 dataset is about 5 inverse femtobarns at each CMS and ATLAS.

I will now take a moment to explain the last statement.

The eV is the most common unit of energy used in particle physics, and it is the amount of kinetic energy an electron has after being accelerated for one meter across a potential of one volt. It is a very tiny amount of energy. The visible light produced by a lightbulb has an energy of around one electron-volt (eV) per photon. Normally the 'eV' has a prefix denoting it's order of magnitude. Just like we use 'cm' for centimeter (10^{-2} m), and km (10^3 m) for kilometer, we speak of MeV (10^6 eV), GeV (10^9 eV), TeV (10^{12} eV), etc. The center of mass energy of the LHC is simply twice the energy of each proton in each beam: 3.5 TeV in 2011.

A 'barn' is a unit of area, and the units of cross-section are units of area. A barn is equal to 10^{-28} m^2 (100 fm^2). Luminosity is basically the rate at which collisions occur in accelerators, so that the number of collisions collected for a given process is the integrated luminosity multiplied by the cross-section for that process.

There are four fundamental forces of nature. The standard model describes three of them: the strong force, the weak force, and electromagnetism. The fourth force is gravity, which is described by general relativity, but has not yet been described using the same theoretical framework as the other three forces. Each force has particles associated with it which mediate the force. For example, when two electrons repel each other (because they have the same electric charge), they do so by exchanging a photon, the quanta of light, as shown in Fig. 1.1.
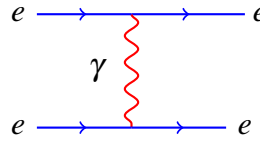
Figure 1.1: Feynman diagram for two electrons (e) scattering via exchange of a photon (γ). I use the convention that time increases to the right (ie., a horizontal axis which is not shown).

This figure is called a *Feynman Diagram*, named for its inventor, Richard P. Feynman (for a biography, see [4]). Feynman diagrams are very useful both as a visual way to understand particle interactions and as a theoretical tool for computation.

Although electromagnetism has only a single carrier, the weak force has two. These are called the W and the Z. The W has electric charge, but the Z is electrically neutral. The carrier of the strong force is called the gluon. Although the photon and gluon are massless, the W and Z are both massive, and, as it turns out, very heavy. They will therefore decay to lighter particles. Both the W and Z couple to all the fermions (matter particles) of the standard model, and they therefore couple to electrons and muons. Electrons and muons both belong to a class of particles called leptons. The other leptons are the tau and the neutrinos. The particle content of the standard model is summarized in Fig. 1.2.

The W and Z decay extremely rapidly (order 10^{-24} s), and hence cannot be detected. However, CMS is designed to detect both electrons and muons. The analyses described in this thesis rely on detecting the Z via its decay to pairs of electrons or muons. Because the Z is electrically neutral, it must decay into particle-anti-particle pairs. This means that the decay products are the same *flavor* (ie, lepton type) and opposite charge. The diagrams for the Z decaying into electron-positron pairs and muon-anti-muon pairs are shown in Fig. 1.3.

There is one more process which is very important to understanding the analysis described in this thesis, and that is the production of top quarks (t) and anti-top quarks ($\bar{t}$), which we call simply $t\bar{t}$. All quarks have *color charge*, which means they interact via the strong force. As I mentioned, the strong force is mediated by gluons. Gluons

Figure 1.2: The particle content of the standard model. The matter particles are all spin 1/2, and are hence fermions. These are shown in purple (leptons) and green (quarks). The gauge bosons (shown in red) are all spin 1 and are responsible for mediating the forces in the standard model.
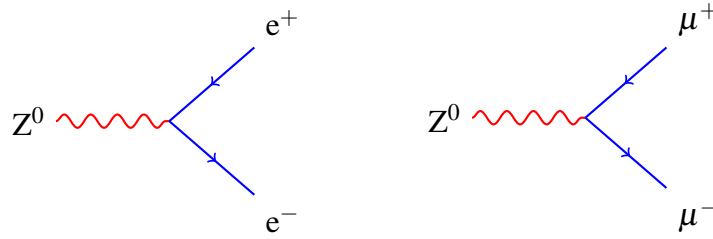
Figure 1.3: Feynman diagrams for the Z boson decaying into an electron-positron pair (left) and a muon-anti-muon pair (right).

are therefore the particles which hold together the quarks (two up quarks and one down quark) which make up protons. Gluons also couple to each other (in technical terms, this is called a "non-abelian" force, or gauge group). Because top quarks are so heavy, they immediately decay to a W boson and a b quark. The W itself then decays to either leptons (one charged lepton and one neutrino of the same flavor), or quarks. A $t\bar{t}$ production and decay diagram is shown in Fig. 1.4.

1.2   Particle Physics Theory Beyond the Standard Model

Despite its great success, we know that the standard model is not complete for several reasons, both experimental and theoretical. The two major pieces of experimental evidence which point towards physics beyond the standard model are neutrino masses and dark matter [5, 6]. Neither of these invalidates the existing predictive power of the standard model, and therefore the standard model remains the most successful theory of particle physics. However, both neutrino masses and dark matter are firmly established experimentally and cannot be explained by the standard model. It is for this reason, among others, that many theories *beyond* the standard model have been developed. I will discuss only one of them, called supersymmetry (abbreviated SUSY).

Supersymmetry is a symmetry between fermions and bosons. This means that for every fermion in the standard model, supersymmetry posits that there is a boson partner of that fermion, and analogously for bosons. The supersymmetric partners of the fermions have the same names as their standard model partners but with an 's' added
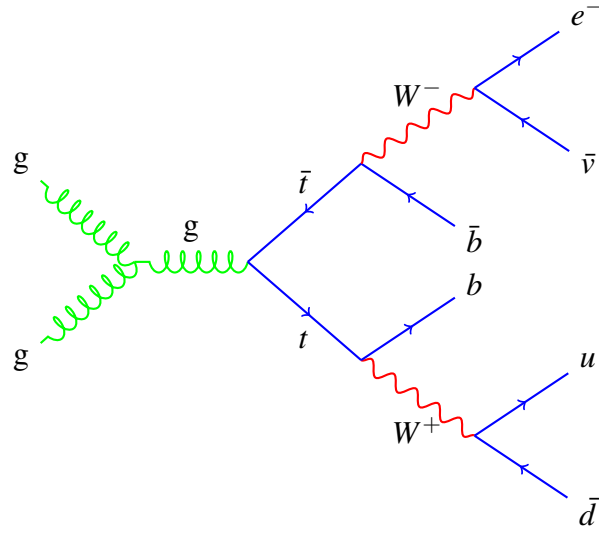
Figure 1.4: Feynman diagram for $t\bar{t}$ production and decay. The left-most vertex is a triple-gluon coupling: the two gluons on the left originate in the protons the LHC collides. The next vertex is gluon-top-anti-top, which is in direct analogy to a photon or Z coupling to an electron-positron pair. The top quarks then decay as described in the text.

at the beginning. For example, partners of the standard model quarks are called squarks. Supersymmetric partners of standard model bosons get an 'ino' added at the end of their name: the electroweak gauge boson partners are called electroweakinos.

There is currently no experimental evidence for SUSY (see Sec. 1.4). It must therefore not be an exact symmetry, but an approximate one. If it were an exact symmetry, the supersymmetric particles would have the same masses as their standard model partners. In particle physics jargon, approximate symmetries are called 'broken' symmetries. There is a mechanism, i.e., some part of the Lagrangian, which breaks a symmetry. In the case of electroweak symmetry breaking, it is the higgs which breaks the symmetry and in so doing, gives mass to the W and Z bosons, while leaving the photon massless. For SUSY, there are a variety of options. The most popular SUSY breaking options are two are gravity-mediated and gauge-mediated. See Sec. 2.2.

1.3 Missing Transverse Energy (MET)

This Section describes an experimental quantity called missing transverse energy, which we abbreviate as MET. The LHC collides protons, but as I mentioned in Sec. 1.1, protons are not fundamental particles: they are composed of quarks (which give them their electric charge) and gluons (which hold the quarks together). It turns out that because the strong force is so strong, the energy associated with the binding of the quarks actually accounts for about 99% of the mass of the proton. The remaining one percent is the rest mass of the quarks in the proton (two up quarks and one down quark).

Becuase the LHC center-of-mass energy (7 TeV) is nearly 10,000 times the mass of the proton (1 GeV), the protons which collide in the LHC disentegrate, and what actually collides are the constituents of the proton: either the quarks or the gluons. This is why the initial state of the collision and decay diagram of Fig. 1.4 is two gluons: one originates in each proton.

Although the energy of the proton is known, the fraction of this energy carried by the quarks or gluons which collide is not known, and is impossible to know. It is normally the case that the fractional energies of the two particles (quarks or gluons) in the collision are different. This means that there is net energy along the proton beam

line which is not known. We therefore cannot conserve momentum along the beam line.

However, momentum *transverse* to the (proton-proton) beam is conserved. This is the premise behind *MET*. If we can measure the transverse momenta of all particles produced in a single collision, they must all add to zero. In reality, we cannot do this because our detector (described in Chapter 3) is not perfect, so the transverse momenta do not always sum to zero. Also, we cannot detect all particles. Neutrinos (ν) are so light and interact so weakly (only via the weak force) that we cannot detect them. Therefore a neutrino produced in a collision (for example, from the decay of a W or Z boson) will lead to transverse momentum imbalance. This is why in $t\bar{t}$ decay to two leptons, there can be large *MET*. For more details on how *MET* is computed for the analyses described herein, see Sec. 4.1.1.

1.4   SUSY Searches

Because SUSY has been a popular theoretical framework for many decades already, it is natural that there has been significant experimental effort invested in searching for SUSY signatures. These signatures cover practically all final states possible including jets and *MET*[7, 8, 9], single isolated leptons [10], opposite-sign [11] and same sign leptons [12], and photons [13, 14] (these references are all examples from CMS). Similiar searches have also been performed by the ATLAS collaboration, the other general purpose detector at the LHC [15, 16]. For a SUSY search at Fermilab's Tevatron in the same final state as this thesis (Z + jets), see [17]. Another example of a Tevatron SUSY search which utilizes a GMSB model (see Sec. 2.3) is [18]. The work of this thesis (Chapter 4) is published in [19]. The work of Chapter 5 has been submitted for publication [20].

Chapter 2

Theory

What follows is not meant to be a technical or mathematical treatment of particle physics theory. It is meant to be a very broad overview which focuses on the aspects of theory which are most relevant to the experimental work described in this thesis. I will briefly summarize the main features of the standard model, and then do the same for SUSY. For the latter, I will describe some models, again, from an experimental perspective, which are relevant to other parts of this thesis.

2.1 The Standard Model

The standard model describes three of the four fundamental forces of nature: the strong force, the weak force, and the electromagnetic force. The latter are unified in the context of the standard model and referred to collectively as the electroweak force. Gravity is the fourth force and is not described by the standard model.

The particle content of the standard model is summarized in Fig. 1.2. The fermions are arranged in three generations. The first generation of quarks are the up and down quarks; the first generation of leptons are the electron and the electron neutrino, and so on. The bosons are the force carriers, or mediators. The particle which mediates the electromagnetic force is the photon, the mediators of the weak force are the W and Z bosons, and the mediator of the strong force is the gluon.

Each force in the standard model is associated with a gauge symmetry, which is a continuous group of local transformations. The quantized fields associated with

the gauge symmetry are called gauge bosons. These must be vector fields, hence all standard model gauge bosons are spin one[21]. The higgs is responsible for giving mass to the gauge bosons and the fermions via its coupling to them. In the standard model, there is a doublet of scalar higgs fields, and because they are complex fields, there are four of them in total. Three are 'eaten' by the W and Z, and hence there is only one physical higgs field which is the higgs boson[22].

2.1.1 Electroweak Interactions in the Standard Model

The standard model electroweak gauge bosons, the $W^\pm$ and Z^0, couple to all the fermions of the standard model, as shown in Fig. 2.1. The W-fermion-fermion vertex factor is [22]

$$-i\frac{g}{\sqrt{2}}\gamma^\mu\frac{1}{2}(1-\gamma^5) \tag{2.1}$$

and the Z-fermion-fermion vertex factor is

$$-i\frac{g}{\cos\theta_W}\gamma^\mu\frac{1}{2}(c_V-c_A\gamma^5) \tag{2.2}$$

where g is the weak coupling factor, and γ are the gamma matricies. θ_W is the Weinberg angle and has the value $\cos\theta_W = \frac{m_W}{m_Z} \cong 0.881$, and $\sin^2\theta_W \cong 0.231$. The constants c_V and c_A are the vector and axial-vector couplings respectively, and are different for different fermion types as described below.

In the above equations, the factor $(1-\gamma^5)$ is the term responsible for the so-called *V-A*, for vector-axial-vector, coupling of the weak force. This factor projects out left handed fermion chirality, and this is why only left handed chirality fermions interact with the electroweak gauge bosons. The W coupling is pure V-A, while the Z has c_V and c_A factors which make different fermions have different components of vector and axial-vector couplings. The values of c_V and c_A for different fermions are given in Tab. 2.1.

The W coupling (Eq. 2.1) is proportional to $g/2\sqrt{2}$. For Z (Eq. 2.2), this is $cg/2\cos\theta_W$, where c is the average of c_V and c_A, or about 0.34 for up-type quarks and 0.42 for down-type quarks. This makes the ratio of Z to W couplings roughly 70% for down-type quarks and 54% for up-type quarks.
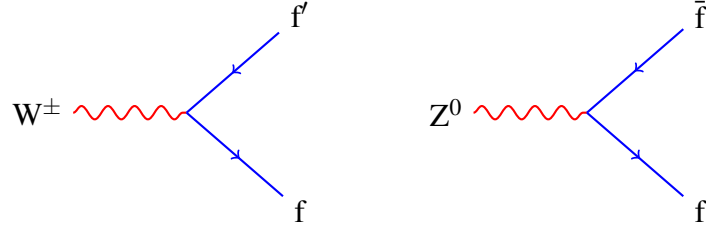
Figure 2.1: Standard model electroweak vertices for the W boson (left) and Z boson (right) coupling to fermions.

Table 2.1: Values of the constants c_V and c_A of Eq. 2.2 for different fermion types.

fermion	c_A	c_V
neutrinos	1/2	1/2
charged leptons	-1/2	$-1/2 + 2\sin^2\theta_W \cong -0.03$
up-type quarks	1/2	$1/2 + \frac{4}{3}\sin^2\theta_W \cong 0.19$
down-type quarks	-1/2	$-1/2 + \frac{2}{3}\sin^2\theta_W \cong -0.34$

2.2 Supersymmetry

One of the first problems which arose in supersymmetry is the decay of the proton. Experimentally, the proton is known to be stable with a half life of some 10^{33} years [23]. (Compare this to the age of the universe, which is about 14 billion years, or 1.4 10^{10} years [24].) However, the most general models of supersymmetry allow operators which can cause proton decay, as shown in Fig. 2.2. In order to avoid this problem, the concept of R-parity is introduced.

R-parity is defined as: $(-1)^{3(B-L)+2s}$, where B is baryon number, L is lepton number, and s is spin [25]. All standard model particles have R = +1, while all super-symmetric particles have R = -1. Because R-parity is a multiplicative quantum number, there must be an even number of SUSY particles in the final state (the inital state being all standard model particles) if R-parity is conserved. This means that the s-channel proton decay described in Fig. 2.2 is forbidden. Also if R-parity is conserved, the lightest SUSY particle (LSP) must be absolutely stable. LSPs are therefore a natural dark matter candidate [6]. It is for these two reasons, among others, that R-parity violating SUSY is
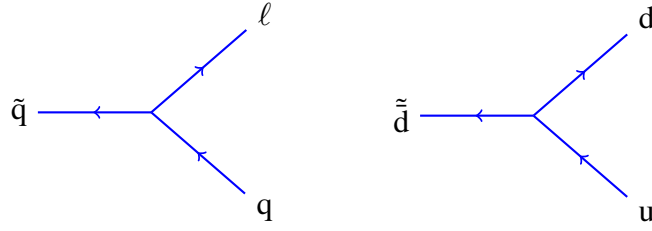
Figure 2.2: Vertices in SUSY which are responsible for proton decay. Both vertices are R-parity violating. The left vertex violates lepton number and the right violates baryon number. The two squark lines can be connected to form (part of) the diagram for proton decay into a meson and a lepton.

a popular theoretical framework.

2.2.1 Gauge Sector of SUSY

In the two higgs doublet model of SUSY, the single higgs double of the standard model is repeated. There are therefore five physical higgs fields, three of them electromagnetically neutral, and two charged. Adding these to the four standard model electroweak gauge bosons gives a total of nine standard model bosons which have fermionic partners in SUSY. These are called gauginos, and there are two general types of gauginos: neutralinos and charginos[26, 27].

The neutralinos are admixtures of the following SUSY fields: the bino, the neutral wino, and the higgsinos. The bino and wino are the partners of the electroweak gauge bosons, and the higgsinos are the partners of the higgs fields. There are therefore four neutralinos, and their mass-gauge eigenstate mixing matrix is therefore a four-by-four matrix which is called N below.

The charginos are admixtures of the charged wino and the charged higgsino fields. There are only two of them, so their mixing matrix is two-by-two. However, because they are complex fields, there are two two-by-two mixing matrices. These will be referred to below as U and V.

For each mixing matrix, the first index is the mass eigenstate and the second is the gauge eigenstate (also referred to as the interaction eigenstate). N_{i1} couples to the
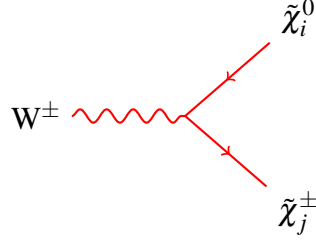
Figure 2.3: Diagram for the W-chargino-neutralino vertex given in Eq. 2.3.

bino, N_{i2} couples to the neutral wino, $N_{i3,4}$ couple to higgsino, and $U_{i1,2}$ and $V_{i1,2}$ couple to the charged wino and higgsino respectively. From this, one can determine the relative couplings for different mixing angles as is demonstrated in the following sections.

2.2.2 W-Chargino-Neutralino Coupling

The vertex coupling the W to the chargino and neutralino is given in Eq. 2.3 [26] and shown in Fig. 2.3. (g and γ are introduced in Sec. 2.1.1, and N, U, and V are the matricies introduced in Sec. 2.2.1.)

$$\frac{ig}{2}\gamma^{\mu}\left[\left(-\frac{1}{\sqrt{2}}N_{i4}V_{j2}^{*}+N_{i2}V_{j1}^{*}\right)(1-\gamma^{5})+\left(\frac{1}{\sqrt{2}}N_{i3}^{*}U_{j2}+N_{i2}^{*}U_{j1}\right)(1+\gamma^{5})\right] \qquad (2.3)$$

From the form of this vertex, one can determine the relative couplings for different mixing scenarios. For example, pure higgsino coupling means that $N_{i3,4}$ are maximal and $N_{i1,2}$ are zero. This results in the coupling (Eq. 2.4):

$$\frac{ig}{2}\gamma^{\mu}\left[-\frac{1}{\sqrt{2}}N_{i4}V_{j2}^{*}(1-\gamma^{5})+\frac{1}{\sqrt{2}}N_{i3}^{*}U_{j2}(1+\gamma^{5})\right] \qquad (2.4)$$

If we further assume that $N_{i4}=N_{i3}^{*}$ and $V_{j2}^{*}=U_{j2}=1$ for simplicity, we get Eq. 2.5:

$$\frac{ig}{\sqrt{2}}\gamma^{\mu}N_{i4}\gamma^{5} \qquad (2.5)$$

The opposite case is pure wino coupling. This corresponds to $N_{i2}=1$ and all other $N_i=0$. Eq. 2.3 then becomes:

$$\frac{ig}{2}\gamma^{\mu}\left[N_{i2}V_{j1}^{*}(1-\gamma^{5})+N_{i2}^{*}U_{j1}(1+\gamma^{5})\right] \qquad (2.6)$$

If we again assume $V_{j1}^* = U_{j1} = 1$, we are left with

$$ig\gamma^\mu N_{i2} \tag{2.7}$$

Comparing Eq.2.5 to Eq.2.7, we find that the ratio of wino-like couplings to higgsino-like couplings is $1/\sqrt{2}$ (assuming that $N_{i2} = N_{i4}$), which translates to a cross-section ratio of 1/2.

2.2.3   Z-Neutralino and Z-Chargino Couplings

The coupling of the Z to two neutralinos or charginos is similiar in structure to the W-chargino-neutralino coupling discussed in Sec. 2.2.2 [26]. These vertices are shown in Fig. 2.4 and their form is given in Eq. 2.8 (Z-chargino) and Eq. 2.9 (Z-neutralino). (θ_W is the Weinberg angle, introduced in Sec. 2.1.1.)

$$\frac{ig}{2\cos\theta_W}\gamma^\mu\Big[[-V_{i1}V_{j1}^* - \frac{1}{2}V_{i2}V_{j2}^* + \delta_{ij}\sin^2\theta_W](1-\gamma^5)+ \tag{2.8}$$
$$[-U_{i1}^*U_{j1} - \frac{1}{2}U_{i2}^*U_{j2} + \delta_{ij}\sin^2\theta_W](1+\gamma^5)\Big]$$

$$\frac{ig}{2\cos\theta_W}\gamma^\mu\frac{1}{2}\Big[[-N_{i3}N_{j3}^* + N_{i4}N_{j4}^*](1-\gamma^5)+ \tag{2.9}$$
$$[N_{i3}^*N_{j3} - N_{i4}^*N_{j4}](1+\gamma^5)\Big]$$

To illustrate the Z-chargino coupling (Eq. 2.8), I will assume U and V are both the identity matrix, and $i = j$. Physically, this corresponds to no mixing between the charginos. The coupling is then:

$$\frac{ig}{2\cos\theta_W}\gamma^\mu[-\frac{3}{2} + \sin^2\theta_W] \tag{2.10}$$

The Z-neutralino coupling (Eq. 2.9) has no terms for wino or bino coupling (ie, $N_{i1,2}$ do not appear). This is in analogy to the fact that in the standard model, there are no ZZZ, ZZγ, nor Z$\gamma\gamma$ vertices. The coupling is maximized when the neutralinos are all one higgsino type, that is when $N_{i,j3}$ are maximized and $N_{i,j4} = 0$ or vice versa. The coupling would then become (assuming $N_{i3} = N_{i4}$):
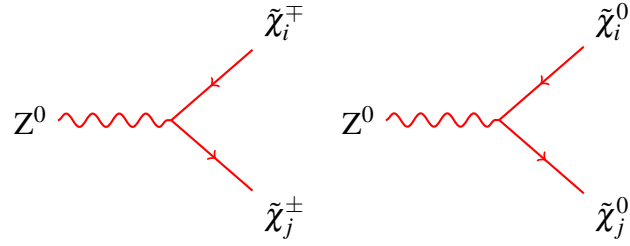
Figure 2.4: Diagram for the Z-chargino (left) and Z-neutralino (right) vertices given in Eq. 2.8 and Eq. 2.9.

$$\frac{ig}{2\cos\theta_W}\gamma^\mu N_{i4}\gamma^5 \tag{2.11}$$

This can be compared to the simplified wino-like coupling of Eq.2.7, and the only difference is a factor of $1/2\cos\theta_W \approx 0.568$.

2.2.4 Electroweakino Production

The summaries of the vertices in Sec. 2.2.2 and 2.2.3 show that the Z-neutralino coupling (Eq.2.7) is roughly 57% of the wino-like W-chargino-neutralino coupling. This is very similiar to the case in the standard model, as we saw in Sec. 2.1.1, where the Z coupling to quarks is rougly 50-70% lower than the W coupling to quarks.

In SUSY, neutralino pair production is normally suppressed relative to chargino-neutralino production. One of the reasons is the ratio of couplings summarized above. To explain the other reason, it is useful to consider the analogous standard model processes: WZ, and ZZ production.

In the standard model, the ZZ cross section at the LHC is roughly half of the WZ cross section. Again, this is partly due to ratio of W to Z couplings to quarks. In addition, the s-channel production diagram for ZZ does not exist because there is no particle which can be the propagator (see Fig. 4.2). This is because in the standard model, there are no ZZZ, ZZγ, nor Z$\gamma\gamma$ vertices.

In SUSY, there are both s- and t-channel production diagrams for all combinations of final state charginos and neutralinos because of the squark-quark-electroweakino vertex. However, for models where the squarks are very heavy, production diagrams

which have squark propagators (t-channel diagrams) will be suppressed. This means that the only diagrams which lead to chargino-neutralino production are s-channel diagrams with a W as the propagator. These arguments will be relevant for choosing the models for the interpretation of the electroweakino anlaysis of Chapter 5 (see Sec. 5.6).

2.3   GMSB Model

GMSB is an abbreviation for "Gauge-mediated supersymmetry breaking," which means that supersymmetry is broken by some part of the the gauge sector. In GMSB models, the gravitino ($\tilde{G}$) is the LSP, and is normally very light, $\sim$1 keV.

The general features of SUSY as described in Sec. 2.2 all apply here. The difference between different models all boil down to parameter choices. The main parameters which are relevant are the particle masses and the couplings.

In this section, I will focus on a experimentalist-minded overview of one particular GMSB model described in [28]. The class of models described in this reference cover a very wide range of phenomenology which I will not attempt to summarize. Instead, I will focus on the particular model used in the interpretation of the analysis described in Chapter 5 (see Sec. 5.5).

In this model, the squark and gluino masses are set to several TeV so that they cannot be produced at a center of mass energy of 7 TeV (which is the energy of the LHC data used in this thesis). The sleptons are also heavy. In contrast, the electroweakinos are all very light (a few hundred GeV). There is one parameter which we will vary in the interpretation for this model; this parameter is called m_χ and is the mass of the heavy neutralino ($\tilde{\chi}_2^0$).

The mass hierarchy of this model is such that the light neutralino ($\tilde{\chi}_1^0$) is just barely (a few GeV) lighter than m_χ. Both the $\tilde{\chi}^\pm$ and the $\tilde{\chi}_2^0$ have no other decay mode than to decay via the $\tilde{\chi}_1^0$. In both cases, there is a very offshell boson (W or Z) in the decay. Because this boson is so light (only a few GeV), its decay products are not detectable. Because of these $\tilde{\chi}^\pm$ and $\tilde{\chi}_2^0$ decays, every event in this model will contain two $\tilde{\chi}_1^0$.

The $\tilde{\chi}_1^0$ is the next-to-lightest SUSY particle (NLSP); as such, it must decay to
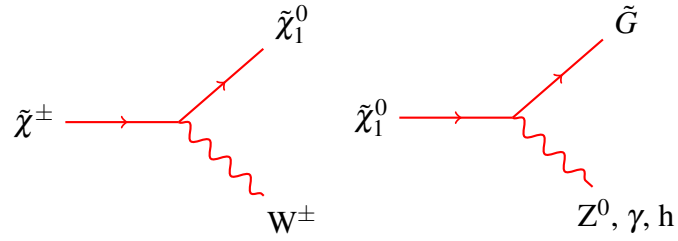
Figure 2.5: Diagram for the chargino decay (left) and neutralino decay (right) in the GMSB model of Sec. 2.3. Connecting the two neutralino lines creates the chargino cascade decay diagram. Note that the left diagram is simply the vertex of Fig. 2.3.

the LSP and a standard model particle. The decay, shown in Fig. 2.5, is to a gravitino ($\tilde{G}$, the LSP) and either a Z, photon (γ), or higgs (h). The branching ratios change as a function of m_χ, but the branching ratio to Z always dominates. This is because the $\tilde{\chi}_1^0$ has very little higgsino and photino content by design, in order to maximize the branching ratio to Zs. In fact, for $m_\chi = 200$ GeV, the branching ratio to Z is 100%. (See Sec. 5.5 for other branching ratios.) The final state for this model is therefore often ZZ + *MET*, where the *MET* comes from the LSPs. As we will see, this is exactly the final state that the analysis described in Chapter 5 is designed to search for.

Chapter 3

The CMS Detector

This chapter summarizes the main features of the CMS detector, providing an overview of how different types of particles interact with the detector elements rather than a complete technical specification. The CMS detector contains a large solenoid which is responsible for generating a magnetic field of 3.8 Tesla. This high magnetic field is necessary to measure the momentum of high energy muons and other charged particles. The other main features of the CMS detector are the silicon tracker (Sec. 3.1), electromagnetic calorimeter (ECAL) (Sec. 3.2), hadronic calorimeter (HCAL) (Sec. 3.3), and muon detectors (Sec. 3.4). The general layout of the CMS detector is shown in Fig. 3.1. A more detailed description of the CMS detector can be found in [29, 30].

3.1   Silicon Tracker

A charged particle passing through silicon will create electron-hole pairs in the material, which, with a voltage bias applied, can be captured on capacitors and then digitized and recorded. This works only for charged particles because the charged particles' electric fields interact with the material. This is the basic way that silicon detectors can detect charged particles. The sensitive areas of silicon are arranged in concentric cylinders around the beam in the barrel portion of the detector, and in a disc shape in the endcaps. Charged particles are therefore detected in several layers of silicon sequentially. The portion of the tracker closest to the beampipe are the pixel detectors (Fig. 3.2). An overview of the tracker is shown in Fig. 3.3.

18
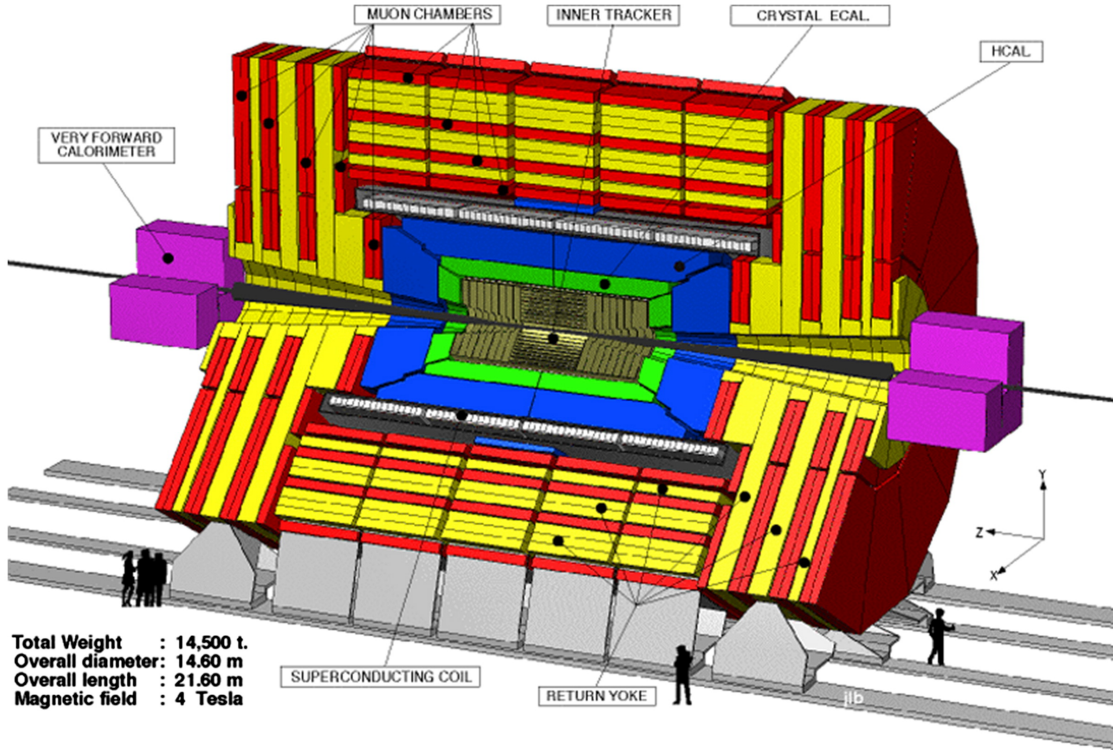
Figure 3.1: Overview of CMS detector.

Each crossing of a charged particle with a silicon tracker layer is called a 'hit.' Because of the magnetic field, the charged particles move in a helix. This helix is reconstructed by connecting the hits in as many layers as possible. The radius r of the helix is proportional to the momentum of the particle:

$$r = \frac{p}{q\,B} \tag{3.1}$$

where p is momentum, q is electric charge, and B is the magnetic field. Since q and B are known constants (the sign of q will determine if the particle bends clockwise or counter-clockwise), measuring r by fitting the trajectory to a helix allows the momentum of the particle to be extracted. This is how the tracker measures momentum.

From Eq. 3.1, one can see that if the momentum is too large, the radius of the trajectory will be much larger than the radius of the tracker, so the trajectory will appear to be straight or nearly so. This effect is the largest limitation to momentum resolution at high momentum, and also why the magnetic field (B) must be so large.

For low momentum, the greatest limitation to momentum resolution is from multiple scattering. Multiple scattering refers to a change in direction due to interactions with material. This is a random process both for the direction of the scatter and the amplitude of the scatter. For small angles, the distribution of scattering angle is gaussian, though there are long non-gaussian tails from Rutherford scattering. The small angle scatters are proportional to $1/v^2$ (v is velocity), so for appreciable velocity, the effect of multiple scattering on momentum resolution is negligible compared to the one described previously. This occurs at around 5 GeV. Also, the scattering angle is proportional to $\sqrt{x/X_0}$, where x/X_0 is the thickness of the material in units of radiation lengths (see Sec. 3.1.1). Therefore, less material leads to less scattering.

There is also a contribution to the momentum resolution from the intrinsic hit resolution, but as we'll see in Sec. 3.1.2, this is quite good, so it is a very small effect which is independent of momentum.

Combining the above effects, we arrive at the following equations which describe tracking resolution [31]:

$$\frac{\sigma(p_T)}{p_T} = \frac{\sigma_{r\phi} p_T}{0.3BL^2} \sqrt{\frac{720}{N+4}} \tag{3.2}$$

$$\frac{\sigma(p_T)}{p_T} = \frac{0.05}{BL} \sqrt{\frac{1.43L}{X_0}} \tag{3.3}$$

Where p_T is the track transverse momentum, $\sigma(p_T)$ is its uncertainty ($\sigma(p_T)/p_T$ is the relative uncertainty), $\sigma_{r\phi}$ is the hit resolution in $r - \phi$, L is the tracker radius, and N is the number of hits in the track (and other symbols are as above). B and L are therefore fixed for a detector, while $\sigma_{r\phi}$ and N will depend, for example, on the η of a track. Eq. 3.2 describes the transverse momentum resolution due to detector effects including number of hits and hit resolution, while Eq. 3.3 describes the contribution due to multiple scattering. Comparing the two, we see that for low p_T, the effects of multiple scattering dominate the resolution since these have no momentum dependence. For larger p_T, device resolution dominates due to the siffness of the track as discussed above.
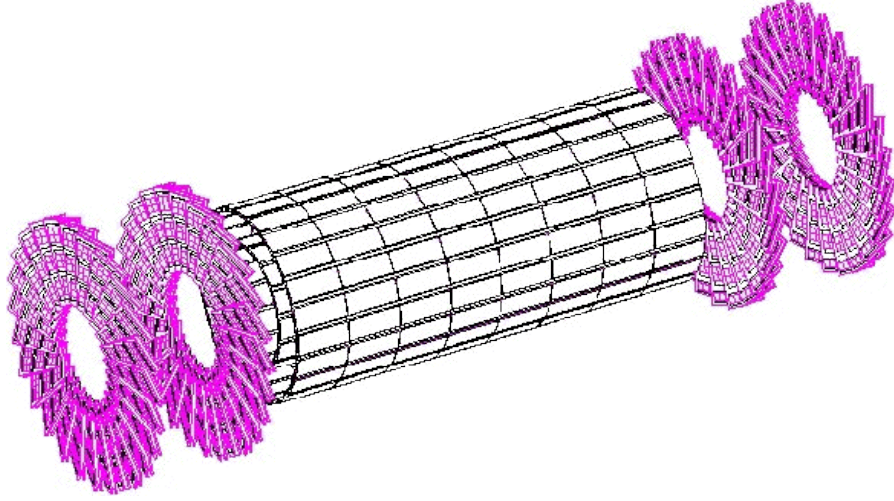
Figure 3.2: The CMS pixel system. The barrel pixels are shown in black, and the endcap pixels in pink.

3.1.1   Interactions in the Tracker

The above discussion applies to electrically charged particles only. Neutral particles do not interact with the tracker's silicon the way that charged particles do, instead they pass through undetected. However, neutral particles may interact via other means which I will now describe.

Photons may convert to an electron-positron ($e^- e^+$) pair by interacting with an atomic nucleus of the detector material. Such electron-positron pairs are called "conversions" and are a background to prompt electrons (see Sec. 4.1.2). The characteristic amount of material traversed before this occurs is described by the "radiation length," usually denoted X_0, which has units of mass per area. The radiation length is material dependent, and it is 7/9 of the mean free path for pair production for a high energy photon. Radiation length is related to energy loss per distance traveled (dE/dx, where x is measured in units of X_0, as in Sec. 3.1) by [32]:

$$\frac{dE}{dx} = -\frac{E}{X_0} \tag{3.4}$$

Radiation length also describes how electrons lose energy via bremsstrahlung, which is the electromagnetic radiation produced by photons interacting with atomic
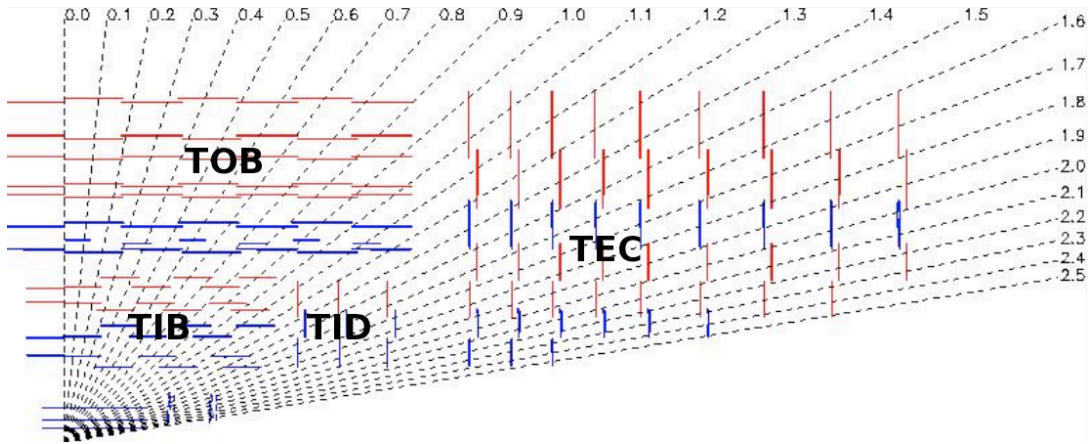
Figure 3.3: Overview of the CMS tracker (one quarter $r-z$ view). The pixels are shown in the bottom left (unlabeled). The next tracker sub-system moving outwards from the beam (which would be horizontal at the bottom of the image), is the tracker inner barrel (TIB) and tracker inner disk (TID). Finally come the tracker outer barrel (TOB) and tracker endcap (TEC). The numbers are η coordinates.

nuclei. For each radiation length traversed, an electron will lose all but $1/e \approx 37\%$ of its energy. The CMS tracker material budged in radiation lengths is shown in the left panel of 3.4.

Long lived neutral hadrons such as the neutron (n) and neutral kaons (K^0) also may interact with atomic neuclei in the tracker volume, although such interactions are rare. Similiar to radiation length, the "interaction length" describes the probability of nuclear interactions in a material: after traversing one interaction length, the probability of survival without interacting is $1/e$. The interaction length is also material dependent, and always longer than the radiation length for a given material, for the following reason. While the strong force is much stronger than the electromagnetic force, it is "screened" due to the non-perturbative nature of QCD, and hence acts over a much shorter distance than the EM force (which may act at infinite distance, as in light from distant galaxies). Nuclear showers therefore take more material to initiate and develop. The interation length characterizes the length scale of hadronic showers. The CMS tracker material budged in interaction lengths is shown in the right panel of 3.4.
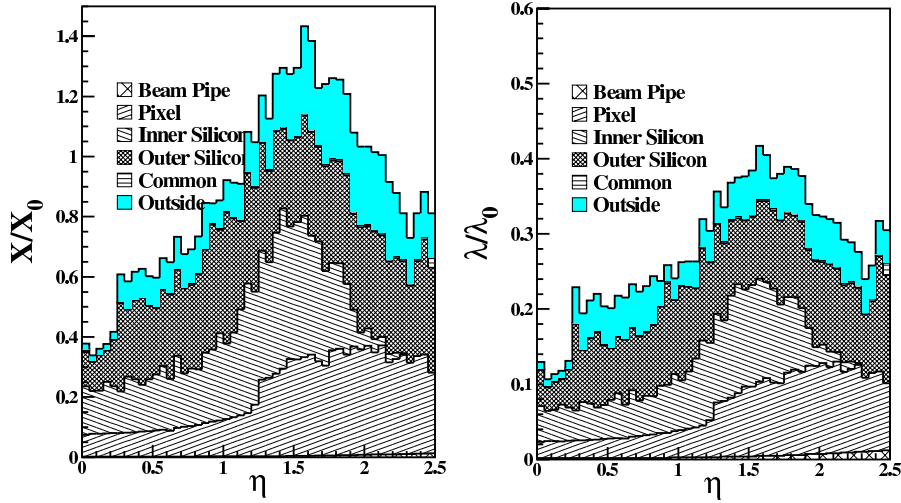
Figure 3.4: The CMS tracker material budget in radiation lengths (left) and interaction lengths (right).

3.1.2 Details of Tracker

Lastly, I will also summarize some basic technical details of the tracker. The size of a pixel (in the pixel detector) is $\approx 100 \times 150$ μm^2. In the intermediate region ($20 < r < 55$ cm), the silicon strip detectors are ≈ 10 cm $\times 90$ μm. For the outer tracker ($r > 55$ cm), the particle flux is low enough that the strip size can be increased to ≈ 25 cm $\times 180$ μm.

The three barrel pixel layers are at radii (r) of 4.4, 7.3, and 10.2 cm, and have a length of 53 cm. The spatial hit resolution is rougly 10 μm for $r - \phi$ and 20 μm for z.

The tracker inner barrel (TIB) contains four layers at 20 cm $< r <$ 55 cm, and $|z| < 65$ cm. The first two layers are "stereo," meaning that they contain two layers which are perpendicular to one another in order to measure both $r - \phi$ and $r - z$. The hit resolution is in this detector is rougly 30 μm for $r - \phi$ and 230 μm for z.

Next, the tracker outer barrel (TOB) covers 60 cm $< r <$ 110 cm and $|z| < 110$ cm. The first two layers of the TOB are also stereo. The hit resolution is rougly 45 μm ($r - \phi$) by 530 μm (z).

The hit resolutions are determined by the size of the active layers as well as the ability to interpolate charge collection on neighboring readouts. The resolution in

$r - \phi$ is more important than that in z for determining, eg. primary and secondary vertex location and beamspot position, so CMS has chosen to trade the latter for the former in order to optimize cost.

The tracker end cap (TEC) extends from 120 cm $< |z| <$ 280 cm, and from 1.0 $< |\eta| <$ 2.4. The tracker inner disk (TID) is between the TIB and TEC, inside the TOB (see Fig. 3.3).

3.2   Electromagnetic Calorimeter

The electromagnetic calorimeter (ECAL) is primarily responsible for measuring the energy of electrons and photons. The momentum of electrons is also measured in the tracker, but the ECAL is the only detector capable of providing accurate measurement of photon energies (see Sec. 3.1.1). An overview of the CMS calorimeters is shown in Fig. 3.5, including the hadronic calorimeter described in Sec. 3.3.

The ECAL material is lead tungstate ($PbWO_4$) crystal which is chosen because it is transparent to optical light and also very dense (over 8 g/cm^3). Electrons and photons incident on the ECAL crystals initiate electromagnetic showers which cause them to convert all their energy into optical light. A dense material is desirable because electromagnetic showers will develop over shorter distances in denser material. In other words, density is correlated with radiation length. Also, a dense material allows the ECAL to fit inside of a smaller solenoid.

The light from the electromagnetic showers is then collected by avalanche photodiodes (APDs) which are mounted on the back of the crystals. The APD signal is then digitized and stored as an ECAL hit. By properly calibrating the APDs and using geometical algorithms combining nearby crystals, electrons and photons are reconstructed. Vacuum phototriodes (VPTs) are used for the ECAL endcap crystals.

An important physical principle which underlies the design of the ECAL is molière radius, which characterizes the transverse width of an electromagnetic shower. The molière radius is defined as the radius which contains on average 90% of the energy of the electromagnetic shower in the plane transverse to the direction of the incident particle. The molière radius of lead tungstate is 2.2 cm, which is also approximately the

transverse length of the ECAL barrel crystals.

This ensures that the shower from a single electron or photon is spread over the eight crystals neighboring the crystal upon which the particle is incident (in other words, a three-by-three block), improving energy and position resolution. The ring of crystals surrounding the three-by-three block will not receive much light from the incident photon. (Electrons are more complicated due to bremsstrahlung–see Sec. 3.4.1.) Similarly, the shower of a real photon is very rarely contained in a single crystal.

Such high ganularity is also essential for good di-photon mass resolution because knowing the angular position of the photon is necessary for mass determination. (Di-photon mass is a critical component of the search for the Higgs Boson.)

Because of this, CMS chose to trade ECAL material for better position resolution. As a result, many charged pions interact and even completely stop in the ECAL due to hadronic interactions. Because the ECAL is designed and calibrated for electromagnetic showers, its response to hadronic showers is very poor. Only roughly a third of the pion's energy is measured by the ECAL. For low energy pions, this is a large effect. High energy pions, on the other hand, will easily penetrate the ECAL and this is not a problem. But since low energy pions are common, overall this non-linearity is a major contributor to fake MET.

I will now summarize some details of the ECAL design. There are 61,200 crystals in the barrel and 7324 in each endcap; the crystals point toward the interaction point as shown in Fig. 3.6. The ECAL barrel (EB) sits immediately outside the tracker with an inner radius of 129 cm and covers $|\eta| < 1.479$. The crystals of the EB have a front face size of 0.0174 in $\delta\phi$ and $\delta\eta$, which corresponds to 2.2 cm square, and a length of 23 cm, which translates to 25.8 X_0. The ECAL endcap (EE) covers $1.479 < |\eta| < 3.0$, and starts at $z = 317$ cm. The crystal geometry in the ECAL endcap (EE) is arranged in $x - y$, as opposed to the $\eta - \phi$ geometry of the EB. The EE crystals are 29 cm square, and 22 cm deep (25 X_0). In both the EB and EE, there are about 1.5 to 2 interaction lengths. In front of the EE is a preshower which contains lead absorber (2-3 X_0) and silicon strip detectors.
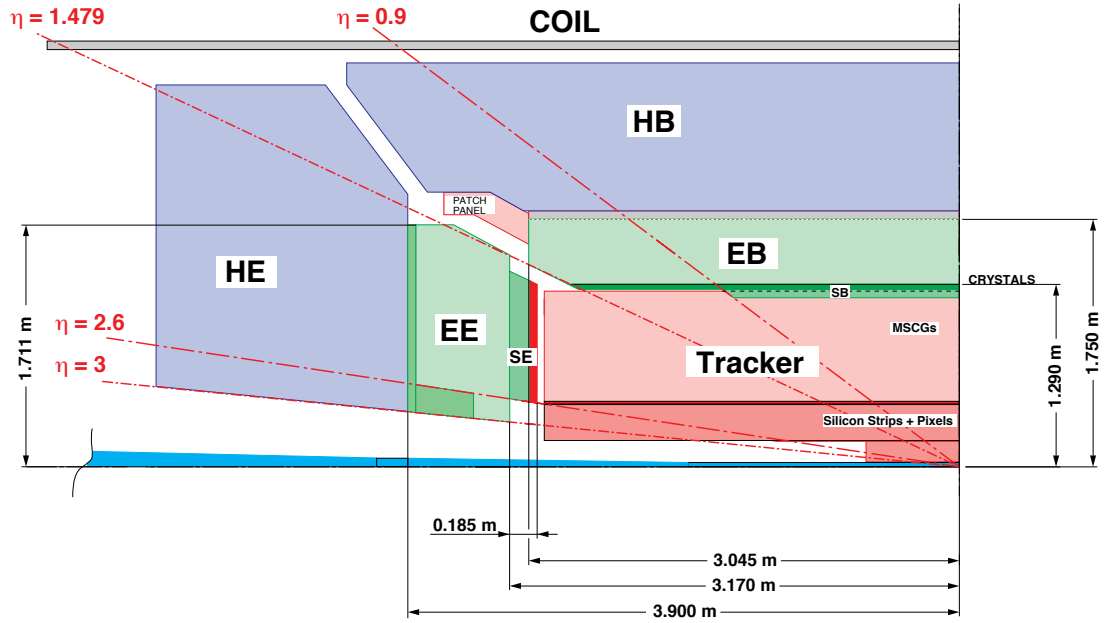
Figure 3.5: Overview of the CMS calorimeter systems (one quarter $r - z$ view). Shown are the ECAL barrel (EB) and endcap (EE), and the HCAL barrel (HB) and endcap (HE).

3.3 Hadronic Calorimeter

The main job of the hadronic calorimeter (HCAL) is to stop any particles which penetrate the ECAL and thereby measure their energy. As discussed in Sec. 3.2, the only such particles are hadrons (for a discussion of muons, see Sec. 3.4). The HCAL consists of layers of brass interspersed with layers of scintillating plastic. The layers of brass ensure that the shower continues to develop and eventually be contained within the HCAL. The scintillator measures ionization radiation. That is, as charged particles such as pions ($\pi^{\pm}$) pass through the scintillator volume, they ionize it, and that energy is converted to visible light. The visible light is then read out by hybrid photo-diodes (HPDs), combined across many channels, digitized, and finally converted into an energy reading.

Hadronic showers contain rougly one-third of their energy in neutral pions (π^0), which immediately decay into photons. Because brass has many radiation lengths, these photons (and their conversions) do not normally reach the scintillating material. The
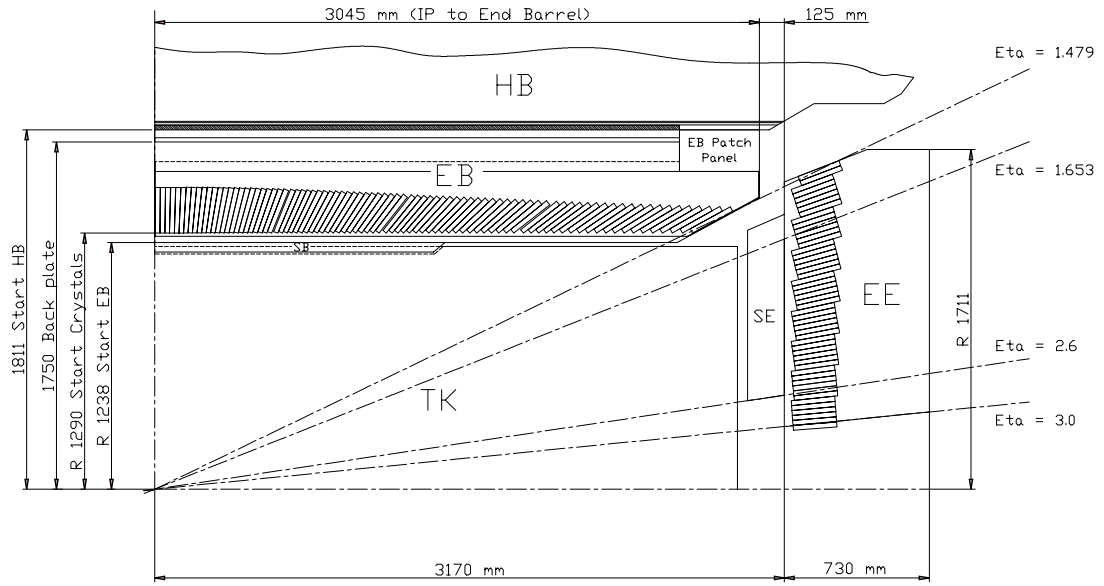
Figure 3.6: Detail of the CMS ECAL (one quarter $r - z$ view).

ability of calorimeters to correct for this effect is called "compensation." The CMS HCAL is not designed for online compensation, so it must be done offline at the level of jets or particle flow candidates (see Sec. 4.1.1). This is one of the main sources of non-linearity of the HCAL energy response, and hence a contributor to fake *MET*.

The η coverage of the HCAL is the same as the ECAL: $|\eta| < 3$. The HCAL hits have a one-to-one correspondence with calo towers. HCAL cells therefore also point toward the interaction region in the same way that ECAL crystals do. This allows for simple determination of variables like the ratio of hadronic to electromagnetic energy (H/E) for a given calo tower.

The HCAL is contained within the solenoid, and spans roughly $1.78 < r < 2.88$ m. For more details, see Fig. 3.5. The number of interaction lengths in the HCAL varies from 7 at $\eta = 0$ to about 11 at $\eta = 1.1$, and then decreases slightly to 10 at $\eta = 3.0$.

3.4   Muon Chambers

The muon chambers are the only major (barrel) sub-detector to lie outside of CMS's superconducting solenoid. This is because muons are the only particle with an

appreciable probability to traverse the material of the HCAL and the solenoid magnet. (Neutrinos do not interact at all, so they don't count.) Muon chambers are essentially a form of tracker: they measure the position of the muons at several consecutive radii, and by fitting these positions to a helix, the momentum of the muon is determined (see Sec. 3.1). I will first describe the general features of how muons interact–both in general and with the CMS detector (Sec. 3.4.1)–and then describe the CMS muon chambers (Sec. 3.4.2).

3.4.1   How Muons Interact with Matter

Muons have the same interactions as electrons (only weak and electromagnetic), but are about two hundred times heavier. This has very important implications for bremsstrahlung, since the power radiated by bremsstrahlung is proportional to m^{-4} (for acceleration perpendicular to velocity) or m^{-6} (for acceleration parallel to velocity).[32] Therefore, the minimum ratio of power radiated by muons to electrons is proportional to $(m_\mu/m_e)^4 \approx 200^4 = 1.6\ 10^9$. This is the main reason that muons are able to penetrate large amounts of material while electrons rapidly lose energy and stop.

The rate of energy loss (dE/dx) is also referred to as stopping power. The stopping power distribution for muons is fairly complicated and contains a variety of physical effects. For low energy muons ($E \lesssim 10$ MeV), energy is rapidly lost from interaction with electrons in the material. At intermediate energies, $0.1 \lesssim E \lesssim 100$ GeV, the stopping power is at a broad minimum as shown in Fig. 3.7. This is why muons at these energies are referred to as minimum ionizing particles, or "mips."

At higher energies ($E > 100$ GeV), both the bremsstrahlung and pair production contribution to the fractional energy loss grows with muon energy. The average contribution from photonuclear interactions is flat with muon energy, but rare photonuclear interactions can be hard, leading to large energy loss. For very high energy muons (1 TeV), according to simulation, the average energy loss in 1 m of iron is 23 GeV, but the median loss is 13 GeV–this is because the distribution has a very long tail.
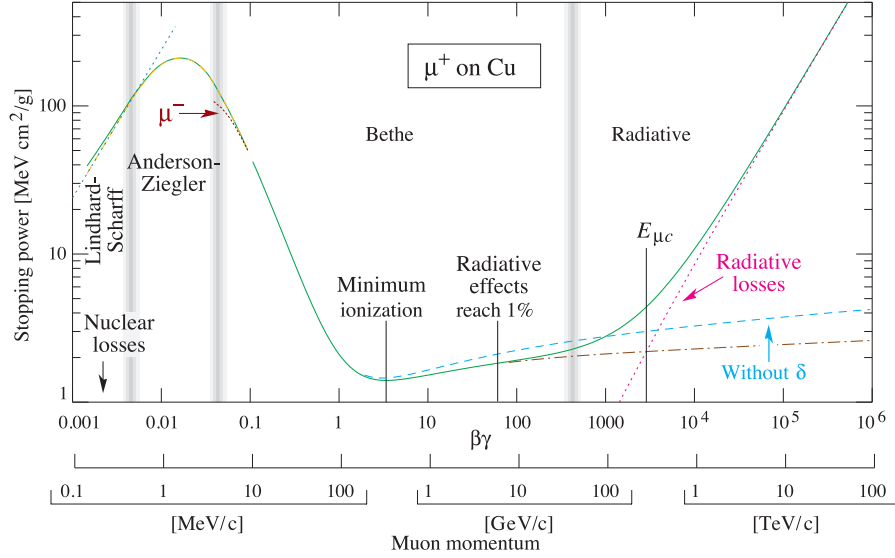
Figure 3.7: Stopping power (dE/dx) for positive muons in copper as a function of $\beta\gamma = p/mc$.

3.4.2 The CMS Muon System

The muon chambers contain three different detector technologies. The drift tubes (DTs) are ionization detectors. They consist of a wire surrounded by a concentric cylinder filled with gas. When a charged particle such as a muon passes through the gas, it ionizes some of the gas molecules and the freed electrons are collected on the wire. This technology has the advantage of fast readout, but at the cost of poor spatial resolution since the position along the wire is difficult to determine, and the wires are typically long (order meters). This is compensated for by using overlapping layers with an angle between them, so that if two layers have a hit, it should occur near the crossing point of the two layers. The drift tubes are contained in the barrel only, in $|\eta| \lesssim 1.2$ (see Fig. 3.8). This technology is used in the barrel only because the neutron background is low, the muon rate is low, and the magnetic field is low.

In contrast, in the endcaps, the muon and neutron rates are higher and the magnetic field is also higher, so cathode strip chambers (CSCs) are used here (up to η of 2.4). CSCs work in a way similiar to the DTs in that both are gas ionization detectors. However, the CSCs have a different geometry: the cathode and anode are plates with gas
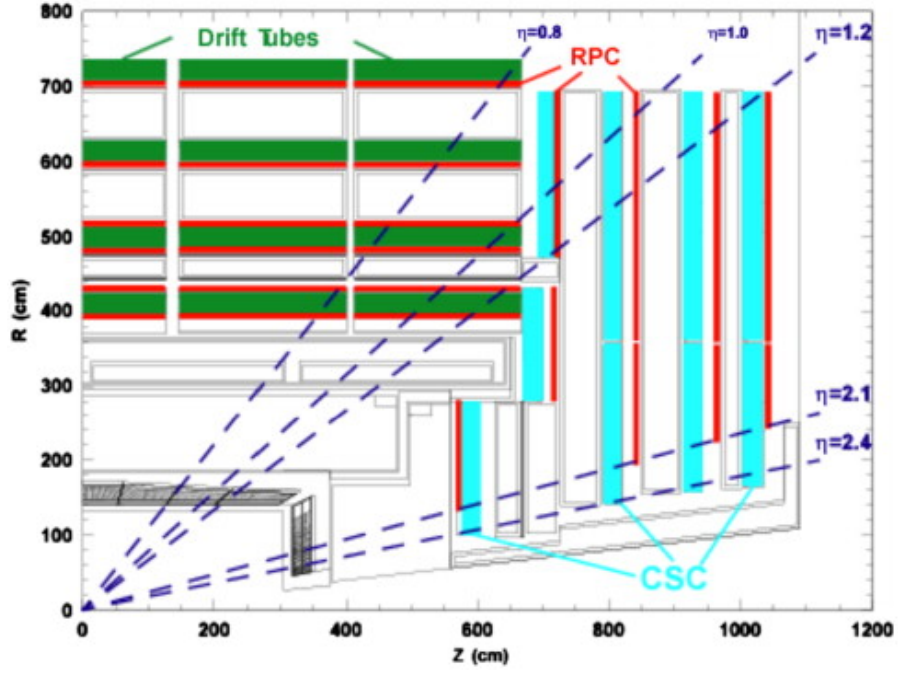
Figure 3.8: Overview of CMS muon system.

interspersed. A charged particle (muon) traverses the cathode, gas, and anode, creating an electron avalance followed by charge and image charge on the anode and cathode. This charge can be read out quickly, but at the cost of position resolution ($\sim 200 \mu m$, also roughly the same for the DTs).

In both the barrel and endcap ($|\eta| < 1.6$), resistive plate chambers (RPCs) are used to augment the other muon detectors. The RPCs can operate at high rates (up to 10 kHz/cm^2), providing a fast response with good time resolution but coarse position resolution. This allows them to identify the LHC bunch crossing. The RPCs operate in a similar fashion to the CSCs: a cathode and anode are separated by gas which is ionized by the muon traversing the detector.

Chapter 4

A Search for New Physics in a Final State of a Z Boson, Jets, and Missing E_T

The introduction of this thesis describes what it means to search for new physics in a final state of a Z boson, jets, and missing E_T (*MET*) at CMS. This chapter describes how it is done. The basic idea is to pick a final state and predict the contribution of all standard model processes to that final state. The specification of a final state of "Z boson, jets, and *MET*" is not a complete specification, but a very broad overview. Sec. 4.1 provides more details on exactly what this means.

This analysis is not a measurement of a parameter in a theory, but rather a search for new physics. As such, we do not need to know our backgrounds to excellent precision. It is enough to estimate the background to decent precision, and then look for excess yield above the expectation. In this particular case, we pick a kinematic variable, *MET*, and predict each background as a function of this variable. Any excess (or perhaps even deficit) of yield at any point in the *MET* distribution can be an indication of new physics. Given the nature of *MET*, we expect any excess to appear in the tail of the distribution. It is therefore very important to predict the tail of the distribution, not only its bulk.

There are three main backgrounds to this search: Z boson production associated with jets (Fig. 4.1), top anti-top pair production (which will be referred to as $t\bar{t}$, see Fig. 1.4), and diboson processes (Fig. 4.2). Each of these backgrounds must be predicted separately.
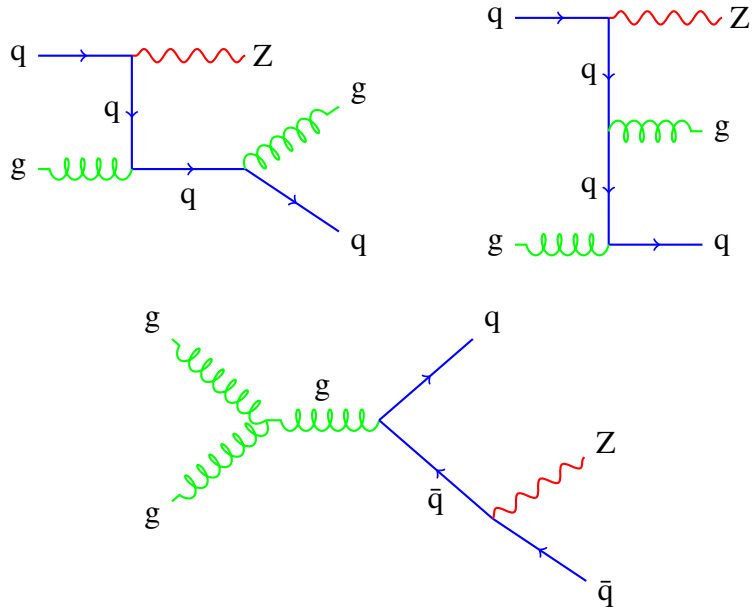
Figure 4.1: Three example Feynman Diagrams for the production of a Z with two jets. Note that these examples are a small subset of all possible Z plus two jet diagrams.

Sec. 4.1 outlines the final state of this analysis, as well as the object selections and signal regions. Sec. 4.2 describes the *MET* templates method which is used to predict the Z + jets background, and Sec. 4.3 describes how $t\bar{t}$ and other "opposite flavor backgrounds" are predicted. The diboson background is taken from Monte-Carlo (MC) simulated events (Sec. 4.4). For all MC discussed, the generators used are Pythia 6.4.22 [33] and Madgraph 5.1.1.0 [34], and generated events are then fed to a detailed simulation of the CMS detector based on Geant [35]. The results of this analysis are shown in Sec. 4.5. Finally, the interpretation is given in Sec. 4.6 and Sec. 4.7. This analysis is published in [19].
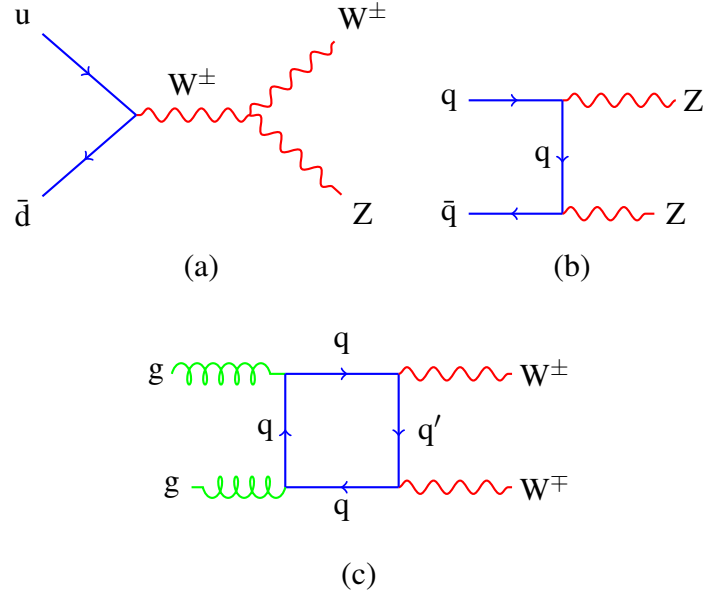
Figure 4.2: Feynman Diagrams for diboson processes. In (a), an example WZ production diagram is shown in the s-channel. WZ can also be produced in t-channel. In (b), ZZ production is shown in the t-channel; for ZZ, there is no s-channel diagram because there is no particle which could be in the propagator (see Sec. 2.2.3). In (c), a loop diagram shows an example of NLO WW production with two gluons as initial state particles. WW production can also proceed through tree-level diagrams like the ones in (a) and (b) for appropriate initial state quarks.

4.1   Specification of the final state

This section describes what is meant by the final state described above. The most important feature of the final state is the presence of a Z boson. The reason we want to select Zs is that they are a clean signature. The mass of the Z boson is approximately 91.2 GeV [32]. Because the Z has finite width, and because of finite lepton momentum resolution, we require the invariant mass of the dilepton system to be within 10 GeV of the Z mass, or from 81 to 101 GeV.

In some leptonic analyses, the presence of leptons which originate from a jet, or some particle other than the intended lepton are a background. These leptons are referred to as "fakes." In a Z analysis, fakes are not an issue for two reasons. First, the p_T of the leptons from a Z is sufficiently high that the rate of fakes at this p_T is relatively low. Second, the two selected leptons are required to have an invariant mass consistent with a Z decay. It is very unlikely that a real and fake lepton would make a Z mass because the Z mass window is relatively small and the mass distribution should be relatively flat. For these reasons, W + jets backgrounds are negligible.

4.1.1   Jets and *MET*

We require two or more jets in the final state for two reasons. First, the background prediction method we use requires jets in the final state. This is purely an experimental concern. Second, we expect new particles to be produced via the strong force (though this is not necessary, as will be discussed below) and therefore decay to jets. This is a theoretical bias. In principle, one could search for new physics in an inclusive Z sample with no jet requirements, but this would be more difficult because the rate of Z production with no jets is much greater than that of Z plus two jets. Each jet reduces the rate by roughly a factor of five, though this a very rough rule of thumb. This is demonstrated in the N_{jets} plot in Fig. 4.3.

Jet reconstruction is not described in detail anywhere in this thesis (see [36]). What follows is an extremely brief summary of a complicated topic. First, jets must be built out of candidate objects. These candidate objects may be calorimeter towers or particle flow particles. This is called *jet clustering*. There are many algorithms to do

this. The one currently in favor in CMS is called anti-K_T [37]. Jet algorithms typically have at least one parameter which characterizes the size of the jet in eta-phi space. The anti-K_T algorithm is not a fixed cone algorithm, so not all jets are the same size. The size paramter most commonly used by CMS, and by this analysis, is 0.5. We require our jets to have $p_T > 30$ GeV. This value is somewhat arbitrary but chosen as a balance between counting low p_T energy which are not part of the same hard collision which produced the Z boson and excluding such jets because the threshold is too high.

The third main feature of the final state is *MET*. The reason we require *MET* is similar to the reason we require jets. Experimentally, the Z plus jets *MET* distribution is a very steeply falling function (a sum of gaussians), so it is easy to suppress this background with a *MET* cut. One major goal of the LHC is to discover and study the dark matter particle, and we expect this particle to be "detectable" only as *MET*. However, we do not want to bias ourselves by assuming a *MET* distribution for a particular new physics scenario. We therefore measure the background *MET* distribution and check for new physics contributions in bins of *MET*. The lowest *MET* bin considered is *MET* > 30 GeV.

There is a reconstruction paradigm in CMS called *particle flow* [38]. I do not describe it in any detail, but I simply want to mention that the general idea or goal is to attempt to reconstruct each particle produced by the collisions. For example, tracks are matched to calorimeter deposits, and depending on the features of these, different "particles" are reconstructed. Particle flow is a set of many complicated algorithms, and, partially due to the fine tuning of these algorithms, generally yields accurate reconstruction of the "true" physics of the collision, at least according to Monte Carlo. The particle flow particles (or "candidates") are then clustered into jets to create particle flow jets, which are the ones used in this analysis. The negative vector sum of the p_Ts of all particle flow candidates is the particle flow *MET*, which is also the *MET* used in this analysis.

To summarize, the general features of the event selection used in this analysis are:

- A leptonically decaying Z boson: $Z \to \ell^+ \ell^-$ ($\ell = e, \mu$):

  - A pair of opposite charge and same flavor leptons

- The invariant mass of the dilepton pair is between 81 and 101 GeV

- In the case of more than two leptons passing the identification criteria described below, we select the pair with invariant mass closest to the Z mass

- At least two jets:

  - Jet $p_T > 30$ GeV, and $|\eta| < 3.0$

  - Particle flow jets are used

- *MET*

  - The search is conducted simultaneously in several *MET* bins

  - Particle flow *MET* is used
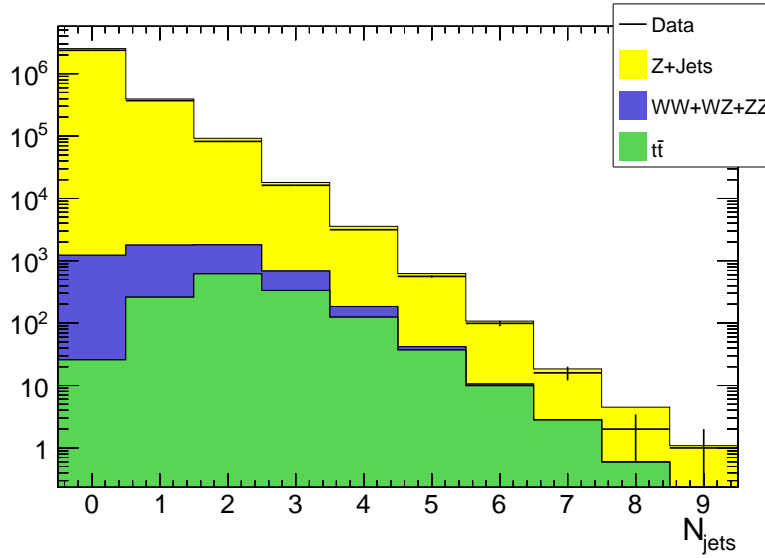
Figure 4.3: The N_{jets} distribution for Z events.

4.1.2 Lepton Selection

I will now briefly summarize more details about the electron and muon selection which is used in this analysis. For the signal region selection, two opposite sign, same flavor leptons are required, each with $p_T > 20$ GeV. We also use opposite sign, opposite flavor leptons as a control sample to predict certain backgrounds as will be described later (see Sec. 4.3). When referring to leptons, 'sign' means the sign of the electric charge, positive or negative, and flavor refers to the type of lepton: here, either electron (e) or muon (μ).

All dilepton events are triggered using one of a set of dilepton triggers. These triggers have a p_T requirement of 17 GeV for one lepton and 8 GeV for the second lepton. The offline requirement of $p_T > 20$ GeV is in the efficiency plateau of these triggers.

Due to the η coverage of the muon chambers (see Sec. 3.4), we require muons to be within $|\eta| < 2.4$. For electrons, the ECAL covers $|\eta| < 3.0$, however, detecting electrons requires a track, and the tracker stops at $|\eta| < 2.5$, so we require electrons to be in this region (see Sec. 3.2).

Aside from these fiducial requirements, we apply identification requirements which are essential to distinguish between prompt leptons and fake leptons. Prompt here means from the decay of a W or Z boson. Leptons from meson or baryon decays are never considered prompt. All of the above are summarized here:

- Electron selection:

    - $p_T > 20$ GeV

    - $|\eta| < 2.5$

    - The energy deposited in the HCAL must be less than 10% (7.5%) of the energy in the ECAL for the barrel (endcap)

    - Geometric requirements on the energy distribution of the ECAL crystals

    - The transverse impact parameter with respect to the nearest vertex is < 0.04 cm

    - The longitudinal impact parameter is less than 1 cm

- Isolation: The sum of the p_T of tracks and the transverse energy in both calorimeters in a cone of $dR = 0.3$ divided by the p_T of the electron is required to be less than 0.15. In the barrel only, a pedestal of 1 GeV is subtracted from the ECAL energy (to a minimum of zero)[39].

- No muon is allowed to be within $dR < 0.1$ of the electron (in order to prevent cases where a muon deposits energy in the ecal or overlaps with a photon or hadron)

- The following two requirements are implemented to reject conversion electrons (see Sec. 3.1.1): no more than one missing inner tracker hit is allowed, and we veto electrons with a reconstructed conversion vertex using a constrained vertex fit

- Muon selection:

  - $p_T > 20$ GeV

  - $|\eta| < 2.4$

  - Muon global fit is required to have χ^2 divided by number of degrees of freedom less than 10

  - Silicon track is required to have at least 11 hits

  - The ECAL energy in the calorimeter tower traversed by the muon cannot exceed 4 GeV

  - The HCAL energy in the calorimeter tower traversed by the muon cannot exceed 6 GeV

  - Quality criteria are applied to the track in the muon chambers

  - The transverse impact parameter with respect to the nearest vertex is < 0.02 cm

  - The longitudinal impact parameter is less than 1 cm

  - Relative transverse momentum error of silicon track used for muon fit is $\delta(p_T)/p_T < 0.1$

  - The same isolation requirement is applied as in the electron case (but no pedestal is subtracted from the ECAL energy).

4.1.3 Hypothesis Disambiguation

We allow for more than two leptons to be in selected events. If all three leptons are the same flavor, there is a choice of which pair to choose for the pair which make the Z.

Flavor here refers to the type of lepton. For the purposes of this analysis, there are two flavors: electrons (e) and muons (μ). A dilepton event can therefore be either same flavor (ee or $\mu\mu$) or opposite flavor ($e\mu$). All Z boson decays are same flavor, and therefore the signal regions used in this analysis are all same flavor.

The process of choosing which two of the three leptons make the Z is referred to as hypothesis disambiguation. The obvious criteria to use for this disambiguation is the invariant mass of the dilepton pair in question: the pair closest to the Z mass is therefore chosen.

For trilepton events, if there is a same flavor, opposite sign dilepton pair in the Z window, it is a signal event. If instead, the dilepton pair closest to the Z mass is opposite sign, opposite flavor, the event will enter the opposite flavor control sample instead of the signal sample. Same sign dilepton pairs are not used anywhere in this analysis.

4.1.4 Preselection

The preselection is the combination of all the requirements described above, except for MET. These are:

- A Z boson: a pair of opposite charge, same flavor leptons in the Z mass window (81-101 GeV)

- At least two jets, each with $p_T > 30$ GeV

To illustrate the properties of the preselection sample composition, the following figures and tables are provided. Fig. 4.4 shows the dilepton mass distribution (this cut is removed for this plot only) for the preselection, separately in the ee and $\mu\mu$ channels. These plots are meant to illustrate the relative contributions of Z + jets and $t\bar{t}$ in the preselection region, in addition to the mass distribution in $t\bar{t}$ events. Note that the x axis starts at 50 GeV because the Z + jets MC is generated with this lower bound. Tab. 4.1

shows the data and MC yields for the preselection region, and Tab. 4.2 shows the same but with the N_{jets} requirement changed from $N_{jets} \geq 2$ to $N_{jets} \geq 3$. This is shown because we also consider a signal region with this N_{jets} requirement.

The preselection is important because the *MET* Templates Method (see Sec. 4.2) is applied to all events passing the preselection.
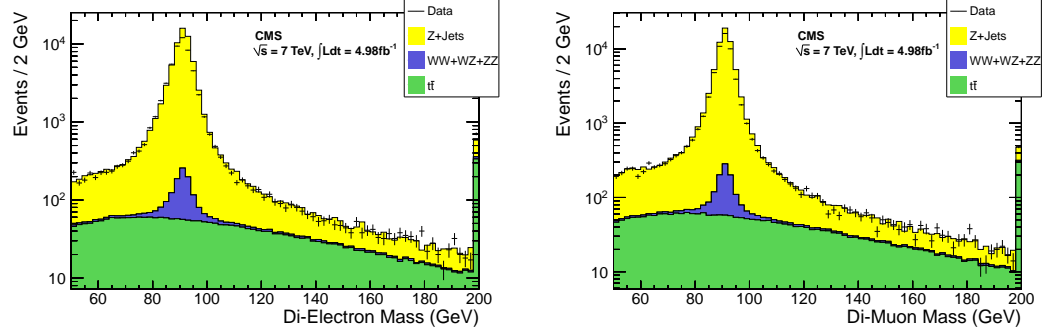
Figure 4.4: Dilepton mass distribution in the *ee* ($\mu\mu$) channel on the left (right) for events passing the preselection.

Table 4.1: Data and Monte Carlo yields for the preselection with $N_{jets} \geq 2$ for 4.98 fb^{-1}.

Sample	*ee*	$\mu\mu$	$e\mu$	tot
W + jets	10.8 ± 4.4	0.0 ± 0.0	8.5 ± 3.8	19.3 ± 5.8
WW	14.8 ± 0.5	17.2 ± 0.5	32.9 ± 0.8	64.9 ± 1.1
WZ	405.7 ± 1.8	411.7 ± 1.7	5.0 ± 0.1	822.4 ± 2.5
ZZ	313.3 ± 1.2	349.1 ± 1.2	0.8 ± 0.0	663.2 ± 1.6
Single Top	29.3 ± 1.2	26.1 ± 1.0	50.8 ± 1.5	106.2 ± 2.1
$t\bar{t}$	523.2 ± 2.6	529.0 ± 2.5	1056.7 ± 3.6	2108.8 ± 5.1
Z + jets	51051.4 ± 147.5	53149.1 ± 143.0	16.2 ± 2.6	104216.8 ± 205.4
Total MC	52348.5 ± 147.6	54482.2 ± 143.0	1171.0 ± 6.1	108001.6 ± 205.6
Data	49214	52757	1256	103227

Table 4.2: Data and Monte Carlo yields for the preselection with $N_{\text{jets}} \geq 3$ for 4.98 fb^{-1}.

Sample	ee	$\mu\mu$	$e\mu$	tot
WJets	0.0 ± 0.0	0.0 ± 0.0	1.7 ± 1.7	1.7 ± 1.7
WW	3.7 ± 0.3	4.0 ± 0.3	7.4 ± 0.4	15.2 ± 0.5
WZ	118.1 ± 1.0	117.8 ± 0.9	1.4 ± 0.1	237.3 ± 1.3
ZZ	71.0 ± 0.6	79.2 ± 0.6	0.2 ± 0.0	150.5 ± 0.8
Single Top	8.0 ± 0.6	7.0 ± 0.5	14.2 ± 0.8	29.1 ± 1.1
$t\bar{t}$	237.1 ± 1.7	238.3 ± 1.7	479.1 ± 2.4	954.4 ± 3.4
Z+Jets	9932.0 ± 65.1	10147.2 ± 62.4	5.3 ± 1.5	20084.4 ± 90.2
Total MC	10369.8 ± 65.1	10593.5 ± 62.4	509.3 ± 3.4	21472.6 ± 90.3
Data	9760	10356	506	20622

4.1.5   Signal Regions

The signal regions are chosen to be sensitive to generic new physics scenarios. As was mentioned in Sec. 4.1.1, *MET* is the main variable used in this analysis to discriminate between background and potential new physics. Because we want to remain sensitive to a variety of possible *MET* signatures, we choose a variety of signal region *MET* requirements (requirements are colloquially called 'cuts'). These are outlined:

- *MET* > 30 GeV : This low *MET* requirement is more of a control region than a signal region due to the large Z + jets background contribution. For this reason, it is a good validation of the *MET* templates background prediction.

- *MET* > 60 GeV : This is also a control region, and it is chosen near the point at which the Z + jets and $t\bar{t}$ contributions are roughly equal as further validation of the background predictions (see Fig. 4.5).

- *MET* > 100 GeV : This is the loosest *MET* cut which is considered as a signal region. It is chosen such that the Z + jets contribution is very small.

- *MET* > 200 GeV : This medium signal region is more sensitive to new physics contributions since the expected backgrounds are much lower here.

- *MET* > 300 GeV : A tight signal region, chosen where approximately one event is expected (from MC) in 5 fb^{-1}.
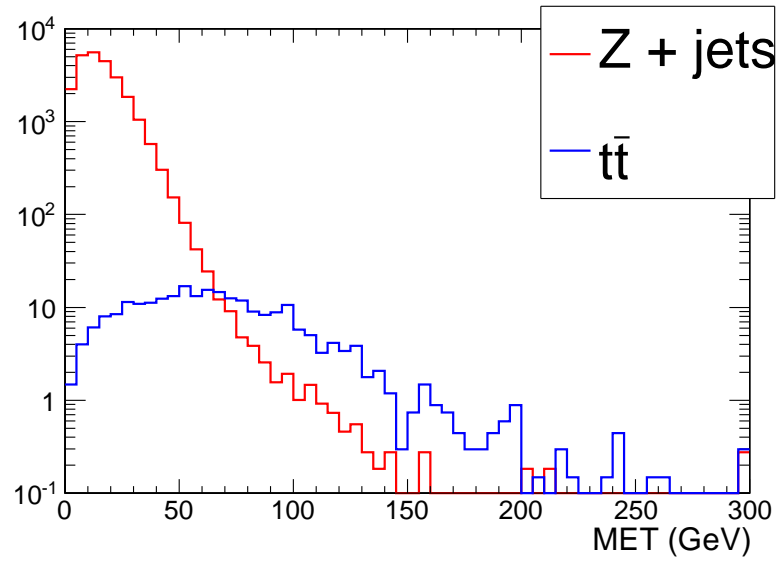
Figure 4.5: Distributions of *MET* in Z + jets and $t\bar{t}$ MC normalized to 1 fb^{-1}. Note that the *MET* distribution for Z + jets is a very steeply falling distribution characteristic of fake *MET*. The $t\bar{t}$, on the other hand, is real *MET*, and is much broader.

4.2 *MET* **Templates Method**

The *MET* templates method [40] is used to predict the contribution of Standard Model Z plus jets events to the signal regions used in this search. Because Z plus jets is a process with no *MET*, all the *MET* in these events is from mismeasurement of jets and leptons. This is called "fake" *MET*. There is in principle a small real *MET* contribution from non-prompt neutrinos from hadron decays, but this is negligible overall. Because lepton reconstruction and momentum resolution is quite accurate, *MET* from lepton mismeasurement is also negligible.The only remaining source of fake *MET* is therefore from jet mismeasurement, and it is this source of fake *MET* which the *MET* templates method is designed to predict.

The key assumption of this method is that the *MET* from jet mismeasurement can be parameterized in terms of the number of jets in the event (N_{jets}) and the scalar sum of jet p_Ts (H_T). This assumption is not perfect (for example, there may be some weak dependence on jet η), but after averaging over many events, it is accurate enough to give a good prediction.

Note that although the p_T threshold for N_{jets} counting is 30 GeV, the p_T threshold for H_T is reduced to 15 GeV. This is done because N_{jets} is used to determine the number of colored partons in the event, while H_T is used to determine the total energy in the event.

The method works as follows. First, a control sample must be chosen. For the analyses described in this thesis, photon plus jets events (γ + jets) and QCD events are used as two separate control samples. The exact selection of the control samples will follow, but explicit independence of the control and signal samples is guaranteed by a veto on any leptons in the control samples.

Once the control sample is selected, *MET* templates are constructed by plotting unit-normalized *MET* distributions in this sample in bins of N_{jets} and H_T. This array of *MET* plots is the basis of the background prediction. The prediction of the *MET* distribution in any given Z plus jets event is the template which corresponds to the *MET* and H_T in the Z plus jets event. In a sense, the templates constitute a set of probability density functions for *MET*. The prediction of the *MET* distribution in the entire Z plus jets sample is simply the sum of all the templates selected. Although the analysis signal

regions are formed by applying *MET* cuts to the Z events, the *MET* templates prediction must be made before making any *MET* cut to avoid bias.

4.2.1   Control Sample Triggering

In order to predict Z + jets events, one can use either QCD or γ + jets as a control sample. The control sample must have a higher rate than the signal sample so that the templates have sufficient statistics to sample the tail of the *MET* distribution. (So if one were trying to predict *MET* in γ + jets, one could use a QCD control sample, but not a Z + jets control sample.)

The γ + jets control sample is selected using single photon triggers, while the QCD control sample is selected using single jet triggers. In both cases, there are a set of triggers with varying p_T thresholds on the objects. For example, the trigger thresholds for the photon triggers are 20, 30, 50, 75, and 90 GeV. These thresholds are applied to the photon object at the L1 trigger level.

For the single jet triggers, at least one jet in the event is required to have an L1 online p_T greater than the trigger thresholds, which are 30, 60, 80, 110, 150, 190, 240, 300, and 370 GeV.

Each trigger is used to create a set of templates binned in H_T and N_{jets}. The triggers therefore become equivalent to a third dimension of template binning. For the photon triggers, the third dimension is the photon p_T. When making the prediction, the p_T of the Z determines which photon trigger is used. For the QCD prediction, the leading jet in the Z event is used to pick the set of templates constructed from the appropriate single jet trigger.

In both cases, offline (that is, at analysis time, after full reconstruction) cuts are applied to the objects to ensure that the triggers are fully efficient. This is necessary because the online and offline reconstruction is different, and the analysis is done with all offline quantities. The trigger thresholds and the corresponding offline selection are described below.

The online photon p_T trigger thresholds, together with the corresponding Z p_T threshold are:

- Photon $p_T > 20$ (Z $p_T < 33$ GeV)

- Photon $p_T > 30$ (33 GeV $<$ Z $p_T <$ 55 GeV)

- Photon $p_T > 50$ (55 GeV $<$ Z $p_T <$ 81 GeV)

- Photon $p_T > 75$ (96 GeV $<$ Z $p_T <$ 81 GeV)

- Photon $p_T > 90$ (Z $p_T >$ 96 GeV)

The single jet trigger online jet thresholds are listed below along with require-
ments on the offline lead jet p_T in parentheses:

- Jet $p_T > 30$ ($p_T <$ 80)

- Jet $p_T > 60$ (80 $\leq p_T <$ 100)

- Jet $p_T > 80$ (100 $\leq p_T <$ 130)

- Jet $p_T > 110$ (130 $\leq p_T <$ 180)

- Jet $p_T > 150$ (180 $\leq p_T <$ 220)

- Jet $p_T > 190$ (220 $\leq p_T <$ 270)

- Jet $p_T > 240$ (270 $\leq p_T <$ 330)

- Jet $p_T > 300$ (330 $\leq p_T <$ 400)

- Jet $p_T > 370$ ($p_T >$ 400)

4.2.2 Photon Selection

A pure photon sample is not necessary for the *MET* templates method. All that
is necessary is that the "photon object" is well measured. Because the CMS calorimeter
systems were designed to have better resolution for photons than for hadrons such as
charged pions (see Sec. 3.2), this is ensured by selecting photon objects which are pre-
dominantly electromagnetic. For example, if a jet happens to have a leading π^0 (which
decays to two photons) which contains most of the jet energy, it is still a viable photon
object for the purposes of the *MET* templates method.

Because *MET* is so important to this analysis, many of the selection criteria applied to photons are actually to ensure that the *MET* in the event is well reconstructed, especially with regard to the photon. The general strategy for doing this is to require that two different reconstruction algorithms yield consistent results. For example, the photon p_T is essentially just the supercluster p_T, while particle flow reconstruction yields an independent determination of the photon p_T which is in general different from the nominal p_T. Cases where the two are very disparate is cause for concern since one is likely to be wrong. Since there is no a priori way of telling which is right and which is wrong, and in particular, because a mistake in either may affect the *MET*, we reject events where the two p_Ts are very different.

We apply the following photon selection:

- $p_T > 22$ GeV

- $|\eta| < 2$

- The energy deposited in the HCAL must be less than 10% of the energy in the ECAL

- There is no track in the pixel detectors which points to the photon

- There must be a particle flow jet (pfjet) of $p_T > 10$ GeV matched to the photon within $dR < 0.3$. The matched jet is required to have a neutral electromagnetic energy fraction of at least 70%.

- The pfjet matched to the photon must satisfy (pfjet p_T - photon p_T) > -5 GeV. This removes a few rare cases in which "overcleaning" of a pfjet generated fake MET.

- We also match photons to calorimeter jets (calojets) and require (calojet p_T - photon p_T) > -5 GeV (the same requirement used for pfjets). This is to remove other rare cases in which fake energy is added to the photon object but not the calojet.

- We reject photons which have an electron of at least $p_T > 10$ GeV within $dR < 0.2$ in order to reject conversions from electrons from W decays which are accompanied by real MET.

- We reject photons which are aligned with the *MET* to within 0.14 radians in phi in order to protect against fake *MET* generated by the photon object.

4.2.3   Trigger Prescale Procedure

Each of the triggers listed in section 4.2.1 has a prescale associated with it. A prescale is a way for experiments to reduce the rate of triggers. Because the experiment is capable of recording a very small fraction of the total collision events delivered by the accelerator, not every event which satisfies the trigger requirement ("fires the trigger") is kept. The fraction of events which are kept is referred to as the prescale of the trigger. For example, a prescale of 30 means that one out of every thirty events which fires the trigger in question is kept.

The prescales must change between runs because the instantaneous luminosity also changes. Often, when the instantaneous luminosity increases, so does the pile-up. This effect, along with the changing prescales, should be taken into account when constructing the templates to provide a fair sampling of the *MET* distribution.

The procedure is to weight each control sample event by the event's prescale when constructing the templates. Only after all events are entered in this way is the normalization of each template to unity performed. This means that the events with higher prescales also get higher weight.

4.2.4   QCD *MET* Templates Recoil Correction

The advantage to using γ + jets to predict Z + jets is that in both cases a boson recoils against the jet system. The reason this is significant is that when all the jets are in one ϕ hemisphere, the propagation of jet mismeasurement to *MET* adds coherently. This scenario is more likely with a high p_T boson. For low p_T bosons, the effect is less pronounced since the jet p_Ts are greater than the boson p_T. There is a very small bias due to the fact that the Z p_T may go to zero while there must be a minimum photon p_T.

The main reason this bias is so small is that we select Z + jets events with at least two jets of $p_T \geq 30$ Gev each. In such events, the Z normally has some p_T also.

For the QCD case, there is no boson: jets are the only reconstructed objects in the event. In the γ + jets case, there is the possibility that mismeasurement of the photon (γ) can produce *MET* which the *MET* templates method does not account for. In the QCD case, there is no such risk. However, it turns out that this effect is very small.

On the other hand, because the jets balance themselves in $r - \phi$ space, on average, jet mismeasurement will cancel out. This is in contrast to the γ + jets case where, because of the recoil of the jet system against the boson, jet mismeasurement adds coherently. This effect is much larger than the boson mismeasurement effect. It must therefore be corrected for using a *MET* smearing procedure.

Before correcting for this effect, its size must be measured in the γ + jets sample. This is done by plotting the quantity

$$\frac{MET_\parallel}{p_T{}^{photon}}$$

where $MET_\parallel$ is the component of the *MET* parallel to the photon p_T. The parallel component is used because we are interested in the effect of the jet system recoiling against the boson, and *MET* perpendicular to the boson cannot be affected by boson recoil. $MET_\parallel$ is normalized to the photon p_T because we are interested in the relative contribution of the recoil from the photon to the *MET*, and because this dimensionless quantity can be applied directly to the Z sample.

The ratio above is found to be gaussian and peaked at roughly -6%. This means that, on average, the *MET* has a bias which is 6% of the photon p_T. The parameters of the gaussians fit to the distribution, and therefore the recoil, do not depend strongly on the number of jets in the event, nor on the photon p_T.

The *MET* smearing procedure is the following. For each Z event, a trial *MET* vector is constructed whose magnitude is 6% of the Z p_T. Then the bins of the template are looped over. For each bin, the trial *MET* vector is added to the bin content to get a new *MET* value for that bin. The direction of the vector is averaged over all angles by repeating the procedure for fixed angles. This means that first, an angle of 10 degrees from the *MET* is chosen (the angle of the *MET* is arbitrary), then 20, etc, until 360 degrees are completed. This procedure yields a new template which is used to predict

the Z event in question. As always, the total prediction is formed by summing all the templates–here they are smeared templates–for every Z event.

4.2.5   Closure Test in MC

In order to gain confidence in this method and test its application in conditions which are well understood, the above procedure is applied to MC samples. The application of the background prediction procedure to MC is referred to as a "closure test." This section will describe the results of the closure test; the results on data will follow (See Sec. 4.5).

The main utility of the closure test, aside from gaining confidence in the method, is to evaluate the contribution of processes with real *MET* to the *MET* templates. These contributions come from several sources, and the main contributions are: Z + jets where the Z decays to two neutrinos, W + jets where the lepton is lost or below the p_T threshold for the lepton veto, and $t\bar{t}$ in the single lepton channel where the lepton is lost. In these examples, the photon object can either come from a jet faking a photon, or be radiated from a final state particle. The combination of all of these process is referred to as SM 'soup,' since they are all Standard Model processes.

These processes are the dominante contribution to the templates at high *MET*. However, this does not present a major problem because the yield from these processes is sufficiently low relative to normal γ + jets and QCD.

The results of these tests for γ + jets templates are shown in figure 4.6 and table 4.3 for $N_{\text{jets}} \geq 2$ and in figure 4.7 and table 4.4 for $N_{\text{jets}} \geq 3$. The results for QCD templates are shown in figure 4.8 and table 4.5 for $N_{\text{jets}} \geq 3$ and table 4.6 $N_{\text{jets}} \geq 4$. Lack of sufficient closure for the QCD $N_{\text{jets}} = 2$ sample motivated us to rely solely on the γ + jets templates for the prediction in this jet bin.

The results are used to derive systematics on the two background predictions. For γ + jets, we asses a 30% systematic independent of *MET*. For QCD, the closure is observed to degrade somewhat with *MET*, so a *MET* dependent systematic is warranted. For the QCD prediction for $N_{\text{jets}} \geq 3$, we assess systematics of 20, 30, and 100% for *MET* > 30, 60, and 100 GeV respectively. For the $N_{\text{jets}} \geq 4$ case, we use 20, 30, and 50% for the same *MET* cut values.
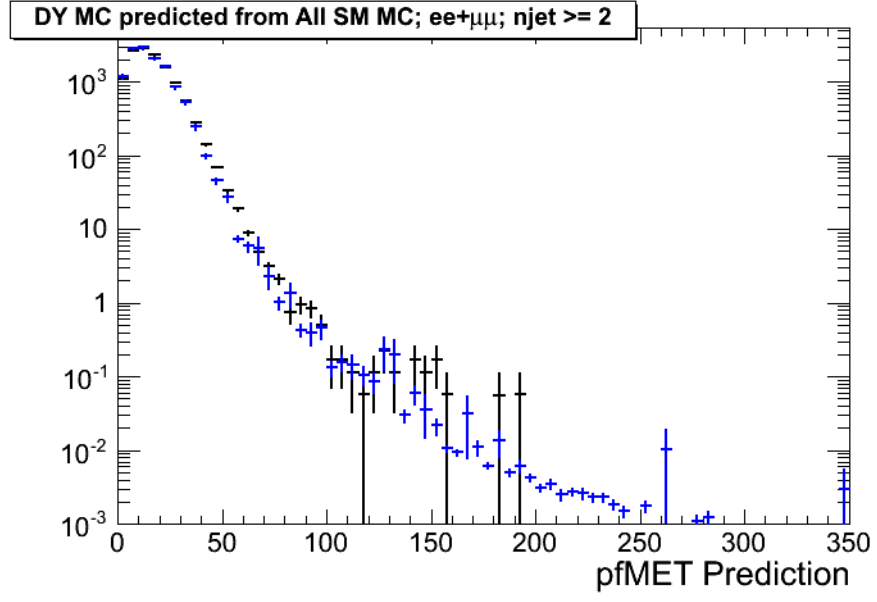
Figure 4.6: The MET distribution in Z plus jets MC (black) and prediction (blue) for $N_{\text{jets}} \geq 2$. See Table 4.3 for integrals.

Table 4.3: Results of MC closure tests for $N_{\text{jets}} \geq 2$. The first row shows the templates prediction only with all SM MC samples in the 'photon' sample (SM soup–see main text for details). The second row shows the yield in DY MC. The third and fourth rows show the results of the OF prediction in MC (Pred) as compared to MC yield in $t\bar{t}$ (Obs). The next two rows show the combined SM prediction from the templates method and OF prediction (Total Pred) as compared to DY plus $t\bar{t}$ yield (Total Obs). (The fifth row is the sum of the first and third and the sixth row is the sum of the second and fourth.) All uncertainties shown are statistical only.

MET cut	> 30 GeV	> 60 GeV	> 100 GeV	> 200 GeV
SM Soup	977 ± 55	19 ± 2.7	1.36 ± 0.19	0.05 ± 0.01
DY MC	1114 ± 7.9	24 ± 1.2	1.58 ± 0.30	0.00 ± 0.00
OF Pred	202.3 ± 0.3	126.2 ± 0.2	42.7 ± 0.1	1.95 ± 0.03
OF Obs	203.2 ± 0.8	126.5 ± 0.6	41.9 ± 0.3	1.52 ± 0.06
Total Pred	1179 ± 55	145 ± 2.7	44 ± 0.2	2.0 ± 0.03
Total Obs	1317 ± 8	151 ± 1.3	43 ± 0.5	1.5 ± 0.06
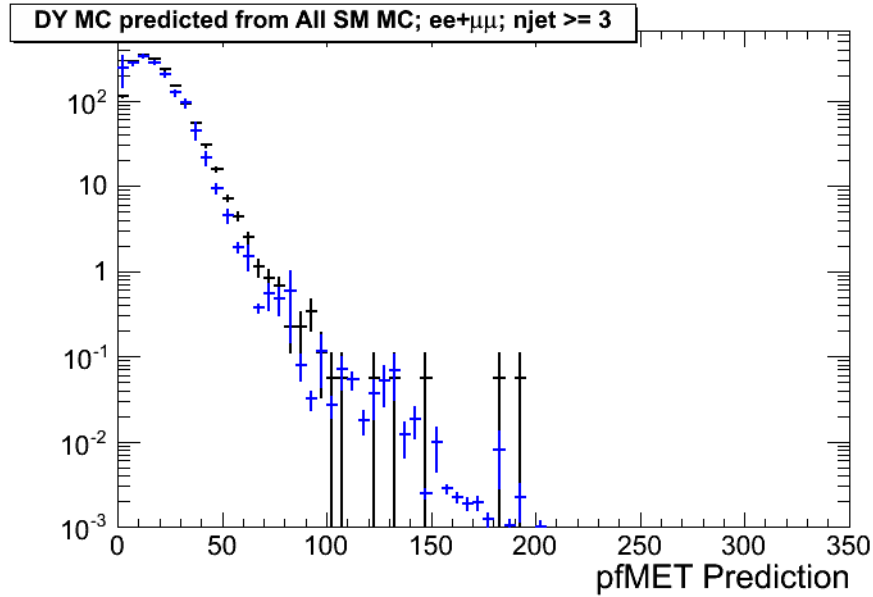
Figure 4.7: The MET distribution in Z plus jets MC (black) and prediction (blue) for $N_{\text{jets}} \geq 3$. See Table 4.4 for integrals.

Table 4.4: Results of MC closure tests for $N_{\text{jets}} \geq 3$. The first row shows the templates prediction only with all SM MC samples in the 'photon' sample (SM soup–see main text for details). The second row shows the yield in DY MC. The third and fourth rows show the results of the OF prediction in MC (Pred) as compared to MC yield in $t\bar{t}$ (Obs). The next two rows show the combined SM prediction from the templates method and OF prediction (Total Pred) as compared to DY plus $t\bar{t}$ yield (Total Obs). (The fifth row is the sum of the first and third and the sixth row is the sum of the second and fourth.) All uncertainties shown are statistical only.

MET cut	> 30 GeV	> 60 GeV	> 100 GeV	> 200 GeV
SM Soup	181 ± 17	4.1 ± 0.7	0.40 ± 0.06	0.01 ± 0.0
DY MC	211 ± 3.4	6.4 ± 0.6	0.4 ± 0.2	0.00 ± 0.0
OF Pred	93.6 ± 0.2	60.3 ± 0.2	22.6 ± 0.1	1.35 ± 0.02
OF Obs	92.8 ± 0.5	59.5 ± 0.4	21.9 ± 0.2	1.11 ± 0.06
Total Pred	275 ± 17	64 ± 0.7	23 ± 0.1	1.36 ± 0.02
Total Obs	304 ± 3.4	66 ± 0.7	22 ± 0.3	1.11 ± 0.06
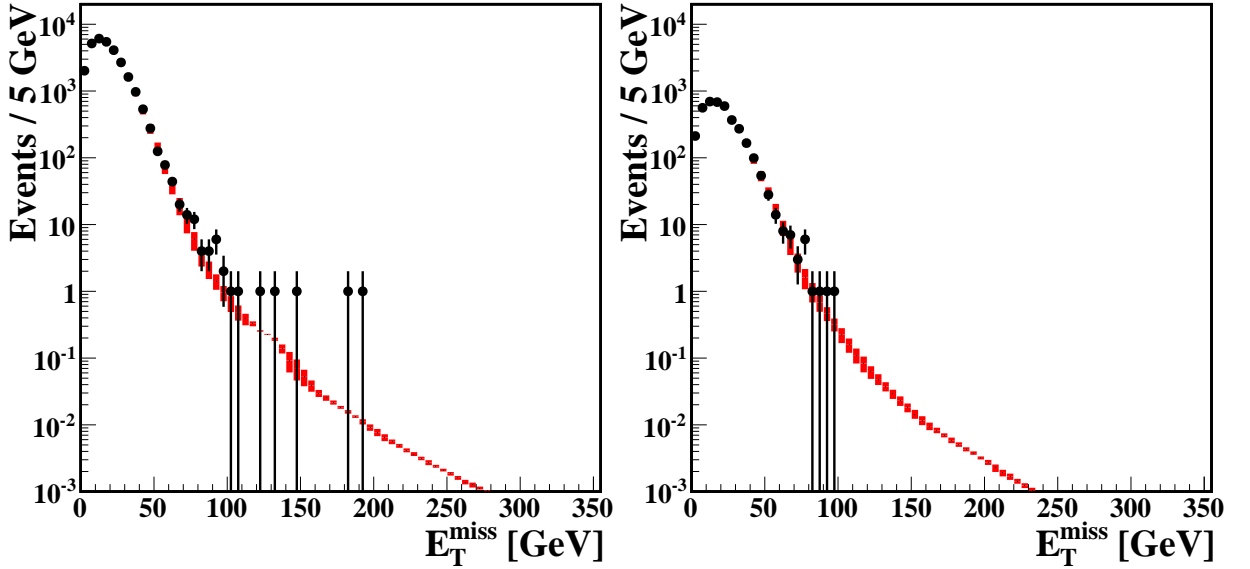
Figure 4.8: Predictions (red band) and MC yields (dots with error bars) for $N_J \geq 3$ (left) and $N_J \geq 4$ (right) in Powheg Z+jets MC. The red error band represents systematic uncertainty from the MET scale offset.

Table 4.5: Results of the QCD closure test for $N_{\text{jets}} \geq 3$. The uncertainty on the prediction includes only the uncertainty from the MET scale offset.

MET cut:	30 GeV	60 GeV	100 GeV	200 GeV	300 GeV
Z+jets (pred):	3599.2 ± 405.8	78.5 ± 23.0	3.0 ± 0.5	0.1 ± 0.0	0.0 ± 0.0
Z+jets (obser):	3720	113	7	0	0

Table 4.6: Results of the QCD closure test for $N_{\text{jets}} \geq 4$. The uncertainty on the prediction includes only the uncertainty from the MET scale offset.

MET cut:	30 GeV	60 GeV	100 GeV	200 GeV	300 GeV
Z+jets (pred):	627.9 ± 73.6	20.2 ± 6.1	0.8 ± 0.2	0.0 ± 0.0	0.0 ± 0.0
Z+jets (obser):	661	28	0	0	0

4.2.6 Systematic Uncertainty on the *MET* Templates Prediction

Based on the MC closure test results of Sec. 4.2.5, a 30% systematic uncertainty on the γ + jets *MET* templates prediction is assessed independent of *MET*, while a 100% systematic uncertainty on the QCD *MET* templates prediction is assessed for *MET* > 100 GeV.

In this section, we investigate other sources of systematic uncertainty besides MC closure for the γ + jets templates prediction. These sources include variation of the prediction as a result of a change in photon selection and as a function of the number of vertices (ie. pile up) in the control versus signal samples.

Photon selection can in principle affect the outcome of the γ + jets *MET* templates prediction if mismeasurement of the photon object contributes to *MET*. (See Sec. 4.2.2 for photon selection details.) In order to test for this effect, we vary two parameters of the photon selection: the hadronic over electromagnetic energy cut (H/E), and the neutral electromagnetic fraction cut (EMF). We then redo the prediction with these new selections and compare the new template prediction to the nominal one.

The number of vertices can affect the *MET* templates prediction because extra vertices contribute to fake *MET* in a random fashion. However, this effect is not significant if the distribution of the number of vertices is the same in the control and signal samples. The reason there may be a difference between the two is that the prescale of the photon triggers increased during the course of 2011 data taking. This means that the photon events were preferentially collected at earlier running time when there was less pile up. However, the overall pile up is modest throughout the entire 2011 data taking period. The average number of verties is ≈ 10 even at the highest instantaneous luminosity achieved in 2011. Furthermore, the prescale reweighting procedure (see Sec. 4.2.3) compensates for this effect.

Though we expect the pile up effect to be modest, we test for it by a reweighting procedure. This means that we plot the ratio of the number of vertices in Z versus γ events and weight each photon event by the ratio in the number of vertices bin for the γ + jets event.

The results of the above procedures are summarized in Tab. 4.7. (Because these studies were performed before the total dataset was collected, the prediction here does

not match that of the full dataset.) We choose to use the control region of $MET >$ 30 GeV for these studies because this region is dominated by Z + jets background and because the statistical uncertainty is lowest here.

The conclusions are as follows. The variation of the photon selection with H/E resulted in a negligible change in the prediction. The variation with EMF produced about a 10% change. The result of the number of vertices is a change of about 3%. We assume that these sources of systematics are independent of the systematic due to the MC closure test. Therefore, these uncertainties are each added in quadrature with the 30% systematic from the closure test resulting in an overall systematic uncertainty of 32% on the γ + jets MET templates prediction.

Table 4.7: Summary of variations in the MET templates prediction. The yields predicted by the MET templates method in the control region of MET > 30 GeV are shown, along with the relative difference with respect to the nominal prediction for several sources of variation in the template prediction.

	Prediction ($MET >$ 30 GeV)	Relative change
Nominal	10141	
Photon selection (H/E $<$ 0.05)	10146	0.00
Photon selection (H/E $<$ 0.01)	10090	0.00
Photon selection (EMF $>$ 0.8)	9991	0.02
Photon selection (EMF $>$ 0.9)	9103	0.10
Number vertices reweighting	10385	-0.03

The potential sources of systematic uncertainty are not necessarily limited to those mentioned above. For example, the jet flavor composition in γ + jets versus Z + jets can potentially contribute some systematic bias. Another effect which is more important is the hadronic recoil. This arises from difference in the p_T spectrum of the photon versus the Z. The low p_T component of this spectrum (ie., $p_T \lesssim 20$ GeV) is not an issue due to the jet requirements. However, at high boson p_T, there is not guaranteed to be good agreement between the Z + jets and γ + jets p_T spectra. This effect has been tested for by binning the templates in the boson p_T. The effect is very small in some regions of phase space, but potentially large in other regions. Due to the complexity and

convolution of these effects with others discussed above, we choose not to try to quantify this source of systematic uncertainty. Instead, we assume that the systematics assessed as a result of the MC closure test sufficiently covers these as well as other potentially unforseen sources of systematics.

4.2.7   Signal Contamination

"Signal contamination" refers to the alteration of a background prediction due to the presence of unknown signal events in the background dominated control regions. For example, the *MET* templates prediction would increase if a new physics signal caused yield in the γ + jets + *MET* final state. This increase could obscure a new physics signal in the Z + jets + *MET* final state.

Signal contamination can only be quantitatively assessed in a well defined new physics scenario, and is fundamentally model dependent. In general, signal contamination is normally not a problem because any new physics signal must have a low cross section relative to the standard model processes which constitute its background (otherwise it would be easily discovered).

For the *MET* templates, the safeguard against signal contamination is the very large cross section of the γ + jets process. The use of two separate control samples (γ + jets and QCD) also protects against signal contamination since it is very unlikely both samples would be contaminated, and a comparison of the two predictions would reveal a discrepancy.

Nevertheless, due to pressures from within CMS, a quantitative check was made for signal contamination for the models LM4 and LM8 (see Sec. 4.6.1). The contamination was found to be negligible (less than 1%).

For the opposite flavor prediction (see Sec. 4.3) there is a larger chance of contamination if both opposite flavor and same flavor leptons are produced in a particular model. For this prediction, the effect of signal contamination is taken into account in the limit setting described in Sec. 4.6.1.

4.2.8 MC Comparison

The *MET* templates background prediction is necessary because *MET* mismeasurement is a random process which is very difficult to simulate in MC. It not only depends on many details of the detector simulation, but also on things like underlying event, etc. This is demonstrated by comparing the MC prediction to the results of the *MET* templates prediction in Tab. 4.8. In order to compare to data, I also show the $t\bar{t}$ prediction as obtained using the procedure of Sec. 4.3 and the diboson prediction from MC (see Sec. 4.4).

The Z + jets MC prediction is roughly 30% lower than the *MET* templates prediction. The systematic uncertainty described above is also 30%. So although the MC and templates predictions are consistent to within roughly 1σ, the template prediction agrees better with the observed yield. It is perhaps conservate to assign a 30% systematic. The $t\bar{t}$ MC also under-predicts as compared to the data-driven prediction.

Table 4.8: Comparison of data-driven and MC predictions for the regions $MET > 30$, 60, 100, 200 and 300 GeV for $N_{\text{jets}} \geq 2$. The MET templates prediction for the Z + jets background (Templates Pred) is compared to Z + jets MC (Z + jets MC). Next, the data-driven prediction for the opposite-flavor background (OF Pred) is compared to $t\bar{t}$ MC. The WZ and ZZ diboson backgrounds are taken from MC (VZ MC). (Uncertainties on the Z + jets MC and $t\bar{t}$ MC are statistical only while a 50% systematic uncertainty is assessed on the VZ MC as explained in Sec. 4.4.) The MET templates and opposite-flavor data driven predictions are added to the VZ MC in the row Data-Driven Pred. This is compared to the total MC prediction (MC Pred) and the observed data.

	$MET > 30$ GeV	$MET > 60$ GeV	$MET > 100$ GeV
Templates Pred	15070 ± 4825	484 ± 156	36 ± 12
Z + jets MC	9941 ± 100	263 ± 16	29 ± 5
OF Pred	1116 ± 101	680 ± 62	227 ± 21
$t\bar{t}$ MC	895 ± 30	557 ± 24	185 ± 14
VZ MC	269 ± 135	84 ± 42	35 ± 17
Data-Driven Pred	16455 ± 4828	1249 ± 174	297 ± 30
MC Pred	11105 ± 171	904 ± 51	249 ± 23
Data	16483	1169	290

	$MET > 200$ GeV	$MET > 300$ GeV
Templates Pred	2.4 ± 0.9	0.4 ± 0.3
Z + jets MC	4.0 ± 2.0	0.8 ± 0.5
OF Pred	11 ± 3.2	1.6 ± 0.6
$t\bar{t}$ MC	6.7 ± 2.6	0.6 ± 0.8
VZ MC	5.3 ± 2.7	1.2 ± 0.7
Data-Driven Pred	19 ± 4.3	3.2 ± 1.0
MC Pred	16 ± 4.2	2.6 ± 1.2
Data	14	0

4.3 Opposite Flavor Background Prediction

At high MET, $t\bar{t}$ is the dominant background in this analysis. Fortunately, it has a natural data control sample: opposite flavor (OF) events.

OF events can originate from a variety of processes. The first set of processes are flavor-symmetric in the sense that opposite flavor and same flavor events occur at equal rates:

$$N_{e\mu} = N_{ee} + N_{\mu\mu}$$

This condition is a result of having two identical particles (Ws) which each decay to either electrons or muons at the same rate. This is the case for $t\bar{t}$ as well as WW production, single top production in the tW channel, and the $Z \to \tau\tau$ process. All these backgrounds are predicted by this procedure.

The only assumption of this method is that the dilepton mass and MET distributions are the same in the control and signal samples. This is illustrated in Fig. 4.9.

4.3.1 OF Prediction Procedure

There are only two tricks necessary to make this prediction. (It is much simpler than the MET templates method of Sec. 4.2.) The first trick is how to deal with the dilepton invariant mass cut, and the second is how to take the lepton efficiencies into account.

If one applies the same dilepton invariant mass cut (ie, $81 < m_{\ell\ell} < 101$) to the opposite flavor sample, the statistics will be limited. Instead, the dilepton mass cut can be removed and replaced by a scale factor taken from MC, called K, which is simply the fraction of opposite flavor events inside the Z mass window. The value of K is found to be 0.16. Its uncertainty will be discussed in Sec. 4.3.2.

The lepton efficiencies must be taken into account because they are different for electrons and muons. The only quantity which enters is the ratio of muon to electron efficiencies (ε). We denote the ratio as R, which is measured in inclusive Z events:

$$R_{\mu e} = \varepsilon(\mu)/\varepsilon(e) = \sqrt{\frac{N_{\mu\mu}}{N_{ee}}} = 1.07$$
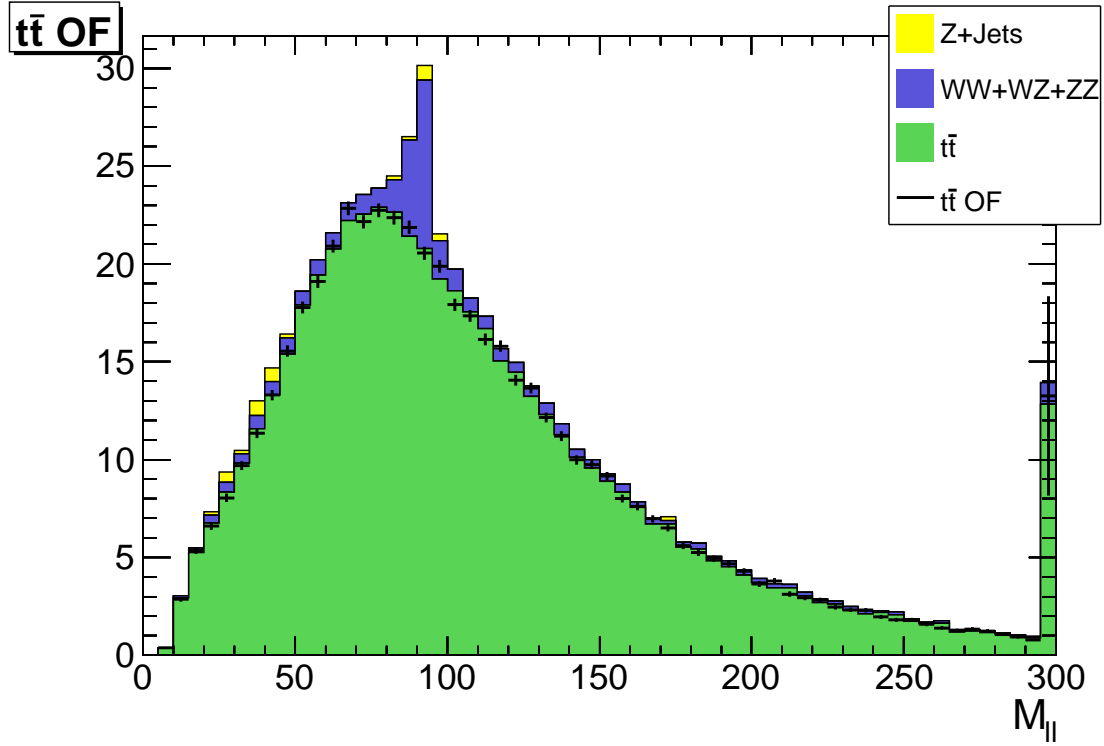
Figure 4.9: MC dilepton mass distribution for events passing the loose signal region selection ($MET > 100$). The solid histograms represent the yields in the same-flavor final state for each SM contribution, while the black data points ($t\bar{t}$ OF) indicate the sum of the $t\bar{t}$ MC contributions in the opposite-flavor final state. The two distributions agree closely.

Here $N_{\mu\mu}$ (N_{ee}) are the number of $Z \to \mu\mu$ (ee) events, and the square root is present because there are two leptons per Z event, and efficiencies multiply. The statistical uncertainty on R is negligible due to the large number of Drell-Yan events, and the systematic on this quantity will be discussed in Sec. 4.3.3.

We therefore have the following equations for the OF prediction:

$$N_{pred}(\mu\mu) = \frac{1}{2}N(e\mu)KR_{\mu e}$$

$$N_{pred}(ee) = \frac{1}{2}N(e\mu)KR_{e\mu}$$

where $R_{e\mu} = \frac{1}{R_{\mu e}}$, $N(e\mu)$ is the total number of OF events above some MET cut, and N_{pred} is the prediction for the number of same flavor events above that same MET cut.

For the analysis described here, K and R have no *MET* dependence, and hence are constants. We will see that in a modification to this analysis, the dependence of K on *MET* will need to be evaluated (see Sec. 5.2.2).

4.3.2 Systematics on OF Prediction: K

Though we expect K to be well modeled in MC, there is in principle a source of systematic uncertainty associated with imperfect modeling of this quantity in MC. In order to assess such an uncertainty, we compare K in data and $t\bar{t}$ MC as a function of *MET* in Fig. 4.10. Based on these results, we use $K = 0.16 \pm 0.01$, or a relative uncertainty of $\approx 6\%$.
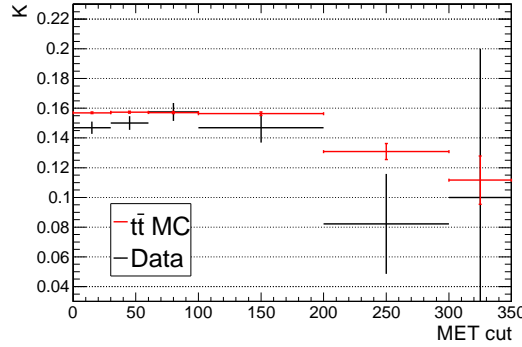
Figure 4.10: K (the ratio of opposite flavor events inside the Z mass window to the total number of opposite flavor events) vs. the MET cut in data and $t\bar{t}$ MC.

4.3.3 Systematics on OF Prediction: R

The quantity R has a potential source of systematic uncertainty associated with it due to the fact that we extract R from Z events and apply it to $t\bar{t}$ events. Though leptons from these two process are fundamentally indistinguishable, their p_T spectrum is different. Fig. 4.11 shows the p_T spectrum for leptons in Z and $t\bar{t}$ MC, and also shows the quantity R in each sample. Based on the variation of R between Z and $t\bar{t}$, we use $R = 1.07 \pm 0.07$, which corresponds to a relative uncertainty of $\approx 7\%$.

Combining the systematic uncertainties due to R and K, we arrive at a total relative systematic of 9%.
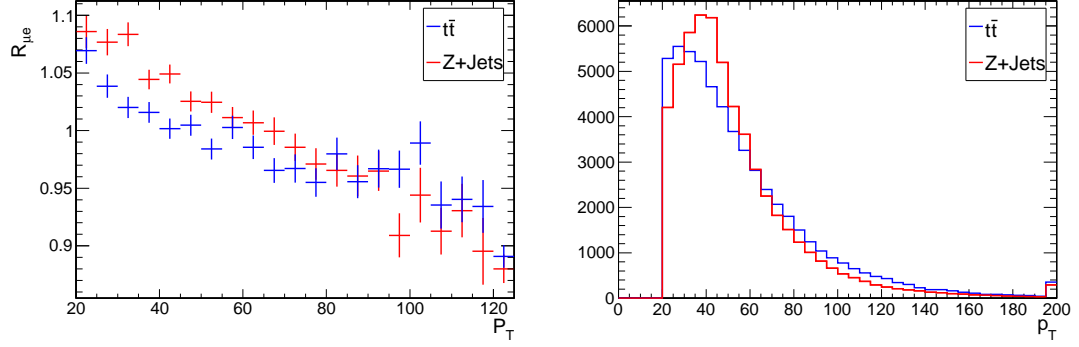
Figure 4.11: $R_{\mu e} = \varepsilon(\mu)/\varepsilon(e)$ (the ratio of muon to electron ID + isolation efficiencies) vs. lepton p_T in Z and $t\bar{t}$ MC (left), lepton p_T distributions for the same samples (right).

4.4 Diboson Background Prediction

There are three main diboson processes: WW, WZ, and ZZ (see Fig. 4.2). Of these, the WW process is the only one which is flavor symmetric, and hence this background is predicted using the OF prediction procedure described in Sec. 4.3.

For WZ and ZZ, we use MC to predict the yield of these processes in the signal regions of this analysis. Both of these processes enter a *MET* selection via true *MET* from neutrinos, and hence we expect the MC to do reasonably well in quantitatively predicting these yields. For the WZ case, the *MET* comes from a leptonic W decay, and for ZZ, from one of the Zs decaying to two neutrinos.

Note that there is a small fraction of WZ in which both bosons decay leptonically, but one of the leptons from the Z decay is lost. This is then a flavor-symmetric component of the WZ background. This is between two and three percent of the total WZ background.

In order to test the validity of the MC and to assess a systematic uncertainty on the MC prediction, we validate the WZ and ZZ MC in tri-lepton and quad-lepton samples as described in Secs. 4.4.1 and 4.4.2.

4.4.1 WZ MC validation Studies

A pure WZ sample can be selected in data with the requirements:

- Exactly 3 $p_T > 20$ GeV leptons passing analysis identication and isolation requirements (see Sec. 4.1.2)

- 2 of the 3 leptons must fall in the Z window of 81-101 GeV

- *MET* > 30 GeV (to suppress Drell-Yan)

The data and MC yields passing the above selection are in Tab. 4.9. Based on these results we assess an uncertainty of 50% on the *WZ* expected background in our signal regions. A data vs. MC comparison of kinematic distributions is given in Fig. 4.12. We compare the following distributions in data vs. MC: number of jets, *MET*, and Z p_T. High *MET* values in *WZ* and *ZZ* events arise from highly boosted W

or Z bosons decaying leptonically, and we therefore check that the MC does a reasonable job of reproducing the p_T distribution of the leptonically decaying Z. The data vs. MC agreement in all of these quantities is reasonable, providing a validation of the MC expectation for the background in our signal regions.

Table 4.9: Data and Monte Carlo yields for the WZ preselection for 3.5 fb^{-1}.

Sample	ee	$\mu\mu$	$e\mu$	Total
$t\bar{t}$	0.8 ± 0.4	0.4 ± 0.3	1.0 ± 0.4	2.2 ± 0.6
Z + jets	5.2 ± 1.5	5.1 ± 1.4	0.0 ± 0.0	10.3 ± 2.1
ZZ	5.1 ± 0.0	5.8 ± 0.0	0.4 ± 0.0	11.3 ± 0.1
WZ	77.4 ± 0.5	88.7 ± 0.5	5.3 ± 0.1	171.4 ± 0.7
Total SM MC	88.6 ± 1.6	99.9 ± 1.5	6.6 ± 0.4	195.1 ± 2.3
Data	113	110	5	228
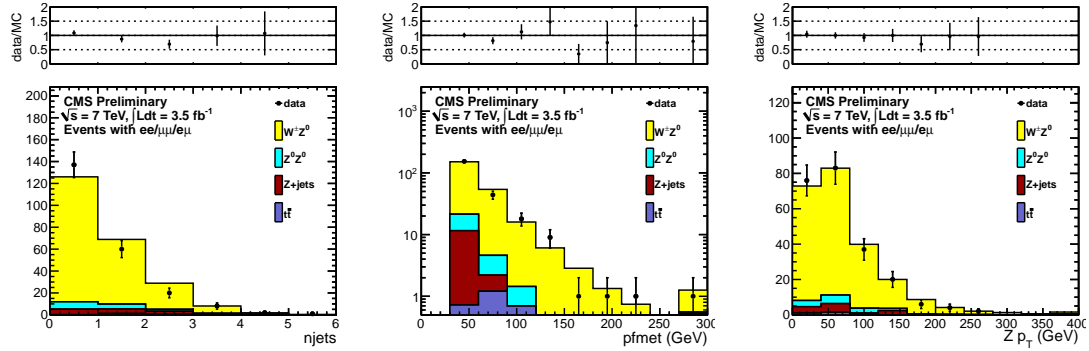
Figure 4.12: Data vs. MC comparisons for the WZ selection discussed in the text for 3.5 fb^{-1}. The number of jets, missing transverse energy, and Z boson transverse momentum are displayed.

4.4.2 ZZ MC validation Studies

A pure ZZ sample can be selected in data with the requirements:

- Exactly 4 $p_T > 20$ GeV leptons passing analysis identication and isolation requirements (see Sec. 4.1.2)

- 2 of the 4 leptons must fall in the Z window 81-101 GeV (this requirement is not necessary on the other lepton pair because there are no other substantial processes which produce four leptons)

The data and MC yields passing the above selection are in Tab. 4.10. Based on these results we assess a 50% uncertainty on the ZZ background expectation in the signal regions due to the statistical precision of the data sample of 25 events. A data vs. MC comparison of kinematic distributions is given in Fig. 4.13. We compare the following distributions in data vs. MC: number of jets, MET, and Z p_T. High MET values in WZ and ZZ events arise from highly boosted W or Z bosons decaying leptonically, and we therefore check that the MC does a reasonable job of reproducing the p_T distribution of the leptonically decaying Z. The data vs. MC agreement in all of these quantities is reasonable, providing a validation of the MC expectation for the background in our signal regions.

Table 4.10: Data and Monte Carlo yields for the ZZ preselection for 3.5 fb^{-1}.

Sample	ee	$\mu\mu$	$e\mu$	Total
$t\bar{t}$	0.0 ± 0.0	0.0 ± 0.0	0.0 ± 0.0	0.0 ± 0.0
Z + jets	0.0 ± 0.0	0.0 ± 0.0	0.0 ± 0.0	0.0 ± 0.0
ZZ	10.0 ± 0.1	12.1 ± 0.1	0.7 ± 0.0	22.8 ± 0.1
WZ	0.0 ± 0.0	0.0 ± 0.0	0.0 ± 0.0	0.0 ± 0.0
Total SM MC	10.0 ± 0.1	12.1 ± 0.1	0.7 ± 0.0	22.8 ± 0.1
Data	9	15	1	25
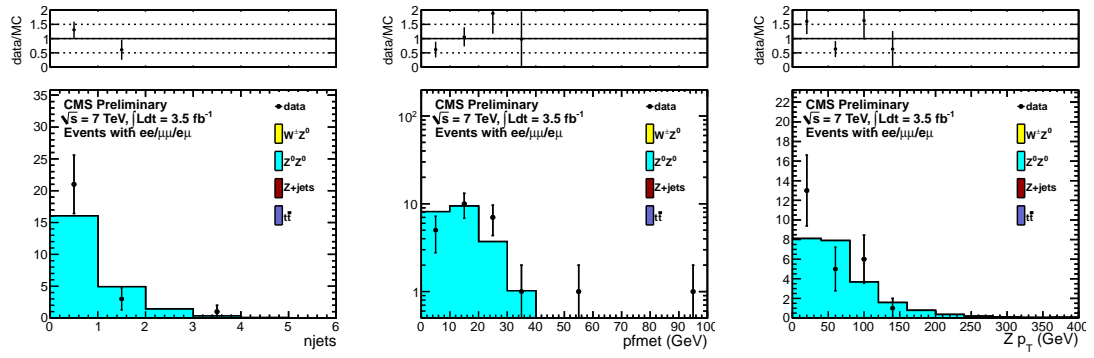
Figure 4.13: Data vs. MC comparisons for the ZZ selection discussed in the text for 3.5 fb^{-1}. The number of jets, missing transverse energy, and Z boson transverse momentum are displayed.

4.5 Experimental Results

The analysis strategy and methodology described in Secs. 4.1 through 4.4 are executed on the full 2011 dataset collected by CMS. Because the pileup conditions changed between runs 2011A and 2011B, we perform all of the above background predictions separately for the two runs and then sum the results to get the prediction for the full 2011 dataset. The results are quoted for all the signal regions described in Sec. 4.1.5.

In all signal regions, the data is in agreement with the prediction, so we conclude that there is no evidence for new physics.

We place 95% confidence level (CL) upper limits on the non-SM contributions to the yields in the signal regions, using a hybrid frequentist-bayesian CLs method with nuisance parameters and the signal strength maximizing the ratio of the signal-with-background and background-only likelihood [41, 42]. We also quote the NLO expected yields for the SUSY benchmark processes LM4 and LM8 (see Sec. 4.6.1). These yields are corrected for the impact of signal contamination by subtracting the expected contribution to the OF background estimate. The contribution to the *MET* templates background estimate is negligble (see Sec. 4.2.7).

The results are displayed in Figs. 4.14 and 4.15 and Tabs. 4.11 and 4.12 for inclusive *MET* bins, and Tabs. 4.13 and 4.14 for exclusive *MET* bins.
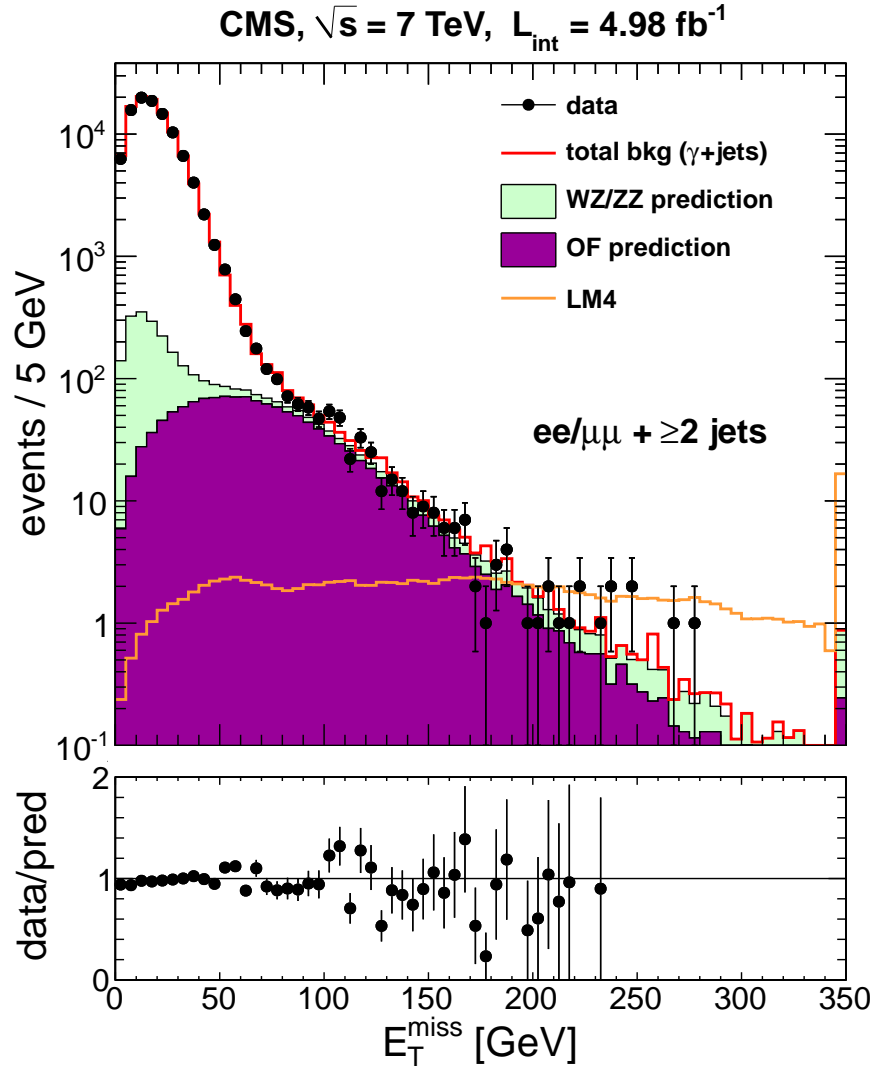
Figure 4.14: The observed *MET* distribution for events with $N_{\text{jets}} \geq 2$ for data (black points), predicted OF background from MC normalized to the $e\mu$ yield in data (solid purple histogram), $WZ + ZZ$ background (solid green histogram) and total background including the Z + jets predicted from γ + jets *MET* templates. The ratio of the observed and total predicted yields (data/pred) is indicated. The error bars indicate the statistical uncertainties in data only.
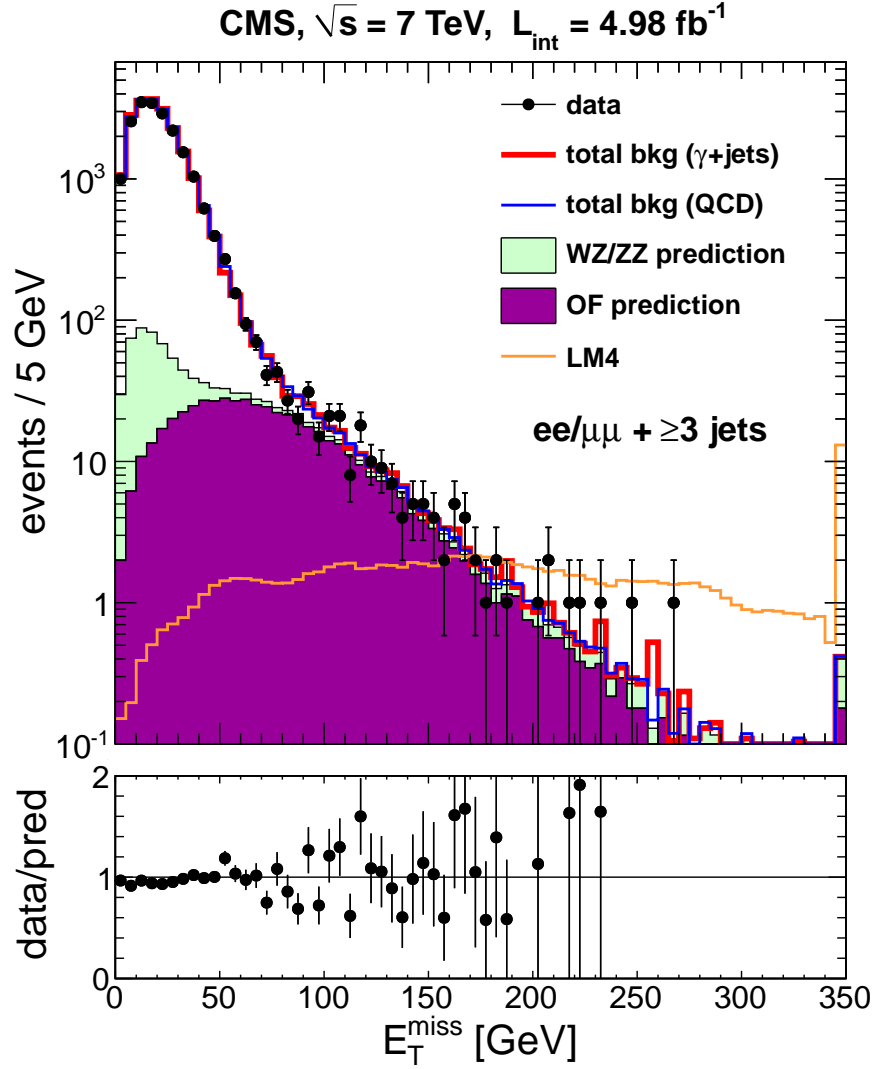
Figure 4.15: The observed *MET* distribution for events with $N_{jets} \geq 3$ for data (black points), predicted OF background from MC normalized to the $e\mu$ yield in data (solid purple histogram), $WZ + ZZ$ background (solid green histogram) and total background including the Z + jets predicted from γ + jets (red line) and QCD (blue line) *MET* templates. The ratio of the observed and total predicted yields (data/pred) is indicated using the average of the γ + jets and QCD methods. The error bars indicate the statistical uncertainties in data only.

Table 4.11: Summary of results in the regions $MET > 30, 60, 100, 200$ and 300 GeV for $N_{jets} \geq 2$. The total predicted background (total bkg) is the sum of the Z + jets background predicted from the γ + jets MET templates method (Zbkg), the flavor-symmetric background predicted from opposite-flavor events (OF bkg), and the WZ+ZZ background predicted from MC (VZ bkg). The uncertainties include both the statistical and systematic contributions. For the observed yield (data), the first (second) number in parentheses is the yield in the ee ($\mu\mu$) final state. The CLs 95% confidence level upper limit on the non-SM yield is indicated. The expected NLO yields for the LM4 and LM8 benchmark SUSY scenarios are indicated, including the uncertainties from lepton identification and isolation efficiency, trigger efficiency, hadronic energy scale, integrated luminosity, and MC statistics. These LM4 and LM8 yields have been corrected for the impact of signal contamination.

	$MET > 30$ GeV	$MET > 60$ GeV	$MET > 100$ GeV
Zbkg	15070 ± 4825	484 ± 156	36 ± 12
OF bkg	1116 ± 101	680 ± 62	227 ± 21
VZ bkg	269 ± 135	84 ± 42	35 ± 17
Total bkg	16455 ± 4828	1249 ± 174	297 ± 30
Data	16483 (8243,8240)	1169 (615,554)	290 (142,148)
Observed UL	9504	300	57
Expected UL	9478	349	60
LM4	120 ± 7.0	108 ± 6.7	93 ± 6.6
LM8	52 ± 3.2	46 ± 3.0	37 ± 2.8

	$MET > 200$ GeV	$MET > 300$ GeV
Zbkg	2.4 ± 0.9	0.4 ± 0.3
OF bkg	11 ± 3.2	1.6 ± 0.6
VZ bkg	5.3 ± 2.7	1.2 ± 0.7
Total bkg	19 ± 4.3	3.2 ± 1.0
Data	14 (8,6)	0
Observed UL	8.3	3.0
Expected UL	11	4.6
LM4	53 ± 7.3	24 ± 6.2
LM8	21 ± 2.8	9.1 ± 2.3

Table 4.12: Summary of results in the regions $MET > 30, 60, 100, 200$ and 300 GeV for $N_{\text{jets}} \geq 3$. The Z + jets and total background predictions are quoted separately for the QCD and γ + jets MET templates. For the total predicted background, the average of the background predictions from the QCD and γ + jets templates methods is used, assessing half the difference between the two methods as an additional systematic uncertainty. Other details are the same as in Tab. 4.11.

	$MET > 30$ GeV	$MET > 60$ GeV	$MET > 100$ GeV
Zbkg (QCD)	4010 ± 802	191 ± 57	11 ± 11
Zbkg (γ + jets)	3906 ± 1252	187 ± 61	14 ± 5.0
OF bkg	442 ± 41	284 ± 26	107 ± 10
VZ bkg	86 ± 43	26 ± 13	11 ± 5.6
Total bkg (QCD)	4539 ± 804	502 ± 64	129 ± 16
Total bkg (γ + jets)	4435 ± 1253	498 ± 67	132 ± 13
Total bkg (average)	4487 ± 1029	500 ± 66	131 ± 15
Data	4501 (2272,2229)	479 (267,212)	137 (73,64)
Observed UL	2028	120	40
Expected UL	2017	134	36
LM4	97 ± 6.1	90 ± 6.1	79 ± 6.6
LM8	42 ± 2.6	39 ± 2.5	33 ± 2.5

	$MET > 200$ GeV	$MET > 300$ GeV
Zbkg (QCD)	0.7 ± 0.7	0.1 ± 0.1
Zbkg (γ + jets)	1.7 ± 0.7	0.3 ± 0.2
OF bkg	7.5 ± 2.2	1.1 ± 0.5
VZ bkg	1.9 ± 1.0	0.4 ± 0.3
Total bkg (QCD)	10 ± 2.5	1.6 ± 0.6
Total bkg (γ + jets)	11 ± 2.5	1.9 ± 0.6
Total bkg (average)	11 ± 2.5	1.8 ± 0.6
Data	8 (3,5)	0
Observed UL	6.7	3.0
Expected UL	8.4	3.9
LM4	44 ± 7.1	19 ± 5.4
LM8	19 ± 2.7	8.3 ± 2.1

Table 4.13: Summary of results in the the exclusive *MET* bins 100-200, 200-300 GeV, and >300 GeV for $N_\text{jets} \geq 2$. The total predicted background (total bkg) is the sum of the Z + jets background predicted from the γ + jets *MET* templates method (Z bkg), the flavor-symmetric background predicted from opposite-flavor events (OF bkg), and the WZ+ZZ background predicted from MC (VZ bkg). The uncertainties include both the statistical and systematic contributions. For the observed yield (data), the first (second) number in parentheses is the yield in the *ee* ($\mu\mu$) final state.

	MET $100-200$ GeV	*MET* $200-300$ GeV	*MET* > 300 GeV
Zbkg	33 ± 12	1.9 ± 0.8	0.4 ± 0.3
OF bkg	215 ± 20	10 ± 3.0	1.6 ± 0.6
VZ bkg	29 ± 15	4.2 ± 2.1	1.2 ± 0.7
Total bkg	278 ± 28	16 ± 3.7	3.2 ± 1.0
Data	276 (134,142)	14 (8,6)	0

Table 4.14: Summary of results in the the exclusive *MET* bins 100-200, 200-300 GeV, and >300 GeV for $N_{\text{jets}} \geq 3$. The total predicted background (total bkg) is the sum of the Z + jets background predicted from the *MET* templates method (Zbkg), the flavor-symmetric background predicted from opposite-flavor events (OF bkg), and the $WZ + ZZ$ background predicted from MC (*VZ* bkg). The Z + jets and total background predictions are quoted separately for the QCD and γ + jets *MET* templates. The uncertainties include both the statistical and systematic contributions. For the average of the background predictions from the QCD and γ + jets templates methods, we assess half the difference between the 2 methods as an additional systematic uncertainty. For the observed yield (data), the first (second) number in parentheses is the yield in the *ee* ($\mu\mu$) final state.

MET	$100 - 200$ GeV	$200 - 300$ GeV	> 300 GeV
Zbkg (QCD)	11 ± 11	0.5 ± 0.5	0.1 ± 0.1
Zbkg (γ + jets)	13 ± 4	1.3 ± 0.6	0.3 ± 0.2
OF bkg	99 ± 10	6.4 ± 1.9	1.1 ± 0.5
VZ bkg	9 ± 4	1.4 ± 0.7	0.4 ± 0.3
Total bkg (QCD)	119 ± 15	8.3 ± 1.3	1.6 ± 0.6
Total bkg (γ + jets)	120 ± 11	9.1 ± 2.1	1.9 ± 0.6
total bkg (average)	120 ± 13	8.7 ± 1.9	1.8 ± 0.6
Data	129 (70,59)	8 (3,5)	0

Table 4.15: Results for run 2011A for $N_{\text{jets}} \geq 2$.

	$MET > 30$ GeV	$MET > 60$ GeV	$MET > 100$ GeV
Z Pred	4902 ± 1570	136 ± 44	10 ± 4
$t\bar{t}$ Pred	523 ± 48	319 ± 30	107 ± 10
diboson Pred	113 ± 57	36 ± 18	15 ± 7
Total Pred	5538 ± 1572	490 ± 56	131 ± 13
Data	5345	447	117

	$MET > 200$ GeV	$MET > 300$ GeV
Z Pred	0.44 ± 0.29	0.03 ± 0.02
$t\bar{t}$ Pred	5.5 ± 1.7	0.94 ± 0.45
diboson Pred	2.2 ± 1.2	0.49 ± 0.35
Total Pred	8.2 ± 2.0	1.5 ± 0.6
Data	8	0

4.5.1 Results for 2011A and 2011B separately

This section shows the results of Sec. 4.5 (Tabs. 4.11 and 4.12), but split between runs 2011A and 2011B. Note that the absolute luminosity corresponding to these two runs does not affect the Z + jets nor the OF ($t\bar{t}$) predictions because those are normalized relative to data events. The diboson prediction is therefore the only prediction affected by absolute luminosity. The luminosity of run 2011A is 2.1 fb^{-1}, and run 2011B is 2.9 fb^{-1}. The results are shown in Tabs. 4.15 through 4.18.

Table 4.16: Results for run 2011B for $N_{\text{jets}} \geq 2$.

	$MET > 30$ GeV	$MET > 60$ GeV	$MET > 100$ GeV
Z Pred	10168 ± 3257	348 ± 113	26 ± 9
$t\bar{t}$ Pred	593 ± 54	361 ± 33	120 ± 12
diboson Pred	156 ± 78	49 ± 24	20 ± 10
Total Pred	10917 ± 3259	758 ± 121	166 ± 18
Data	11138	722	173

	$MET > 200$ GeV	$MET > 300$ GeV
Z Pred	1.9 ± 0.8	0.41 ± 0.24
$t\bar{t}$ Pred	5.9 ± 1.8	0.62 ± 0.35
diboson Pred	3.1 ± 1.6	0.67 ± 0.49
Total Pred	11.0 ± 2.5	1.7 ± 0.7
Data	6	0

Table 4.17: Results for run 2011A for $N_{\text{jets}} \geq 3$.

	$MET > 30$ GeV	$MET > 60$ GeV	$MET > 100$ GeV
Z Pred	1349 ± 432	55 ± 18	5.3 ± 1.9
$t\bar{t}$ Pred	203 ± 19	130 ± 12	50 ± 5.3
diboson Pred	36 ± 18	11 ± 5.5	4.7 ± 2.4
Total Pred	1588 ± 433	196 ± 23	60 ± 6.1
Data	1521	193	58

	$MET > 200$ GeV	$MET > 300$ GeV
Z Pred	0.37 ± 0.27	0.03 ± 0.02
$t\bar{t}$ Pred	3.3 ± 1.1	0.63 ± 0.35
diboson Pred	0.81 ± 0.42	0.19 ± 0.13
Total Pred	4.5 ± 1.2	0.85 ± 0.37
Data	4	0

Table 4.18: Results for run 2011B for $N_{\text{jets}} \geq 3$.

	$MET > 30$ GeV	$MET > 60$ GeV	$MET > 100$ GeV
Z Pred	2558 ± 820	132 ± 43	9.0 ± 3.1
$t\bar{t}$ Pred	239 ± 22	155 ± 15	56 ± 5.9
diboson Pred	50 ± 25	15 ± 7.6	6.5 ± 3.2
Total Pred	2846 ± 821	302 ± 46	72 ± 7.4
Data	2980	286	79

	$MET > 200$ GeV	$MET > 300$ GeV
Z Pred	1.3 ± 0.6	0.31 ± 0.22
$t\bar{t}$ Pred	4.2 ± 1.3	0.47 ± 0.30
diboson Pred	1.1 ± 0.6	0.26 ± 0.18
Total Pred	6.6 ± 1.6	1.0 ± 0.4
Data	4	0

4.6 Interpretation of Experimental Results

The previous sections detail the experimental techniques and results of this analysis. There remains significant work to be done to make these results useful for placing limits on theories of new physics. Particle Physics theory has advanced far beyond experiment in the sense that there are a plethora of possible new physics scenarios. It is not trivial to check whether new experimental results can limit the parameter space of such new physics models. For the majority of this work to fall on the experimentalists is not practical–the time of experimentalists is better spent understanding experiments than on placing limits on new (realistic or unrealistic) theories.

The reason for this is simply the vastness of the possible parameter space of new physics models. For example, the minimal model of supersymmetry has around 100 parameters [26]. The phenomenology of such supersymmetric models may depend non-trivially on every parameter. There are many other entire classes of new physics scenarios (extra dimensions, technicolor, etc). In order to set a rigorous limit on any such model, MC must be generated for a particular choice of parameters. This entails both generating the underlying collisions (many generator tools are available, but they are not necessarily general enough to cover every scenario) and then passing the generated events to a full detector simulation of the CMS detector. (The CMS collaboration does not make its detector simulation public.)

The best compromise currently in practice are a set of two tools: efficiency models and simplified models. In the case of efficiency models, the goal is for a theorist to be able to create a set of generator-level events and then apply the efficiency models directly to those events (after fiducial cuts) to estimate the yield which would be seen by CMS (in a given luminosity). This yield can then be compared to the upper limits (UL) of Sec. 4.5 to see whether the given model is ruled out.

However, there are two full models that we calculate cross section upper limits for: LM4 and LM8. These are discussed in Sec. 4.6.1. Efficiency models are described in Sec. 4.6.2, and simplified models are described in Sec. 4.7.

4.6.1 Cross Section Upper Limits on LM4 and LM8

Although the CMSSM [43] is one of the most popular models of SUSY, it has a very low branching ratio to Z bosons except for a very limited range of parameter space. However, there are two benchmark points in the CMSSM parameter space, called LM4 and LM8 ("LM" stands for "low mass" [44]), which do have an appreciable branching ratio to Z bosons. Therefore, the only two full models considered in this analysis are LM4 and LM8. For placing limits on specific models, it is preferable to use cross section upper limits rather than the model independent upper limits reported in Sec. 4.5. This is because the efficiencies are model dependent, so they should be calculated separately for each specific model under consideration. For model independent upper limits, the efficiency is assumed to be 100% with zero uncertainty. We use the procedure outlined in Sec. 4.7.1 for the signal efficiency uncertainties.

For the limits in this section, signal contamination (see Sec. 4.2.7) is taken into account by finding the yield for the given model in the $e\mu$ channel with no dilepton invariant mass cut, and then multiplying by $K = 0.16$. This yield is then subtracted from the same flavor yield. The results for the signal regions of $MET > 100$, 200, and 300 GeV in the $N_{\text{jets}} \geq 3$ bin are used to calculate the upper limits summarized in Tab. 4.19. This table shows that both of these models are ruled out by this analysis.

Table 4.19: Summary of the 95% CLs exclusion limits on the cross section for the LM4 and LM8 models using the cut-and-count method in the 3 signal regions MET > 100, 200 and 300 GeV for $N_{\text{jets}} \geq 3$. Uncertainties from luminosity, trigger efficiency, lepton selection efficiency and hadronic energy scale are included. The limits are corrected for the impact of signal contamination in the OF background prediction. For reference, we display also the NLO cross sections for the two models.

SUSY benchmark	MET > 100 GeV	MET > 200 GeV	MET > 300 GeV	σ_{NLO} (pb)
LM4	1.4	0.44	0.42	2.5
LM8	1.4	0.42	0.38	1.0

4.6.2 Efficiency Models: Overview

Efficiency refers to the probability for the (CMS) detector to reconstruct an object or particle. Efficiencies are normally expressed as a set of numerator and denominator requirements. The ratio of the number of events passing the numerator requirements to that passing the denominator requirements for some dataset is the efficiency. The difficult part of calculating efficiencies is usually wrapped up in either the numerator or denominator definitions. In this case the numerator is relatively straightforward: it is some part of the final selection requirements described in Sec. 4.1. The denominators for efficiency models are one or more generator-level particles inside the acceptance used for this analysis.

Efficiencies are thus provided allowing one to calculate the fraction of generator-level events likely to pass the final analysis selections. These efficiencies must be calculated in the context of a particular model, and are assumed to be independent of one another. This is in fact the main weakness of the efficiency models–the efficiencies are not independent so changing some parts of a model may change some efficiences in non-trivial ways. Nevertheless, it is usually a decent approximation to treat the efficiencies as independent, so that is what we do. It is in principle possible to to compute two-dimensional efficiencies. For example, to parameterize the lepton isolation efficiency as a function of the lepton p_T and N_{jets}. This is not yet done, and remains as a possible further refinement if need should arise in the future.

We will normally define the denominator as one or more generator particles. For example, when parameterizing lepton identification efficiency, the denominator is simply a generator lepton in the acceptance. For MET, the transverse component of the sum of all undetected particles is considered the generator-level MET. Undetected particles here means neutrinos and the LSP.

4.6.3 Efficiency Models: Leptons

In order for a dilepton event to be recorded by CMS, it must pass one or more single or di-lepton triggers. The efficiency for these triggers can be well approximated by constants: the efficiency to trigger on a $\mu\mu$ event is 90%, an $e\mu$ event is 95%, and an

ee event is 100%. The systematic uncertainties (see Sec. 4.7.1) on these efficiencies are 2% each.

In general, the lepton identification and isolation requirements are fairly independent of one another, so we treat them as such for the purpose of efficiency models. The identification efficiency for muons is approximately independent of p_T, and about 91%. For electrons, it varies approximately linearly from 83% at $p_T = 20$ GeV to 93% at $p_T = 60$ GeV and is then flat. More details on how these numbers were arrived at, plus combined identification and isolation efficiencies for $t\bar{t}$ are shown in Fig. 4.16.

The isolation requirement is a very model dependent quantity as it depends strongly on the amount of hadronic activity, ie., N_{jets} and H_T. We use $t\bar{t}$ to parameterize the isolation requirement because it is a process with large H_T (at least for a standard model process) and because it is a very common background. In addition, the isolation efficiency is also given for LM4 and LM8 as examples of how the isolation efficiency degrades with increased jet activity. These are found in Fig. 4.17, and fit to Eq. 4.1 of Sec. 4.6.4. The results of the fit are summarized in Tab. 4.20. To summarize the conclusions from these figures, the isolation efficiency in $t\bar{t}$ events varies approximately linearly from about 85% for muons and 88% for electrons at $p_T = 20$ GeV to about 97% for $p_T > 60$ GeV. For LM4, this efficiency is degraded by about 5% over the whole momentum spectrum, and for LM8, it is degraded by about 10%.

Table 4.20: Values of the fitted parameters (see Eq. 4.1) for the lepton isolation efficiency vs p_T shown in Fig. 4.17.

Variable, Sample	$\varepsilon_{\text{plateau}}$	x_{offset} (GeV)	σ (GeV)
Electron p_T, $t\bar{t}$	0.97	-37	65
Electron p_T, LM4	0.95	-80	128
Electron p_T, LM8	0.88	-37	77
Muon p_T, $t\bar{t}$	0.97	-24	57
Muon p_T, LM4	0.95	-39	94
Muon p_T, LM8	0.91	-46	114
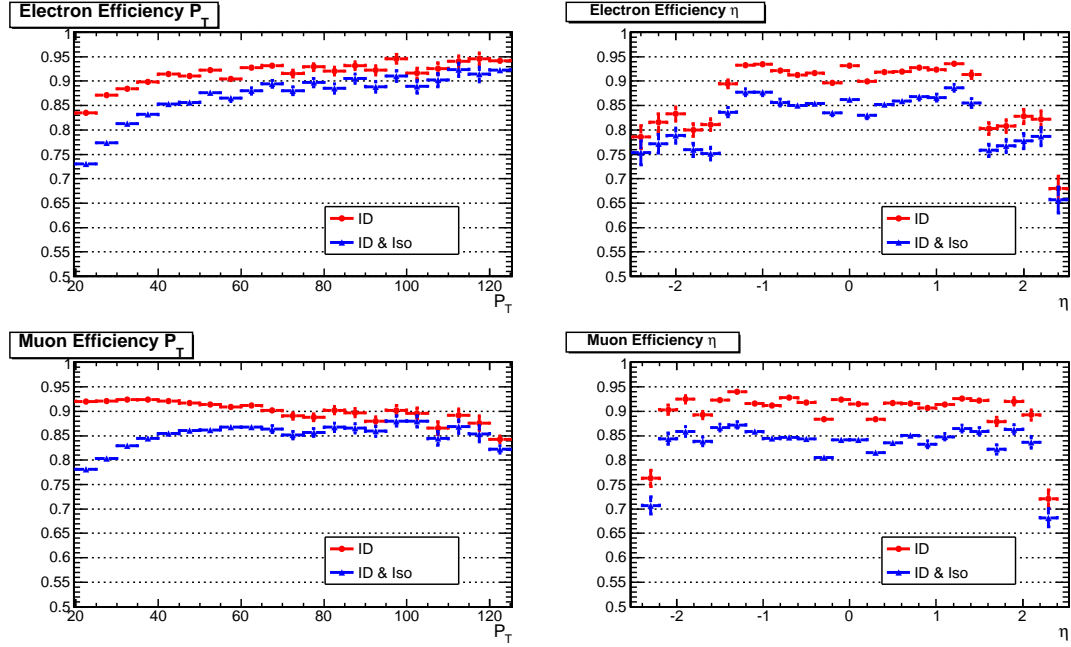
Figure 4.16: Identification and isolation efficiencies for electrons (top) and muons (bottom) from $t \to W \to \ell$ and $t \to W \to \tau \to \ell$ in $t\bar{t}$ events as a funciton of lepton p_T (left) and η (right).

4.6.4 Efficiency Models: *MET* and Jets

We parameterize the *MET* turn on by fitting to this function:

$$\varepsilon(x) = \varepsilon_{\text{plateau}} \frac{1}{2}\left[\text{erf}\left(\frac{x - x_{\text{offset}}}{\sigma}\right) + 1\right] \tag{4.1}$$

Recall the definition of the error function:

$$\text{erf}(x) = \frac{2}{\sqrt{\pi}} \int_0^x e^{-t^2} dt \tag{4.2}$$

Figure 4.18 contains MET turn-on curves for LM4 which are fitted to Eq. 4.1. The values of the fitted parameters are quoted in Tab. 4.21.

For this analysis, we do not parameterize the jet requirements in any quantitative way because the jet requirements are very modest. We consider generator level quarks and gluons with $p_T > 30$ GeV and $|\eta| < 3.0$ as an approximation to jets. For a more complete treatment of hadronic requirements, see Sec. 5.4.
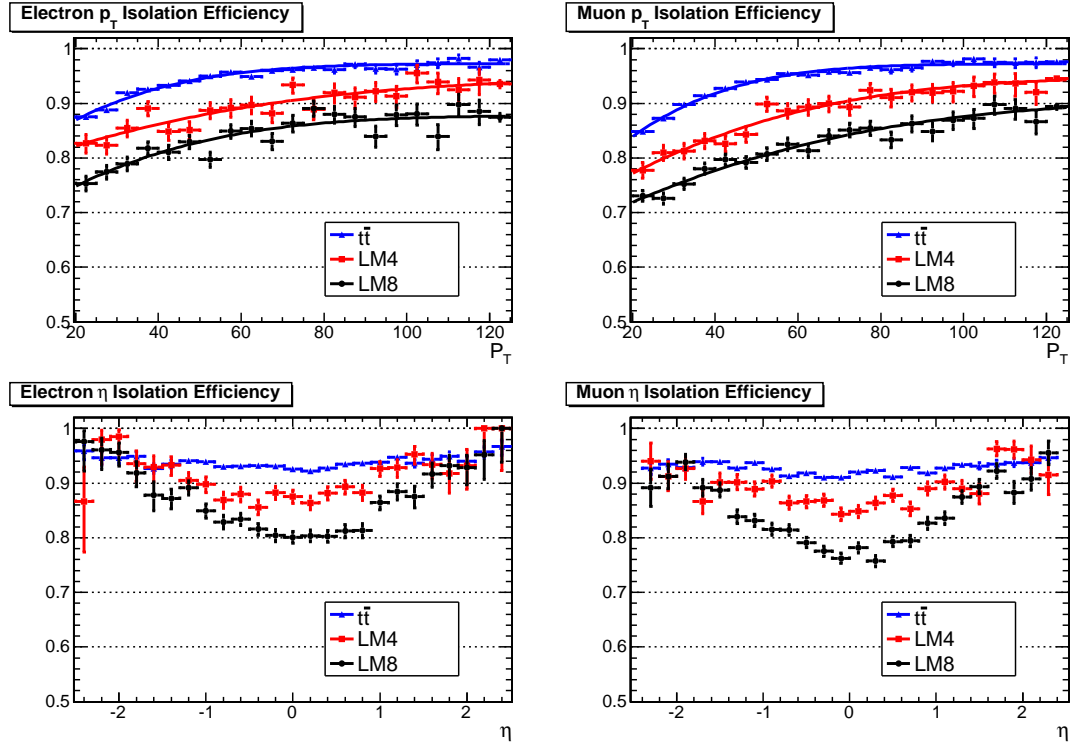
Figure 4.17: Isolation efficiencies for electrons (left) and muons (right) for $t\bar{t}$, LM4 and LM8 as a funciton of lepton p_T (top) and η (bottom). Efficiencies as a function of p_T are fit to Eq. 4.1, and fit parameters are given in Tab. 4.20.

As a validation of the efficiency models provided, we have compared the yields expected from applying the efficiency model to LM4 and LM8 to the full detector simulation for these model points. We find closure to within about 15%.

Table 4.21: Values of the fitted parameters (see Eq. 4.1) for the MET turn-on curves of Fig. 4.18.

Parameter	$MET > 100$ GeV	$MET > 200$ GeV	$MET > 300$ GeV
$\varepsilon_{\text{plateau}}$	1.00	0.99	0.98
x_{offset} (GeV)	103	214	321
σ (GeV)	29	38	40
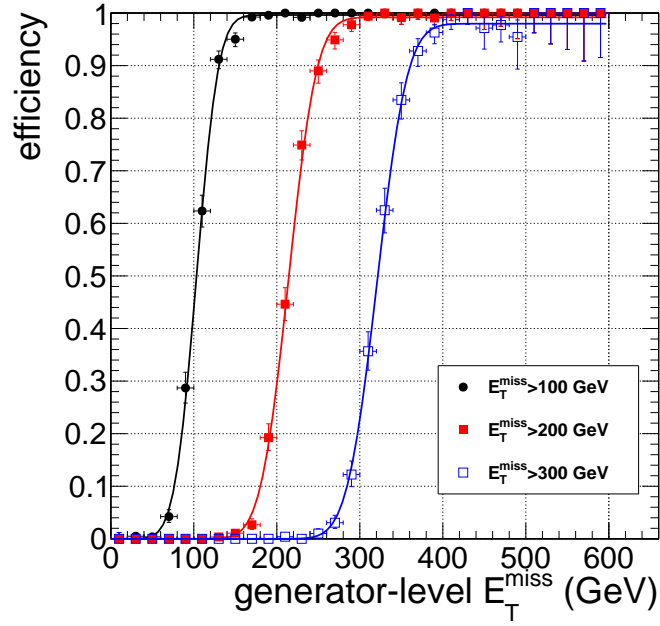
Figure 4.18: The efficiency to pass the $MET > 100, 200, 300$ GeV requirements as a function of the generator-level MET for LM4.

4.7   Simplified Models

The basic idea behind simplified models [45, 46, 47] is to approximate a particular new physics scenario as a single decay diagram. A full model will have a spectrum of particles, each with a set of branching ratios, producing a potentially complicated phenomenology. However, it is often the case that the production of such a model will be dominated by the production of one or just a few particles. Those particles may have multiple decay modes, but often a particular analysis is only sensitive to only one or a few of those modes. Therefore, using a simplified model with just a single diagram can be representative of a more complete model. Efficiencies are provided as a function of the simplifed model's parameters allowing a theorist to validate his or her own approximation to the CMS reconstruction efficiency. These efficiencies can then be applied to other models provided they are similar to the simplifed model. In certain cases, such as branching ratios, it may be possible to apply multiplicative factors to the efficiencies provided here. Cross section upper limits are also provided for the simplified models, again mainly for validation purposes.

The simplifed models in consideration here have only two parameters each which are always the masses of two of the particles in the decay chain. Parameterizing models in terms of new particle masses gives a simple interpretation for the mass reach of an analysis.

In addition to the uncertainties on the background estimates discussed in Sec. 4.2 and 4.3, for application of the experimental results to a new physics model, additional uncertainties on the signal acceptance and efficiency must be taken into account. These are discussed in Sec. 4.7.1. We then move on to specific simplified models. Simplified models with a massive LSP are considered in Sec. 4.7.2, and massless LSPs are studied in Sec. 4.7.3.

4.7.1   Signal Acceptance and Efficiency Uncertainties

In order to place a realistic limit on a new physics model, systematic uncertainties on the yield of the model must be taken into account. These are distinct from and in addition to the systematic uncertainties on the background estimates discussed above.

The first source of this uncertainty is associated with leptons, and has two parts. The first part is due to the lepton trigger requirements. This is a 2% uncertainty based on studies of trigger efficiency in a leptonic Z sample. There is also systematic uncertainty due to the lepton identification and isolation requirements. The efficiency to pass these requirements is found to agree between data and MC to about 2%, so we take this as the corresponding systematic. Note that this is 2% per lepton, and since there is a correlation between the two leptons, this is an overall 4% systematic.

The other major source of systematic uncertainty is associated with the jet and *MET* energy scale. The two scales are associated with one another because systematic under or overmeasurement of jets can contribute to *MET*. The energies of jets, for the purposes of this analysis, are known to at least 7.5% [36]. We therefore vary the jet momenta up and down by this fraction, and propagate the change in momentum balance to the *MET*. After doing so, the yield for a given signal region is checked and compared to the nominal yield to derive a systematic uncertainty. These uncertainties will be smaller for models with large *MET*, or larger for models with modest *MET*. For LM4 and LM8, the uncertainty for the *MET* > 100 GeV requirement is 4-6%, but for *MET* > 300 GeV, the uncertainty is around 24-28%. For the simplifed models considered in the following sections, this source of uncertainty is evaluated at each parameter point and used in the calculation of the cross section upper limit.

Uncertainties in the acceptance due to variations in the parton distribution functions are evaluated individually for each model as recommended in [48]. The uncertainty from the integrated luminosity is 2.2% [49].

4.7.2   Simplified Models with Massive LSP

The simplifed models considered in this section are inspired by a SUSY scenario similar to the CMSSM model points LM4 and LM8. The simplified model features pair production of a heavy gluino ($\tilde{g}$) which decays via an offshell squark to two quarks and a neutralino ($\tilde{\chi}_2^0$). For these models, the squark mass is always much larger than the gluino mass, so squark production is negligible. The $\tilde{\chi}_2^0$ then decays to a Z and a $\tilde{\chi}_1^0$ which is the LSP. Becuase the gluino is pair produced, and because all of the branching ratios are fixed to unity, there are two Zs and two LSPs in each event. This topology is

illustrated in Fig. 4.19. In CMS terminology, this model is referred to as T5zz.

The simplifed model has two parameters: the mass of the gluino ($m_{\tilde{g}}$) and the mass of the LSP ($m_{\tilde{\chi}_1^0}$). The efficiencies and cross section upper limits are given as a function of these two parameters. Because the Z mass is nearly 100 Gev (91.2 GeV), the mass difference between the gluino and LSP is always at least 100 GeV so that the Z can be on shell. This analysis does not have sensitivity to offshell Zs due to the dilepton mass requirement. There is in effect a third parameter of the model which is the mass of the intermediate neutralino ($m_{\tilde{\chi}_2^0}$). $m_{\tilde{\chi}_2^0}$ is parameterized in terms of $m_{\tilde{g}}$ and $m_{\tilde{\chi}_1^0}$: $m_{\chi_2^0} = m_{\chi_1^0} + x \cdot (m_{\tilde{g}} - m_{\chi_1^0})$. x is therefore the ratio of the mass difference between the $\tilde{\chi}_2^0$ and the $\tilde{\chi}_1^0$ to the mass difference between the $\tilde{g}$ and the $\tilde{\chi}_1^0$. We consider three values of the parameter x: $x = 0.25$, $x = 0.5$, and $x = 0.75$. For $x = 0.75$, the $\tilde{\chi}_2^0$ is closer in mass to the gluino than the LSP. This is a trade off between giving more energy to the jets versus to the *MET*.

The efficiencies provided for the simplified models correspond to the signal region of *MET* > 100 GeV and are normalized to at least one (of the two) Zs decaying leptonically. For each parameter point specified by the masses of the $\tilde{g}$ and $\tilde{\chi}_1^0$, we calculate the upper limits on the cross-section using the results of the three non-overlapping regions *MET* 100-200 GeV, 200-300 GeV, and > 300 GeV displayed in Tab. 4.13 ($N_{\text{jets}} \geq 2$).

The inputs to the shape analysis are the observed, predicted, and expected signal yields in the 3 non-overlapping regions. The luminosity, trigger effiency, and lepton selection efficiency uncertainties are assessed as flat uncertainties. The hadronic energy scale uncertainty is assessed as a shape systematic, taking into account the bin-to-bin migration of signal events. We do not correct for signal contamination since the signal contributions to the QCD and γ + jets control samples and to the $e\mu$ control sample are negligible. The cross section plots are computed with respect to the inclusive Z decay mode. In order to interpret these limits in terms of gluino pair production cross-section, we use a reference cross-section σ_{ref} and draw the 95% CL exclusion contours at 1/3, 1 and 3 times σ_{ref} in order to give a sense of how the limit changes with the cross-section. The cross section σ_{ref} corresponds to gluino pair production in the limit of infinitely heavy squarks, calculated at next to leading order using PROSPINO [50] and CTEQ6

parton distribution functions [51].

The results of the above procedure for $x = 0.5$ are displayed in Fig. 4.20, for $x = 0.75$ in Fig. 4.21, and for $x = 0.25$ in Fig. 4.22.
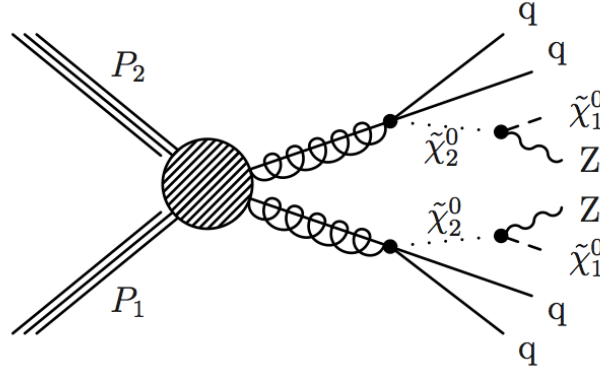
Figure 4.19: Diagramatic illustration of the production and decay of the massive LSP simplified model scenario (T5zz).
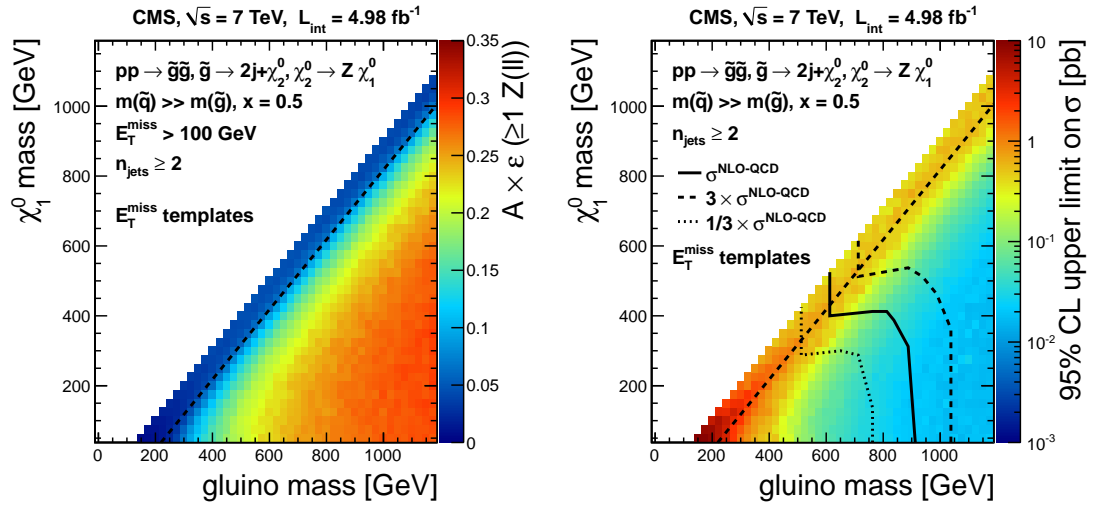
Figure 4.20: Results for the SMS model with neutralino LSP and $x = 0.5$ for $N_{\text{jets}} \geq 2$. The left plot is the efficiency times acceptance with respect to the number of signal events with at least one leptonically decaying Z. The right plot is the cross section upper limit, calculated with respect to the inclusive Z decay mode.
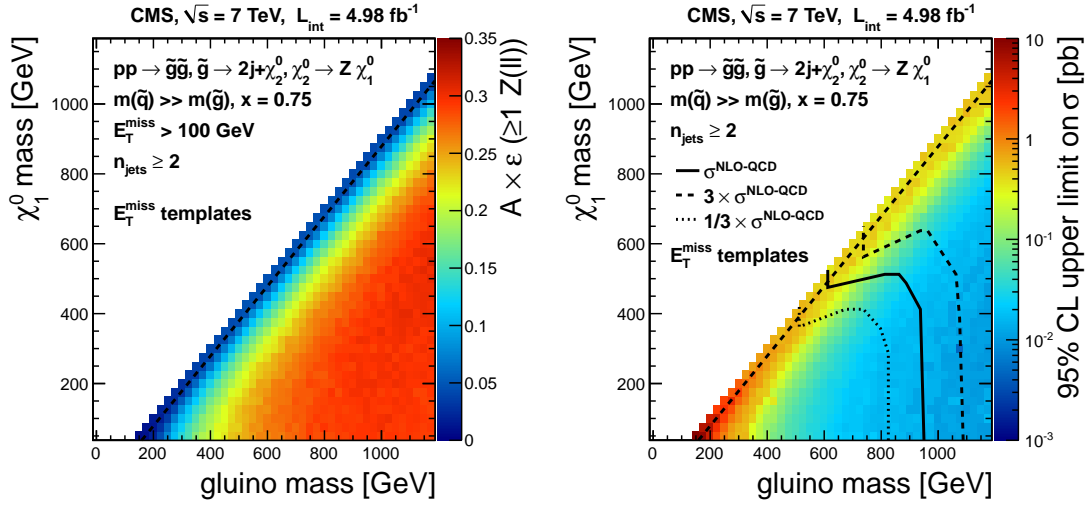
Figure 4.21: Results for the SMS model with neutralino LSP and $x = 0.75$ for N_{jets} ≥ 2. The left plot is the efficiency times acceptance with respect to the number of signal events with at least 1 leptonically decaying Z. The right plot is the cross section upper limit, calculated with respect to the inclusive Z decay mode.
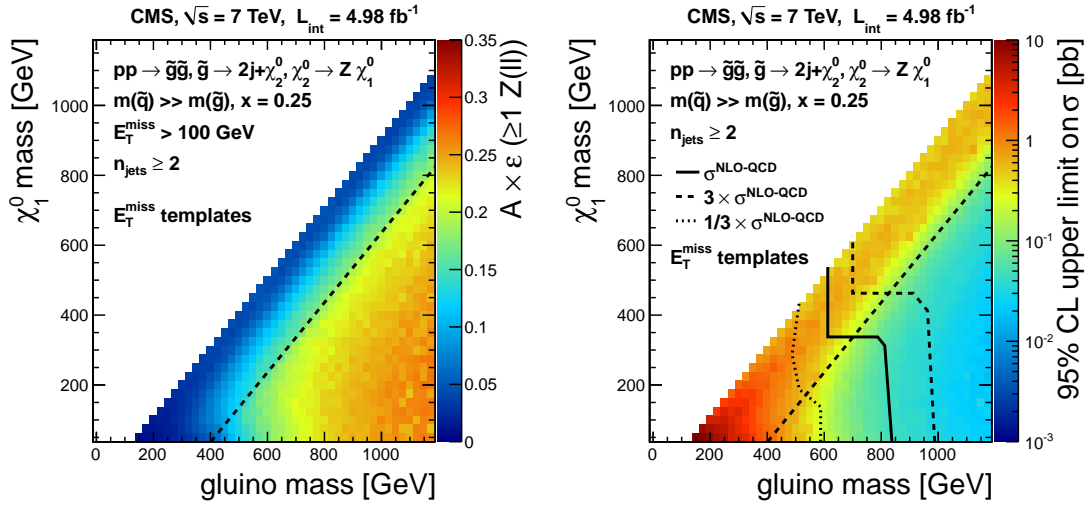
Figure 4.22: Results for the SMS model with neutralino LSP and $x = 0.25$ for N_{jets} ≥ 2. The left plot is the efficiency times acceptance with respect to the number of signal events with at least one leptonically decaying Z. The right plot is the cross section upper limit, calculated with respect to the inclusive Z decay mode.

4.7.3   Simplified Models with Massless LSP

The massless LSP scenario is inspired by gauge-mediated SUSY breaking (GMSB) models. In these models, the LSP is the gravitino ($\tilde{G}$), and typically has a very small mass of $\lesssim 1$ keV. Here we treat the gravitino as massless. The topology of this model is essentially identical to the topology of the T5zz model of Sec. 4.7.2 except with the LSP changed from the $\tilde{\chi}_1^0$ to the $\tilde{G}$. (Please refer to Sec. 2.2.1 for a discussion of the gauge structure of SUSY.) See Fig. 4.23. Because the LSP is massless, the two parameters of the model are the gluino mass ($m_{\tilde{g}}$) and the neutralino mass ($m_{\tilde{\chi}_1^0}$).

Our approach for calculating efficiencies and cross section upper limits is the same here as in Sec. 4.7.2. The results are shown in Fig. 4.24. The same results are redisplayed after projecting onto the $m_{\tilde{g}}$ axis in Fig. 4.25.
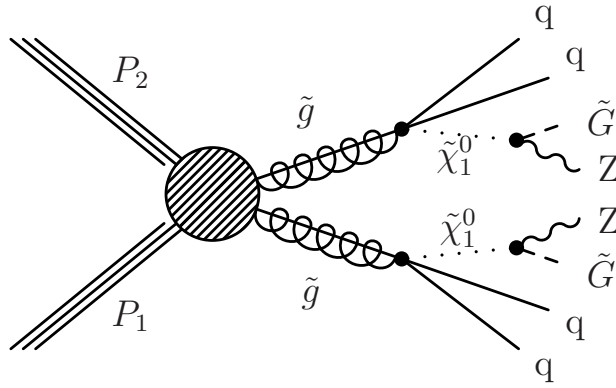
Figure 4.23: Diagramatic illustration of the production and decay of the massless LSP simplified model scenario.
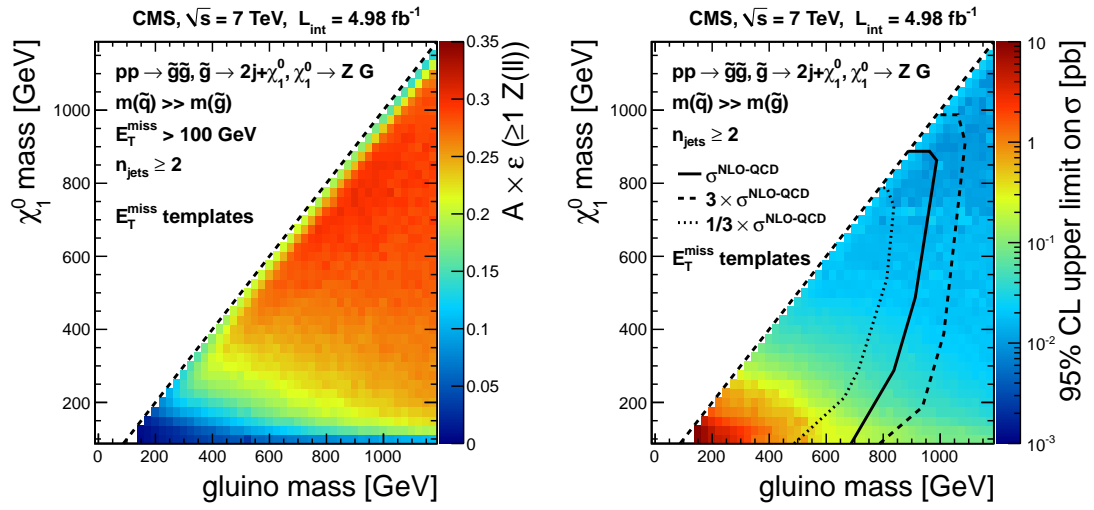
Figure 4.24: Results for the SMS model with massless LSP ($\tilde{G}$) for $N_{\text{jets}} \geq 2$. The left plot is the efficiency times acceptance with respect to the number of signal events with at least one leptonically decaying Z. The right plot is the cross section upper limit, calculated with respect to the inclusive Z decay mode.
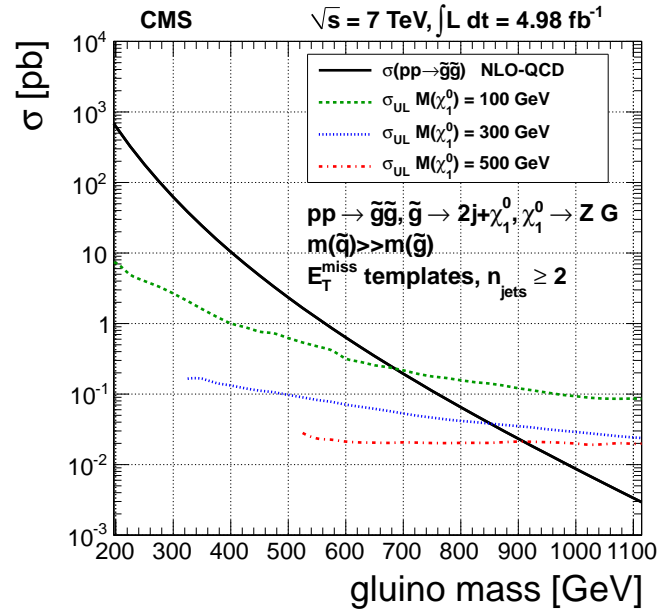
Figure 4.25: Results for the SMS model with massless LSP ($\tilde{G}$) for $N_{\text{jets}} \geq 2$. The upper limits on the cross section vs. gluino mass are plotted for three choices for the mass of the lightest neutralino, and compared to the predicted cross section computed at NLO.

Selected figures and tables from this chapter are published in: CMS Collaboration, "Search for physics beyond the standard model in events with a Z boson, jets, and missing transverse energy in pp collisions at sqrt s = 7 TeV", Physics Letters B 716 (2012), no. 2, 260 - 284. doi:10.1016/j.physletb.2012.08.026.

Chapter 5

A Search for New Physics in WZ/ZZ + *MET*

This chapter presents an extension of the analysis described in Chapter 4. The overall analysis strategy is practically identical: the background estimation procedures are largely unchanged, and the approach for the interpretation is also analogous to the one previously described. The main difference between the two analyses is the introduction of additional selection criteria (commonly referred to as 'cuts') to gain sensitivity to possible new physics scenarios which could be missed by the analysis previously described. The analysis of Chapter 4 will be referred to as the 'inclusive' analysis to reflect its general nature. The analysis presented in this chapter is called the 'targeted' or 'electroweakino' analysis for reasons which will soon become clear.

The inclusive analysis focused on strong production (ie., QCD) of new physics because that is the scenario with the largest cross section, and hence the one which would potentially be detectable with lower integrated luminosity than other production modes. Schematics of such production diagrams are illustrated in the diagrams in Figs. 4.19 and 4.23. However, many models of new physics, including supersymmetry, also feature electroweak production of new particles. Electroweak production will have a much lower production cross section simply because electroweak coupling is much weaker than strong coupling. (It is, after all, called the 'weak' force.) Also with electroweak production, jets need not appear in the final state. Electroweak production of new physics would likely proceed through diagrams analogous to the ones describing

standard model diboson production (see Fig. 4.2).

Because we are targeting a new physics scenario with a low cross section, it is essential that we reduce the backgrounds beyond what has been presented. This is the main motivation for introducing a new set of cuts.

This chapter is organized as follows. First, I will describe the additional selection criteria which constitute the main difference between the targeted search presented in this chapter and the inclusive search of Chapter 4. Next, I will describe the minimal changes to the background prediction techniques in Sec. 5.2. Finally, the experimental results (Sec. 5.3) and interpretation (Sec. 5.4-5.6) will close the chapter.

5.1 Additional Selection Criteria for WZ/ZZ + MET

Chapter 4 presented the most general possible search in the final state of Z + jets + MET possible with the background prediction methods described. Here, we apply the same approach of the 'inclusive' analysis of Chapter 4, but we add new cuts in order to gain sensitivity to electroweak production of new physics. Specifically, we are targeting the final state of WZ or ZZ plus MET.

In WZ/ZZ, we select at least one leptonically decaying Z boson, exactly as was done in Chapter 4. The other boson (either a W or Z) is selected by its decay to jets. The branching ratio of the Z to jets is about 70%, and the W is about 68% [32].

The main goal of introducing the cuts described in this section is to significantly reduce the background relative to the inclusive analysis. The main background to reduce is $t\bar{t}$ because its rate is so large. As can be clearly seen from Tabs. 4.11 and 4.12, $t\bar{t}$ is the dominant background in the inclusive analysis for all signal regions with $MET > 60$ GeV. Fortunately, there is a relatively straightforward way to reduce the $t\bar{t}$ background without significantly affecting sensitivity to new physics (without b quarks in the final state). The key to doing this is utilizing b tagging, as described in Sec. 5.1.1.

In order to select jets which originate from the decay of W or Z bosons, we require the dijet invariant mass to be near the W and Z masses. This cut also significantly reduces the Z + jets and $t\bar{t}$ backgrounds. See Sec. 5.1.2. The final additional cut is the veto on the presenece of a third lepton in order to reduce the WZ background as

summarized in Sec. 5.1.3.

5.1.1   b Tag Veto

The basic idea of b tagging is to use the long lifetime of b mesons and baryons to distinguish jets with such hadrons from jets with only light quark baryons. The typical lifetime associated with b hadron is 10^{-12} seconds. In contrast, the W and Z bosons live on the order of 10^{-25} seconds, while the charged pion has a lifetime long enough to reach the calorimeters: 10^{-8} s. Because of the long lifetime, the decay products of the b hadrons produce tracks which originate from vertices outside the primary vertex. Detecting such displaced vertices is a main part of b tagging.

Because all top quarks decay to a W boson and a b quark, $t\bar{t}$ events are guaranteed to have two b jets (resulting from the hadronization of the b quark from the top decay), and the likelihood for those jets to fall in the acceptance is fairly high. However, b tagging is a tricky buisness, and the efficiency to correctly tag a true b jet is modest: in the neighborhood of 50-70% depending on the details of the jet and the tagger [52]. Nevertheless, this is plenty good enough for the purposes of this analysis.

The way b tagging is utilized for this analysis is as a b veto. That is, any event which has any jets (passing the p_T and η cuts for N_{jets} counting) which are b tagged is not used for the analysis. Because there are two b jets in every $t\bar{t}$ event, even though the single b jet tagging efficiency is not very high, the probability to correctly tag at least one of the two b jets is high enough to significantly reduce this background.

There are many b tagging algorithms currently in use by CMS. The one we choose to use here is called the track counting high efficiency (TCHE) algorithm. This algorithm has three working points which are characterized by a trade off between efficiency and mis-tag rate. Mis-tag rate is the rate to mistakenly tag a light jet (a jet arising from u, d, or an s quark, or from a gluon) as a b jet. The loose working point has a high efficiency (efficiency refers to the probability to correctly tag a true b jet as such), but also a high mistag rate. The tight working point has a much lower efficiency, but also a low mistag rate. The medium working point is a trade off between the two, maintaining decent efficiency with a reasonable mis-tag rate.

For the purposes of this anslysis, we want to stay on the loose side because

we want to reject as many true b jets as possible in order to effectively reduce the $t\bar{t}$ background. However, a high mis-tag rate is undesirable because it will reject signal by incorrectly tagging light jets as b jets. For the TCHE tagger, the mis-tag rate for the loose working point grows rapidly with the p_T of the jet. The medium working point, however, has a reasonable mis-tag rate even at high jet p_T. For this reason, we use the loose working point for jet $p_T < 100$ GeV, and then use the medium working point for $p_T > 100$ GeV.

5.1.2   Dijet Invariant Mass

This analysis selects WZ and ZZ events by selecting a Z in the dilepton (e or μ) channel, and a W or Z in the dijet channel. In order to select the hadronically decaying boson, the dijet invariant mass is used. Fig. 5.1 shows the dijet mass distribution in MC for WZ, ZZ, Z + jets, and $t\bar{t}$. This plot is made after selecting the two leptons from the Z decay, and after a two jet requirement. In events with three or more jets, the mass of the two leading p_T jets is used. Though the dijet mass resolution is not all that great, there are still very clear peaks in the WZ and ZZ sample from the boson decay. The tails of the distribution for these samples are from ISR jets which happen to have larger p_T than the jets from the W or Z decay.

The choice of the window for this cut is a trade off between rejecting more background from Z + jets and $t\bar{t}$, and maintaining good efficiency for jets from W or Z decays. We find that the optimal place for this cut (at least with cut values of multiples of five) is from 70 to 110 GeV.

There is an alternative to using the two leading jets for the dijet mass requirement, and that is to use the two jets whose mass is closer to the boson the jets came from. Since we are looking for both W and Z to jets, we would use the average of the two masses, or around 85 GeV. However, the problem with doing the cut in this way is that it is much less effective in rejecting Z + jets and $t\bar{t}$ background. In addition, the efficiency for Ws and Zs does not increase very much. We therefore use the two highest p_T jets when making this cut.

In addition to the background rejection described above, this cut also helps reject diboson background where both bosons decay leptonically (or the Z decays to two neu-

trinos) and the jets are from ISR. In this case, the dijet mass distribution is very broad, similiar to the Z + jets distribution of Fig. 5.1.
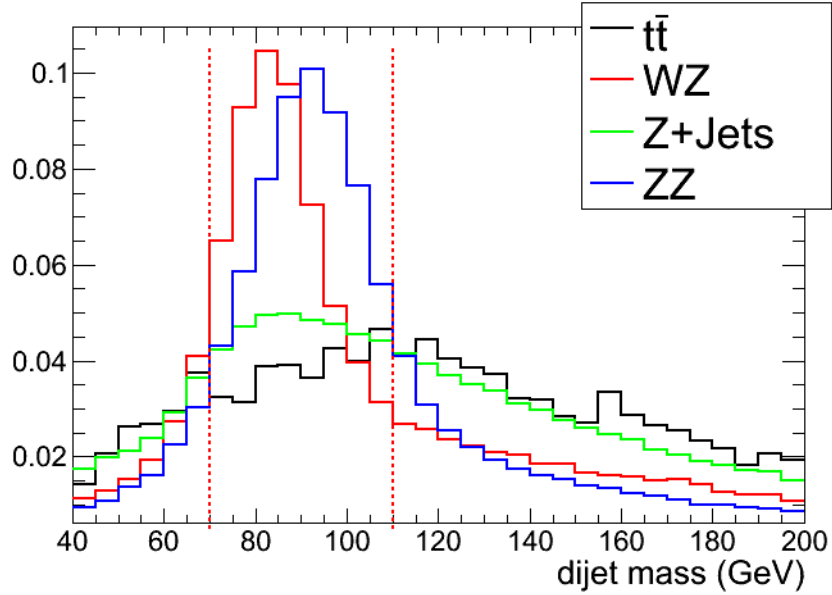
Figure 5.1: The dijet invariant mass distribution in MC overlaid for the most important background processes. The red vertical lines indicate the selection window of 70 to 110 GeV.

5.1.3   Third Lepton Veto

The third lepton veto is used to suppress WZ where both the W and Z decay leptonically and the jets are from ISR. We use the same lepton selection as for signal leptons (see Sec. 4.1.2). After the suppression of $t\bar{t}$ from the additional cuts described above, diboson processes are a large fraction of the remaining background at high *MET*. This cut helps reduce the WZ component of the diboson background.

5.1.4   Preselection

The combination of selection cuts from the nominal analysis (Sec. 4.1.4) and the cuts described above (Secs. 5.1.1 through 5.1.3) constitute the preselection for this targeted analysis. The full list is summarized here:

- A leptonically decaying Z boson: $Z \rightarrow ee$ or $\mu\mu$

- Two or more jets ($p_T > 30$ GeV, $|\eta| < 3.0$)

- A veto on the presence of a b tagged jet

- The invariant mass of the two leading p_T jets is 70 to 110 GeV

- There are exactly two leptons

The yields for the preselection are shown in Tab. 5.1 and the dilepton invariant mass plots are shown in Fig. 5.2. These can be compared to the equivalents for the nominal analysis in Sec. 4.1.4.
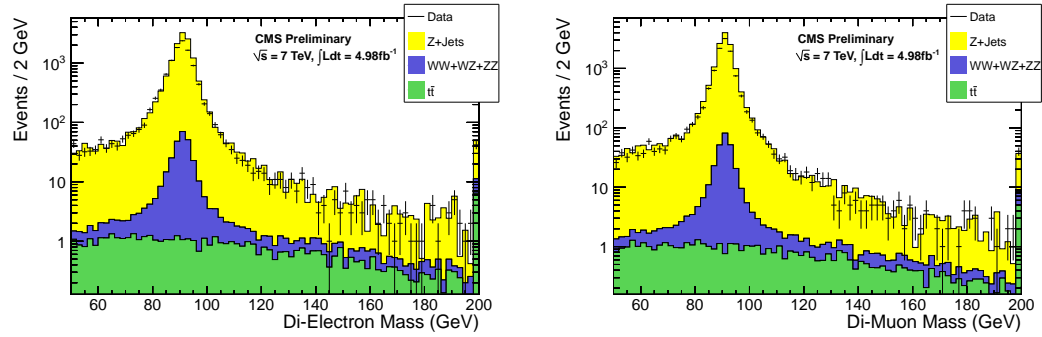
Figure 5.2: Dilepton mass distribution for events passing the preselection for the targeted analysis in the *ee* (left) and $\mu\mu$ (right) final states.

5.1.5 Signal Regions

The same strategy is followed as in the inclusive analysis. *MET* cuts are added on top of the preselection in order to gain sensitivity to new physics scenarios with *MET*. Because the backgrounds are greatly reduced in this analysis as compared with the inclusive analysis, the *MET* cuts can be looser. We keep the low *MET* control regions of *MET* > 30 and 60 GeV. A loose signal region of *MET* > 80 GeV is useful for models with modest *MET*. The higher *MET* signal regions are *MET* > 100, 150, and 200 GeV.

Table 5.1: Data and Monte Carlo yields for the preselection with $N_{\text{jets}} \geq 2$ for 4.98 fb^{-1}.

Sample	ee	$\mu\mu$	$e\mu$	tot
WJets	2.3 ± 2.2	0.0 ± 0.0	0.0 ± 0.0	2.3 ± 2.2
WW	2.1 ± 0.2	2.6 ± 0.2	4.9 ± 0.3	9.7 ± 0.5
WZ	136.8 ± 1.2	137.5 ± 1.2	0.7 ± 0.1	275.1 ± 1.7
ZZ	121.8 ± 0.9	125.6 ± 0.8	0.1 ± 0.0	247.5 ± 1.2
Single Top	1.0 ± 0.2	1.1 ± 0.3	1.7 ± 0.3	3.8 ± 0.5
$t\bar{t}$	9.2 ± 0.4	9.1 ± 0.4	19.1 ± 0.5	37.4 ± 0.7
Z+Jets	10951.2 ± 80.6	11566.7 ± 78.7	1.8 ± 0.9	22519.6 ± 112.7
Total MC	11224.4 ± 80.7	11842.7 ± 78.7	28.4 ± 1.2	23095.5 ± 112.7
Data	9734	10314	28	20076

5.2 Changes to Background Predictions

The selection criteria described in Sec. 5.1 change the sample composition of this targeted analysis compared to the inclusive analysis of Chapter 4. This change in sample composition requires some minimal changes in the background prediction methods used in the inclusive analysis. The overall strategy, and almost all of the details of the background predictions methods will remain the same as previously described.

5.2.1 Changes to MET Templates Method

The only change to the MET templates method is to use the same b jet veto when selecting the control sample as is used to select the signal sample (see Sec. 5.1.1). This is done for consistency, however, it is a very small effect. The presence of b jets can affect the MET due to semi-leptonic b decays, but neutrinos from these decays do not have much p_T, and jet mismeasurement is a larger effect overall.

The dijet mass requirement of Sec. 5.1.2 does not affect the MET in any significant way, so there is no need to apply this cut to the control sample.

Events with leptons are not used for the MET templates control sample, so the third lepton veto does not change these samples.

The last change in methodology for the MET templates method is to use the $\gamma+$ jets control sample exclusively.

5.2.2 Changes to Opposite Flavor Prediction

In the inclusive analysis, the opposite flavor $(e\mu)$ control sample is dominated by $t\bar{t}$ for all MET values (see Sec. 4.3.1). We thus find that K (the fraction of opposite flavor events inside the Z window) is constant as a function of MET, and has the value $K = 0.16$. In this targeted analysis, the b jet veto is very effective in suppressing the $t\bar{t}$ background. Therefore, at low MET, the presence of Z $\rightarrow \tau\tau$ is no longer negligible. This process has a dilepton mass distribution which is different from that of $t\bar{t}$, which affects the value of K at low MET. At high MET, diboson backgrounds are a significant fraction of the $t\bar{t}$ background, although the dilepton mass distribution is similiar for these

two samples. Because of this changing sample composition as a function of *MET*, we also find that the value of *K* changes with *MET*. This is shown in Fig. 5.3 (left).

We again derive the systematic uncertainty on this prediction from a comparison between data and MC. The data and MC agree to about 17% up to $MET > 100$ GeV. We therefore take 17% as the systematic due to *K*. This is added in quadrature with the 7% due to the electron to muon efficiency ratio (see Sec. 4.3.3), and rounded up to 20%. For $MET > 150$ GeV, there are no opposite flavor events in the Z window, so we use the statistical uncertainty on the MC prediction of this quantity as a systematic. For *MET* > 150 GeV, this is 25%, and for $MET > 200$ GeV, it is 60%. This is summarized in Tab. 5.2.
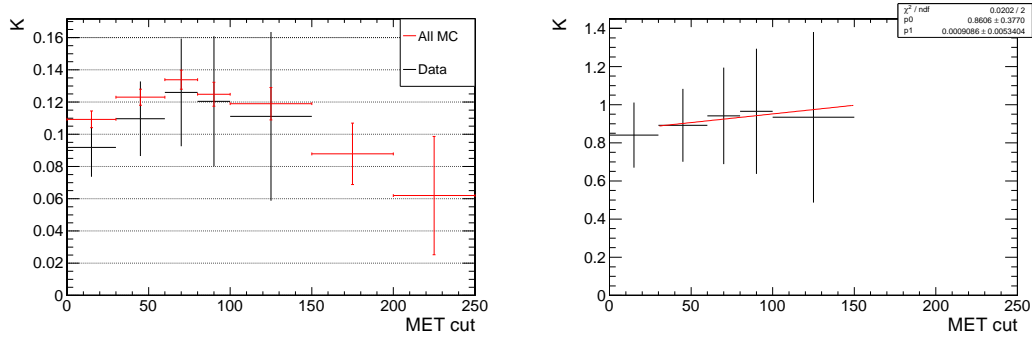
Figure 5.3: The left plot shows K as a function of *MET* in MC (red) and data (black). The bin low edge corresponds to the *MET* cut, and the bins are inclusive. The MC used is a sum of all SM MC used in the yield table of section 5.1.4. The right plot is the ratio of K in data to MC. The ratio is fit to a line whose slope is consistent with zero (the fit parameters are 0.9 ± 0.4 for the intercept and 0.001 ± 0.005 for the slope).

Table 5.2:   The values of K used in the OF background prediction. The uncertainties shown are the total relative systematic used for the OF prediction, which is the systematic uncertainty from K added in quadrature with a 7% uncertainty from the electron to muon efficieny ratio as assessed in the inclusive analysis.

MET Cut	K	Relative Systematic
30	0.12	20%
60	0.13	20%
80	0.12	20%
100	0.12	20%
150	0.09	25%
200	0.06	60%

5.3 Experimental Results

The background prediction methods described above are applied to the full 2011 dataset and compared with the observed yield. Results are shown in Fig. 5.4 and Tabs. 5.3 and 5.4. As was done in the inclusive analysis, we separately apply the background prediction methods to the run 2011A and run 2011B datasets; see Sec. 5.3.1.

Finally, the results of the background prediction obtained with the b veto cut applied, but the dijet mass and third lepton veto cuts *not applied* are shown in Sec. 5.3.2. These results are not used in the interpretation sections which follow.

5.3.1 Results for 2011A and 2011B separately

The results for run 2011A are shown in Tab. 5.5 and for run 2011B in Tab. 5.6. See Sec. 4.5.1 for details of the run periods.

5.3.2 Results for Other Signal Region

In this Section, the results of the background prediction obtained with the b veto cut applied, but the dijet mass and third lepton veto cuts *not applied* are shown in Tab. 5.7. These results are not used in the interpretation sections which follow.

Table 5.3: Summary of data yields and predicted backgrounds in each of the signal regions. The total background (total bkg) is the sum of the Z + jets background predicted from the γ + jets *MET* templates, the flavor-symmetric background predicted from opposite-flavor events (OF bkg), and the WZ/ZZ background predicted from MC (WZ/ZZ bkg). The total predicted background is compared to the observed data yields (data). All uncertainties indicate the statistical and systematic components added in quadrature. The 95% confidence level observed and expected upper limits (UL) on the non-SM contributions to the signal regions is also indicated. The expected yields from an example point of the WZ + *MET* model ($m_\chi = 200$ GeV, massless LSP) and GMSB model ($m_\chi = 230$ GeV) described in Sec. 2.3 are also indicated.

	MET > 30 GeV	*MET* > 60 GeV	*MET* > 80 GeV
Z + jets bkg	2339 ± 750	40 ± 13	7.6 ± 2.5
OF bkg	27 ± 6	17 ± 4	10.0 ± 2.3
WZ/ZZ bkg	59 ± 30	10 ± 5	5.8 ± 2.9
Total bkg	2426 ± 750	67 ± 15	23.4 ± 4.5
Data	2478	62	15
Observed UL	-	24	7.3
Expected UL	-	27	12
WZ model (200/0)	13 ± 3	11 ± 2	8.9 ± 2.2
GMSB model (230)	12 ± 1	10 ± 1	8.3 ± 0.8

	MET > 100 GeV	*MET* > 150 GeV	*MET* > 200 GeV
Z + jets bkg	2.4 ± 0.8	0.6 ± 0.2	0.2 ± 0.1
OF bkg	5.4 ± 1.4	0.8 ± 0.3	0.06 ± 0.07
WZ/ZZ bkg	3.6 ± 1.8	1.2 ± 0.6	0.4 ± 0.2
Total bkg	11.4 ± 2.4	2.6 ± 0.7	0.7 ± 0.3
Data	8	2	0
Observed UL	6.4	4.3	3.0
Expected UL	8.4	4.6	3.0
WZ model (200/0)	6.7 ± 2.1	2.1 ± 1.0	0.5 ± 0.2
GMSB model (230)	6.6 ± 0.8	2.6 ± 0.5	0.6 ± 0.2

Table 5.4: Summary of data yields and predicted backgrounds in exclusive *MET* signal regions. Details are the same as in Table 5.3.

MET	30 - 60 GeV	60 - 80 GeV	80 - 100 GeV
Z + jets background	2298 ± 737	32.9 ± 11.1	5.2 ± 1.8
OF background	11 ± 2	6.6 ± 1.6	4.6 ± 1.2
WZ/ZZ background	50 ± 25	3.9 ± 2.0	2.2 ± 1.1
Total background	2359 ± 737	43.4 ± 11.4	12.0 ± 2.4
Data	2416	47	7

MET	100 - 150 GeV	150 - 200 GeV	> 200 GeV
Z + jets background	1.7 ± 0.6	0.4 ± 0.2	0.2 ± 0.09
OF background	4.6 ± 1.2	0.8 ± 0.3	0.06 ± 0.07
WZ/ZZ background	2.5 ± 1.3	0.7 ± 0.4	0.4 ± 0.2
Total background	8.8 ± 1.8	1.9 ± 0.5	0.7 ± 0.3
Data	6	2	0

Table 5.5: Results of background predictions for run 2011A only.

	$MET > 30$ GeV	$MET > 60$ GeV	$MET > 80$ GeV
Z	701.88 ± 225.21	11.36 ± 4.15	2.54 ± 0.90
OF	14.08 ± 3.10	8.73 ± 2.05	5.65 ± 1.40
VZ	25.00 ± 12.50	4.10 ± 2.05	2.45 ± 1.23
Total Pred	740.95 ± 225.57	24.20 ± 5.06	10.65 ± 2.07
Data	732	20	6

	$MET > 100$ GeV	$MET > 150$ GeV	$MET > 200$ GeV
Z	0.8068 ± 0.3053	0.2502 ± 0.1395	0.0633 ± 0.0511
OF	2.89 ± 0.83	0.5414 ± 0.2592	0.0602 ± 0.0701
VZ	1.54 ± 0.77	0.4870 ± 0.2513	0.1739 ± 0.1049
Total Pred	5.23 ± 1.17	1.28 ± 0.39	0.2974 ± 0.1361
Data	4	2	0
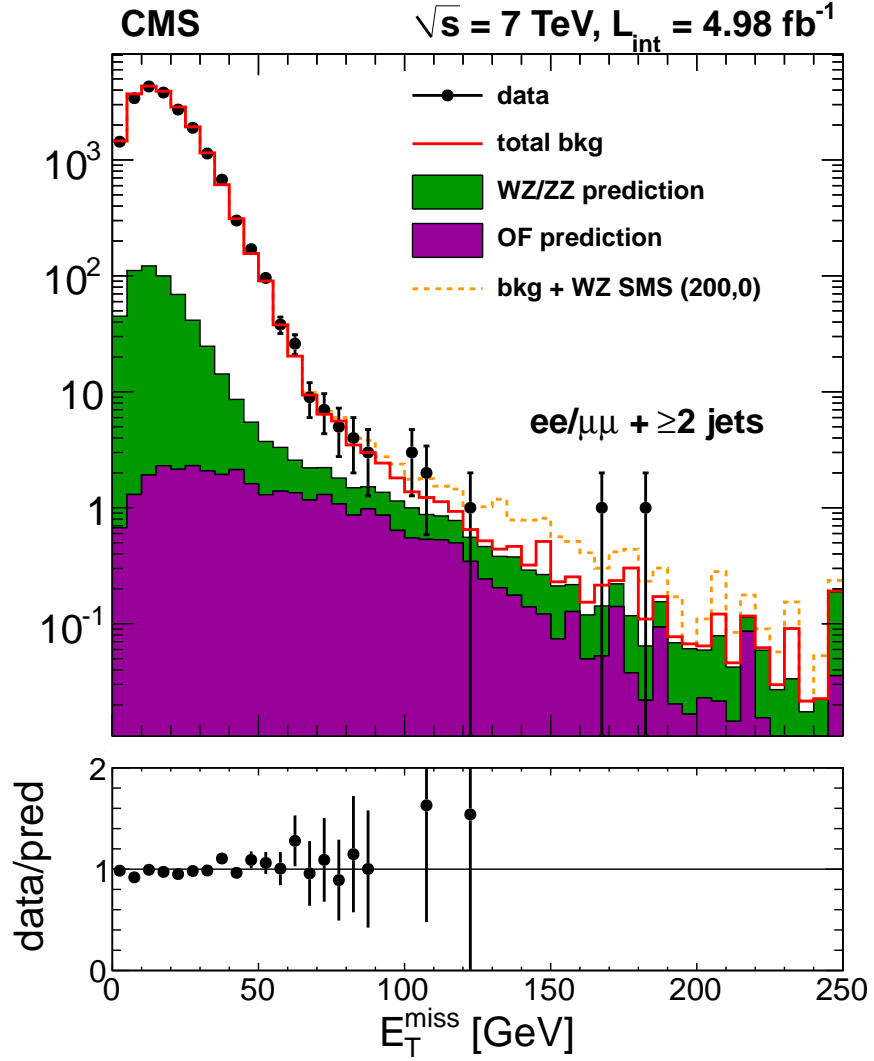
Figure 5.4: The total predicted *MET* distribution (red) is the sum of the OF prediction (purple histogram), the diboson prediction (green histogram) and the *MET* template prediction from γ + jets. Data is overlayed as black data points. For illustration of the *MET* distribution in a signal model (see Sec.5.6), the WZ SMS (point $m_\chi, m_{LSP} = 200, 0$ GeV) *MET* distribution added to the total background prediction is shown in orange. Below the *MET* distribution is plotted the ratio of the observed (data) and predicted *MET*.

Table 5.6: Results of background predictions for run 2011B only.

	$MET > 30$ GeV	$MET > 60$ GeV	$MET > 80$ GeV
Z	1636.86 ± 525.56	29.12 ± 9.76	5.02 ± 1.71
OF	13.35 ± 2.96	7.82 ± 1.86	4.33 ± 1.13
VZ	34.40 ± 17.20	5.64 ± 2.82	3.37 ± 1.69
Total Pred	1684.61 ± 525.85	42.58 ± 10.33	12.73 ± 2.65
Data	1746	42	9

	$MET > 100$ GeV	$MET > 150$ GeV	$MET > 200$ GeV
Z	1.55 ± 0.56	0.3781 ± 0.1465	0.1269 ± 0.0553
OF	2.53 ± 0.75	0.2707 ± 0.1703	0.0000 ± 0.0000
VZ	2.12 ± 1.06	0.6701 ± 0.3458	0.2393 ± 0.1443
Total Pred	6.19 ± 1.42	1.32 ± 0.41	0.3662 ± 0.1545
Data	4	0	0

Table 5.7: Results table for signal region with b veto but *without* dijet mass nor third lepton veto cuts. For each signal region (*MET* cut) is tabulated each background prediction, the total background prediction, the observed yield in data, and the 95% CLs upper limit on non-Standard Model yield.

	$MET > 30$ GeV	$MET > 60$ GeV	$MET > 80$ GeV
Z	10478 ± 3356	306 ± 99	57 ± 19
OF	132 ± 23	81 ± 14	48 ± 8
VZ	188 ± 94	63 ± 31	40 ± 20
Total Pred	10799 ± 3357	450 ± 105	145 ± 29
Data	10997	440	144

	$MET > 100$ GeV	$MET > 150$ GeV	$MET > 200$ GeV
Z	18.0 ± 6.0	5.1 ± 1.9	1.68 ± 0.76
OF	26.7 ± 9.3	4.7 ± 2.2	0.72 ± 0.53
VZ	26.1 ± 13.1	9.7 ± 5.1	4.06 ± 2.44
Total Pred	70.8 ± 17.1	19.5 ± 5.8	6.46 ± 2.61
Data	71	15	6

5.4 Interpretation of Experimental Results: Efficiency Models

The interpretation for the Electroweakino targeted analysis will follow the same approach as the inclusive analysis interpretation of Secs. 4.6 and 4.7. The lepton selection is identical between the two analyses, so the results of Sec. 4.6.3 apply equally well here.

Efficiency Models are covered in this section, and simplified models are covered in Sec. 5.6.

This analysis requires two or more jets. Though jets are reconstructed as clusters of energy in the calorimeters, they originate from the hard scatter as colored partons. In order to parameterize the detector response to jets, we measure (in MC) the efficiency to reconstruct a jet of $p_T > 30$ GeV (the minimum jet p_T used in this analysis) as a function of the generator level parton p_T. The efficiency as a function of parton p_T is then fit to the following equation.

$$\varepsilon(x) = p_6 + p_4\left[\operatorname{erf}\left(\frac{x - p_0}{p_1}\right) + 1\right] + p_5\left[\operatorname{erf}\left(\frac{x - p_2}{p_3}\right) + 1\right] \tag{5.1}$$

Where 'erf' is the error function defined in Eq. 4.2. The results are shown in Fig. 5.5. The efficiency is measured separately for different parton types: gluons, light quarks (u, d, s), c quarks, and b quarks. It is found that the reconstruction efficiency does not depend on parton type.

The b jet veto efficiency is necessary in order to model the efficiency to reject signal events which have the decays $Z \to b\bar{b}$ and $W \to c\bar{s}$. It is also necessary to know the mis-tag rate, that is, the probability to incorrectly tag a light quark jet or gluon jet as a b jet. The latter effect is a larger source of inefficiency in the WZ simplified model used to derive these efficiencies. (See Sec. 5.6 for information on simplified models used in this analysis.) Recall that the loose working point is used for jet $p_T < 100$ GeV, and the medium working point is used for jet $p_T > 100$ GeV. The efficiencies as a function of parton p_T are shown in Fig. 5.6 and the results of fitting these efficiencies are shown in Tab. 5.8.

Finally, as is done in the inclusive analysis in Sec. 4.6.4, we measure (again, in
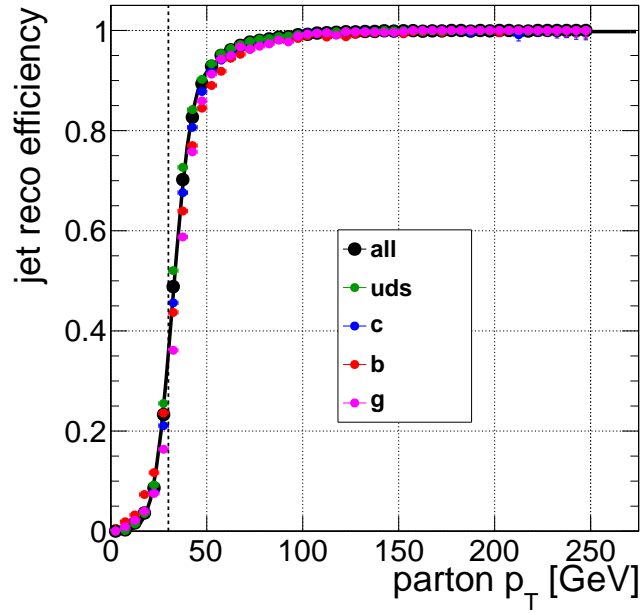
Figure 5.5: The efficiency for parton-jets to be reconstructed and identified as jets in the analysis, parameterized by the parton-jet p_T. Fit parameters are shown in Tab. 5.8.

MC) the efficiency for the CMS detector to reconstruct *MET* as a function of generator level *MET* for the five *MET* signal regions used in this analysis. For *MET*, we fit the efficiency turn on to Eq. 4.1. The efficiency is shown in Fig. 5.7, and the values of the fit parameters are shown in Tab. 5.7.
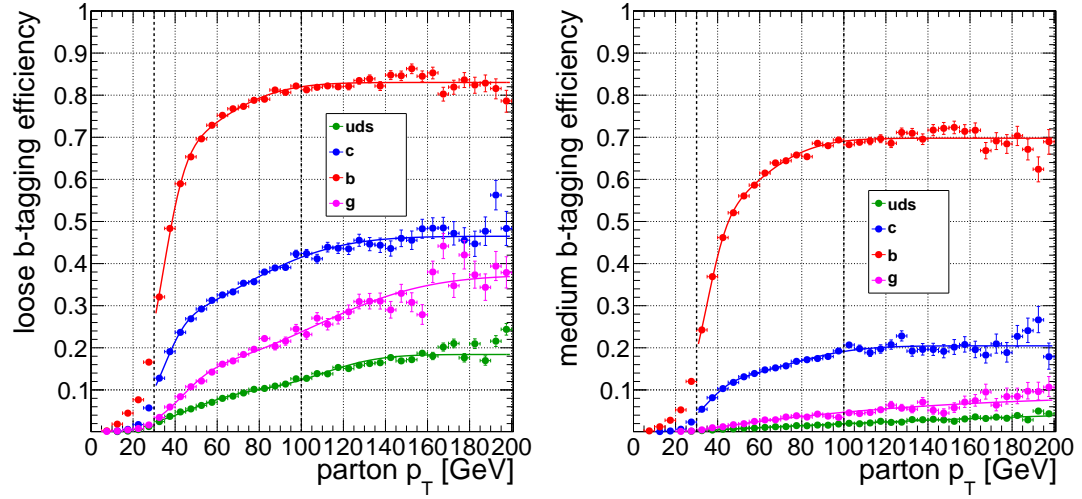
Figure 5.6: The efficiency for parton-jets to be reconstructed and identified as b-jets in the analysis, parameterized by the parton-jet p_T, for the loose (left) and medium (right) working points. Fit parameters are shown in Tab. 5.8.

Table 5.8: Values of the fitted parameters (see Eq. 5.1) for various jet selections. The efficiencies for jet reconstruction (Fig. 5.5) and b tagging (Fig. 5.6) for the TCHE loose and medium working points for each parton-jet flavor.

Variable	p_0	p_1	p_2	p_3	p_4	p_5	p_6
jet reconstruction	52	29	32	11	0.07	0.43	0
loose b-tagging (b)	47	42	34	12	0.14	0.27	0
loose b-tagging (c)	68	53	34	12	0.13	0.10	0
loose b-tagging (g)	106	60	43	17	0.12	0.06	0
loose b-tagging (q)	78	35	78	38	-0.92	1.02	0
medium b-tagging (b)	46	38	35	11	0.17	0.18	0
medium b-tagging (c)	34	13	72	38	0.06	0.05	0
medium b-tagging (g)	-32191	113547	-287	296	-0.96	0.67	0
medium b-tagging (q)	-718	2523	-333	729	-0.40	0.35	0
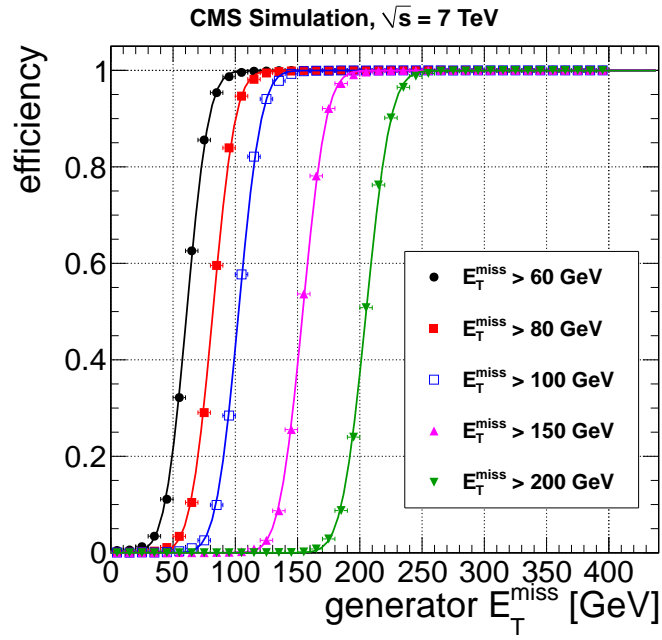
Figure 5.7: The efficiency to pass the MET > 60, 80, 100, 150, and 300 GeV requirements as a function of the generator level MET, evaluated using the WZ simplified model.

Table 5.9: Values of the fitted parameters (see Eq. 4.1) for the MET selection requirements displayed in Fig. 5.7.

MET cut	$\varepsilon_{\text{plateau}}$	x_{offset}	σ
$MET > 60$ GeV	1.00	61.0	19.7
$MET > 80$ GeV	1.00	82.0	20.1
$MET > 100$ GeV	1.00	102.7	20.3
$MET > 150$ GeV	1.00	154.2	21.0
$MET > 200$ GeV	1.00	205.1	22.0

5.5 Interpretation of Experimental Results: GMSB Model

For this targeted analysis, we consider one 'full' model which is the GMSB model described in Sec. 2.3. I will summarize the main features of this model relevant for this section. The colored sparticles are very massive, so electroweak production is the only way to produce the new particles of this model at the LHC. The sparticles which can be produced are the charginos ($\tilde{\chi}^{\pm}$) and neutralinos ($\tilde{\chi}^0$). The mass hierarchy and branching ratios are such that the charginos are just barely heavier than the neutralinos, so they decay to a neutralino and the other decay products are too low energy to be detected. There are therefore two neutralinos in every event. The neutralinos may decay via a Z, a photon, or a higgs. In the case where both neutralinos decay to a Z, there are two Zs in the final state. There is only one parameter in the model which is the mass of the neutralino (m_{χ}).

The final state of this model is therefore ZZ + *MET*, which is exactly what this analysis is designed to measure. One Z is found in a leptonic decay while the other is found in a hadronic decay to two jets.

The approach taken for the interpretation for this GMSB model is very similiar to the one taken in the inclusive analysis for the interpretation in the context of simplified models (Sec. 4.7). We provide efficiencies and cross section upper limits at each parameter point in the model.

The systematic uncertainties on the signal efficiency and acceptance are determined in the same way as described in Sec. 4.7.1.

The exclusion procedure used is the same as described in Sec. 4.7.2.

We show the efficiencies and cross section ($\sigma \times$ BR) upper limits in Tab. 5.10. This information is displayed graphically in Fig. 5.8.

Table 5.10: Summary table for the GMSB model. For each mass parameter m_χ considered, we indicate the efficiency times acceptance normalized to the number of ZZ events (ε), the 95% CL upper limit on the cross section times branching ratio ($\sigma \times$ BR UL), the inclusive signal cross section (σ), the branching ratio to the ZZ + *MET* final state (BR), and the product of these last two quantities ($\sigma \times$ BR).

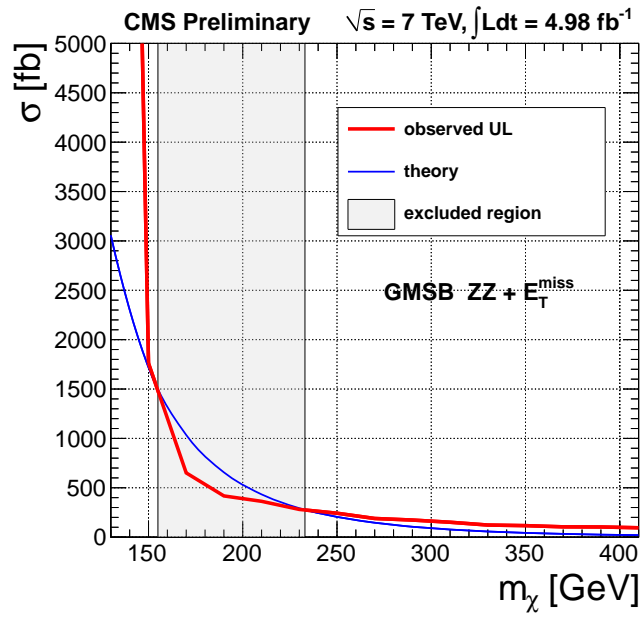| m_χ (GeV)	ε (10^{-3})	$\sigma \times$ BR UL	σ	BR	$\sigma \times$ BR
130	0.05 ± 0.01	21094	3057	1.00	3057
150	0.5 ± 0.1	1760	1719	0.99	1702
170	1.4 ± 0.3	651	1035	0.96	994
190	2.8 ± 0.4	417	656	0.94	617
210	4.1 ± 0.5	363	433	0.92	398
230	4.9 ± 0.6	281	293	0.90	264
250	5.9 ± 0.6	242	205	0.89	182
270	7.0 ± 0.6	189	146	0.88	128
290	7.2 ± 0.6	173	105	0.87	91
310	7.9 ± 0.6	151	77	0.87	67
330	8.6 ± 0.7	122	57	0.86	49
350	8.9 ± 0.7	117	43	0.86	37
370	9.4 ± 0.7	104	33	0.85	28
390	9.5 ± 0.7	103	25	0.85	21
410	10 ± 0.8	95	20	0.85	17

Figure 5.8: Interpretation in the GMSB model. The observed cross section upper limits (red line) are compared with the theory predictions (blue line). The excluded region m_χ 155–233 GeV is indicated by the gray shaded box.

5.6 Interpretation of Experimental Results: Simplified Models

For the interpretation of this targeted analysis in the context of simplified models, a very similar approach is taken as in the inclusive anslysis (Sec. 4.7). The only major difference is the model itself. The simplified model used in the inclusive analysis featured strong (QCD) production of gluinos which then decayed to neutralinos ($\tilde{\chi}^0$). The simplified model used in this section features direct electroweak production of neutralinos and charginos ($\tilde{\chi}^\pm$). For the reasons outlined in Sec. 2.2.4, a simplified model with neutralino-neutralino or chargino-chargino production suffers from lower production cross section relative to neutralino-chargino production and will therefore not be used for this analysis.

In simplified models, branching ratios are all set to unity. In this particular simplified model, the neutralino ($\tilde{\chi}^0_2$) always decays to a Z and the LSP ($\tilde{\chi}^0_1$), while the chargino ($\tilde{\chi}^\pm$) decays to a W and the LSP. A diagram illustrating this is shown in Fig. 5.9. This analysis then selects the Z via its decay to leptons and the W via its decay to jets. The LSPs produce *MET*.

The interpretation for this model follows the same procedure as described in Sec. 5.5 and Sec. 4.7.2. The results are shown in Tab. 5.11 and in Fig. 5.10 and Fig. 5.11.
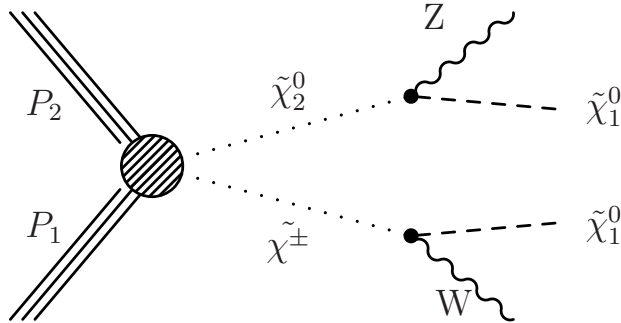
Figure 5.9: Diagram for the WZ simplified model.

Table 5.11: Summary table for the WZ + *MET* model with LSP mass equal to 0 and 50 GeV. For each mass parameter m_χ considered, we indicate the efficiency times acceptance normalized to the number of WZ events (ε). The theory cross sections for the wino-like (σ_{wino}) and higgsino-like ($\sigma_{higgsino}$) scenarios (see Sec. 2.3) are also indicated (see Sec. 2.2.2).

m_χ (GeV)	LSP mass 0 GeV ε (10^{-3})	LSP mass 50 GeV ε (10^{-3})	theory σ_{wino} (fb)	$\sigma_{higgsino}$ (fb)
125	0.2 ± 0.0	0	3960	1980
150	0.6 ± 0.3	0.1 ± 0.0	1949	975
175	1.6 ± 0.4	0.9 ± 0.3	1052	526
200	2.2 ± 0.7	1.5 ± 0.5	614	307
225	2.8 ± 0.6	2.6 ± 0.5	377	189
250	3.3 ± 0.7	3.4 ± 0.8	239	120
275	3.6 ± 0.7	3.7 ± 0.8	157	79
300	4.2 ± 0.8	3.8 ± 0.8	106	53
325	4.9 ± 0.9	4.9 ± 0.9	73	36
350	5.2 ± 0.8	5.1 ± 0.9	51	26
375	5.2 ± 0.9	4.7 ± 0.8	37	19
400	4.9 ± 0.9	5.4 ± 0.8	26	13
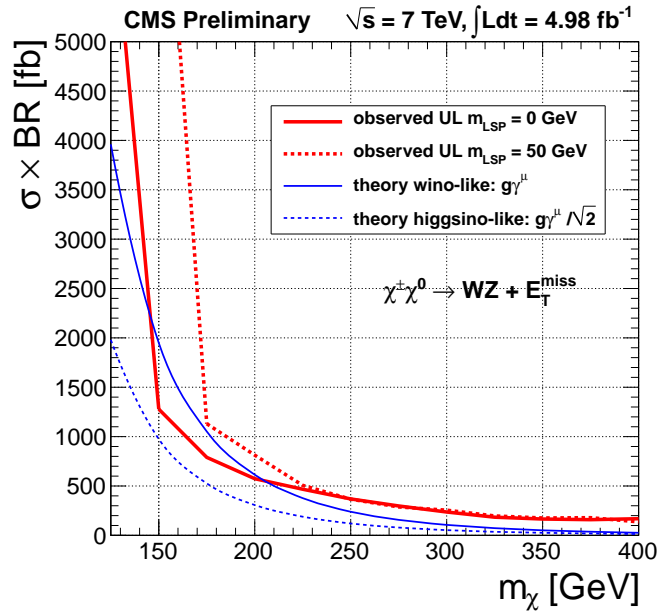
Figure 5.10: Interpretation in the WZ simplified model. The observed cross section upper limits (red line) are compared with the theory predictions (blue line). We display the observed cross section limits for massless LSP (solid red line) and LSP with mass 50 GeV (dotted line). We also display both the wino-like (solid blue line) and higgsino-like (dashed blue line) (see text for details).
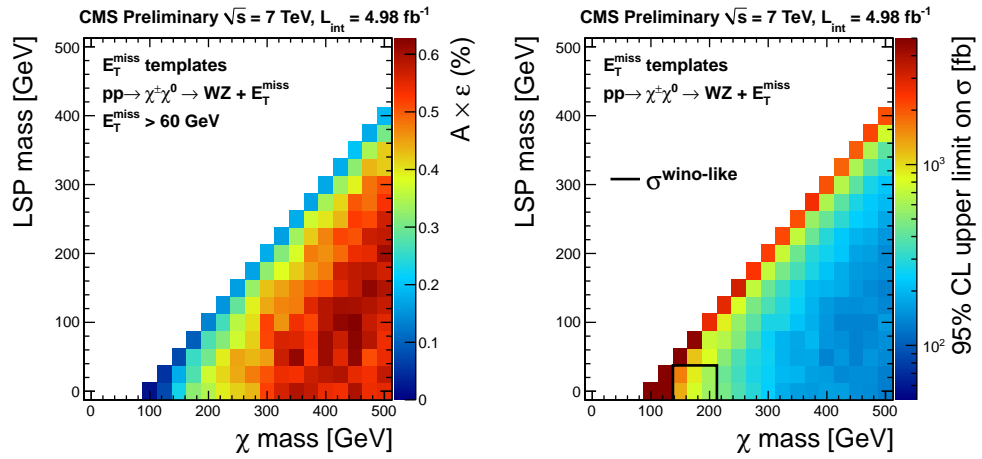
Figure 5.11: Interpretation in the WZ SMS model. The signal efficiency times acceptance to pass the *MET* > 60 GeV signal region requirement is indicated in the left plot. The observed 95% CL cross section upper limits are indicated in the right plot. The solid contour in this plot indicates the excluded region, assuming the pure wino-like cross section.

Selected figures and tables from this Chapter are published in: CMS Collaboration, "Search for electroweak production of charginos and neutralinos using leptonic final states in pp collisions at sqrt s = 7 TeV", arXiv:1209.6620.

Bibliography

[1] S. Weinberg, "The Discovery of Subatomic Particles (Revised Edition)". Cambridge University Press, 2003.

[2] D. Griffiths, "Introduction to Elementary Particles". Wiley-VCH, 2008.

[3] D. H. Perkins, "Introduction to High Energy Physics". Cambridge University Press, 2000.

[4] J. Gleick, "Genius: The Life and Science of Richard Feynman". Vintage, 1993.

[5] WMAP Collaboration, "Seven-Year Wilkinson Microwave Anisotropy Probe (WMAP) Observations: Cosmological Interpretation", *Astrophys. J. Suppl.* **192** (2011) 18. `doi:10.1088/0067-0049/192/2/18`.

[6] J. Ellis, J. S. Hagelin, D. V. Nanopoulos, K. Olive, and M. Srednicki, "Supersymmetric Relics from the Big Bang", *Nucl. Phys. B* **238** (1984) 453. `doi:10.1016/0550-3213(84)90461-9`.

[7] CMS Collaboration, "Inclusive search for squarks and gluinos in pp collisions at $\sqrt{s} = 7$ TeV", *Phys. Rev. D* **85** (2012) 012004, `arXiv:1107.1279`. `doi:10.1103/PhysRevD.85.012004`.

[8] CMS Collaboration, "Search for supersymmetry in events with b jets and missing transverse momentum at the LHC", *JHEP* **07** (2011) 113, `arXiv:1106.3272`. `doi:10.1007/JHEP07(2011)113`.

[9] CMS Collaboration, "Search for Supersymmetry at the LHC in Events with Jets and Missing Transverse Energy", *Phys. Rev. Lett.* **107** (2011) 221804, `arXiv:1109.2352`. `doi:10.1103/PhysRevLett.107.221804`.

[10] CMS Collaboration, "Search for supersymmetry in pp collisions at $\sqrt{s} = 7$ TeV in events with a single lepton, jets, and missing transverse momentum", *JHEP* **08** (2011) 156, `arXiv:1107.1870`. `doi:10.1007/JHEP08(2011)156`.

[11] CMS Collaboration, "Search for physics beyond the standard model in opposite-sign dilepton events at $\sqrt{s} = 7$TeV", *JHEP* **06** (2011) 026, `arXiv:1103.1348`. `doi:10.1007/JHEP06(2011)026`.

[12] CMS Collaboration, "Search for new physics with same-sign isolated dilepton events with jets and missing transverse energy at the LHC", *JHEP* **06** (2011) 077, `arXiv:1104.3168`. `doi:10.1007/JHEP06(2011)077`.

[13] CMS Collaboration, "Search for Supersymmetry in *pp* Collisions at $\sqrt{s} = 7$ TeV in Events with Two Photons and Missing Transverse Energy", *Phys. Rev. Lett.* **106** (2011) 211802, `arXiv:1103.0953`. `doi:10.1103/PhysRevLett.106.211802`.

[14] CMS Collaboration, "Search for supersymmetry in events with a lepton, a photon, and large missing transverse energy in pp collisions at $\sqrt{s} = 7$ TeV", *JHEP* **06** (2011) 093, `arXiv:1105.3152`. `doi:10.1007/JHEP06(2011)093`.

[15] ATLAS Collaboration, "Searches for supersymmetry with the ATLAS detector using final states with two leptons and missing transverse momentum in $\sqrt{s} = 7$ TeV proton-proton collisions", *Phys. Lett. B* **709** (2012) 137. `doi:10.1016/j.physletb.2012.01.076`.

[16] ATLAS Collaboration, "Search for supersymmetric particles in events with lepton pairs and large missing transverse momentum in $\sqrt{s} = 7$ TeV proton-proton collisions with the ATLAS experiment", *Eur. Phys. J. C* **71** (2011) 1682. `doi:10.1140/epjc/s10052-011-1682-6`.

[17] H. Baer, X. Tata, and J. Woodside, "Z^0 + Jets + (Missing) p_T Events as a Signal for Supersymmetry at the Tevatron Collider", *Phys. Rev. D* **42** (1990) 1450. `doi:10.1103/PhysRevD.42.1450`.

[18] S. Ambrosanio, G. L. Kane, G. D. Kribs, S. P. Martin, and S. Mrenna, "Search for Supersymmetry with a Light Gravitino at the Fermilab Tevatron and CERN LEP Colliders", *Phys. Rev. D* **54** (1996) 5395, `arXiv:hep-ph/9605398`. `doi:10.1103/PhysRevD.54.5395`.

[19] CMS Collaboration, "Search for physics beyond the standard model in events with a Z boson, jets, and missing transverse energy in pp collisions at $\sqrt{s} = 7$ TeV", *Physics Letters B* **716** (2012), no. 2, 260 – 284. `doi:10.1016/j.physletb.2012.08.026`.

[20] CMS Collaboration, "Search for electroweak production of charginos and neutralinos using leptonic final states in *pp* collisions at $\sqrt{s} = 7$ TeV", `arXiv:1209.6620`.

[21] M. E. Peskin and D. V. Schroeder, "An Introduction to Quantum Field Theory". Westview Press, 1995.

[22] F. Halzen and A. D. Martin, "Quarks and Leptons: an Introductory Course in Modern Particle Physics". John Wiley & Sons, Inc., 1984.

[23] Super-Kamiokande Collaboration, "Search for Proton Decay via $p \rightarrow e^+\pi^0$ and $p \rightarrow \mu^+\pi^0$ in a Large Water Cherenkov Detector", *Phys. Rev. Lett.* **102** (Apr, 2009) 141801. `doi:10.1103/PhysRevLett.102.141801`.

[24] WMAP Collaboration, "Seven-year Wilkinson Microwave Anisotropy Probe (WMAP) Observations: Sky Maps, Systematic Errors, and Basic Results", *The Astrophysical Journal Supplement Series* **192** (2011), no. 2, 14.

[25] P. Fayet, "Supergauge invariant extension of the Higgs mechanism and a model for the electron and its neutrino", *Nucl. Phys. B* **90** (1975) 104. `doi:10.1016/0550-3213(75)90636-7`.

[26] H. E. Haber and G. L. Kane, "The Search for Supersymmetry: Probing Physics Beyond the Standard Model", *Phys.Rept.* **117** (1985) 75–263. `doi:10.1016/0370-1573(85)90051-1`.

[27] K. T. Matchev and S. D. Thomas, "Higgs and *Z* Boson Signatures of Supersymmetry", *Phys. Rev. D* **62** (2000) 077702. `doi:10.1103/PhysRevD.62.077702`.

[28] J. T. Ruderman and D. Shih, "General Neutralino NLSPs at the Early LHC", `arXiv:1103.6083`.

[29] CMS Collaboration, "The CMS Experiment at the CERN LHC", *JINST* **03** (2008) S08004. `doi:10.1088/1748-0221/3/08/S08004`.

[30] CMS Collaboration, "CMS physics: Technical design report", Technical Report CERN-LHCC-2006-001, CMS-TDR-008-1, (2006).

[31] K. Kleinknecht, "Detectors for particle radiation". Cambridge University Press, 1998.

[32] Particle Data Group Collaboration, "Review of Particle Physics", *Journal of Physics G* **37** (2010), no. 075021,.

[33] T. Sjöstrand, S. Mrenna, and P. Z. Skands, "PYTHIA 6.4 physics and manual", *JHEP* **05** (2006) 026. `doi:10.1088/1126-6708/2006/05/026`.

[34] MadGraph/MadEvent Collaboration, "MadGraph/MadEvent v4: the new web generation", *JHEP* **09** (2007) 028. `doi:10.1088/1126-6708/2007/09/028`.

[35] Geant4 Collaboration, "GEANT4 – a simulation toolkit", *Nucl. Instr. Meth. A* **506** (2003) 250. `doi:10.1016/S0168-9002(03)01368-8`.

[36] CMS Collaboration, "Determination of jet energy calibration and transverse momentum resolution in CMS", *JINST* **6** (2011) P11002. `doi:10.1088/1748-0221/6/11/P11002`.

[37] M. Cacciari, G. P. Salam, and G. Soyez, "The anti-k_t jet clustering algorithm", *JHEP* **04** (2008) 063. `doi:10.1088/1126-6708/2008/04/063`.

[38] CMS Collaboration, "Commissioning of the Particle-Flow Reconstruction in Minimum-Bias and Jet Events from pp Collisions at 7 TeV", CMS Physics Analysis Summary CMS-PAS-PFT-10-002, (2010).

[39] CMS Collaboration, "First Measurement of the Cross Section for Top-Quark Pair Production in Proton-Proton Collisions at $\sqrt{s} = 7$ TeV", *Phys. Lett. B* **695** (2011) 424. `doi:10.1016/j.physletb.2010.11.058`.

[40] V. Pavlunin, "Modeling Missing Transverse Energy in V+jets at CERN LHC", *Phys. Rev. D* **81** (2010) 035005. `doi:10.1103/PhysRevD.81.035005`.

[41] T. Junk, "Confidence Level Computation for Combining Searches with Small Statistics", *Nucl. Instr. Meth. A* **434** (1999) 435. `doi:10.1016/S0168-9002(99)00498-2`.

[42] A. L. Read, "Modified Frequentist Analysis of Search Results (the *CL$_s$* Method)", in *Workshop on Confidence Limits, Jan 17-18, 2000*, F. James, L. Lyons, and Y. Perrin, eds., p. 81. CERN, Switzerland, 2000.

[43] G. Kane, "Study of Constrained Minimal Supersymmetry", *Phys. Rev. D* **49** (1994) 6173. `doi:10.1103/PhysRevD.49.6173`.

[44] CMS Collaboration, "CMS Technical Design Report, Volume II: Physics Performance", *J. Phys. G* **34** (2007) 995. `doi:10.1088/0954-3899/34/6/S01`.

[45] Daniele Alves, Nima Arkani-Hamed, Sanjay Arora, Yang Bai, Matthew Baumgart, Joshua Berger, Matthew Buckley, Bart Butler, Spencer Chang, Hsin-Chia Cheng, Clifford Cheung, R. Sekhar Chivukula, Won Sang Cho, Randy Cotta, Mariarosaria D'Alfonso, Sonia El Hedri, Rouven Essig, Jared A. Evans, Liam Fitzpatrick, Patrick Fox, Roberto Franceschini, Ayres Freitas, James S. Gainer, Yuri Gershtein, Richard Gray, Thomas Gregoire, Ben Gripaios, Jack Gunion, Tao Han, Andy Haas, Per Hansson, JoAnne Hewett, Dmitry Hits, Jay Hubisz, Eder Izaguirre, Jared Kaplan, Emanuel Katz, Can Kilic, Hyung-Do Kim, Ryuichiro Kitano, Sue Ann Koay, Pyungwon Ko, David Krohn, Eric Kuflik, Ian Lewis, Mariangela Lisanti, Tao Liu, Zhen Liu, Ran Lu, Markus Luty, Patrick Meade, David Morrissey, and Stephen Mrenna, "Simplified Models for LHC New Physics Searches", *J.Phys.* **G39** (2012) 105005, `arXiv:1105.2838`. `doi:10.1088/0954-3899/39/10/105005`.

[46] MARMOSET Collaboration, "MARMOSET: The Path from LHC Data to the New Standard Model via On-Shell Effective Theories", (2007). `arXiv:hep-ph/0703088`.

[47] B. Knuteson and S. Mrenna, "BARD: Interpreting New Frontier Energy Collider Physics", (2006). `arXiv:hep-ph/0602101`.

[48] D. Bourilkov, R. C. Group, and M. R. Whalley, "LHAPDF: PDF Use from the Tevatron to the LHC", (2006). `arXiv:hep-ph/0605240`.

[49] CMS Collaboration, "Absolute Calibration of the Luminosity Measurement at CMS: Winter 2012 Update", CMS Physics Analysis Summary CMS-PAS-SMP-12-008, (2012).

[50] W. Beenakker, R. Hopker, and M. Spira, "PROSPINO: A Program for the Production of Supersymmetric Particles in Next-to-Leading Order QCD", (1996). `arXiv:hep-ph/9611232`.

[51] CTEQ Collaboration, "New Generation of Parton Distributions with Uncertainties from Global QCD Analysis", *JHEP* **07** (2002) 012. `doi:10.1088/1126-6708/2002/07/012`.

[52] CMS Collaboration, "Commissioning of b-jet identification with pp collisions at sqrt(s) = 7TeV", *BTV-10-001* (2010).